A Small Animal Optical Tomographic Imaging System with Omni-Directional, Non-Contact, Angular-Resolved Fluorescence Measurement Capabilities

Jong Hwan Lee

Submitted in partial fulfillment of the
requirements for the degree of
Doctor of Philosophy
in the Graduate School of Arts and Science

COLUMBIA UNIVERSITY

2014

Abstract

A Small Animal Optical Tomographic Imaging System with Omni-Directional, Non-Contact, Angular-Resolved Fluorescence Measurement Capabilities

Jong Hwan Lee

The overall goal of this thesis is to develop a new non-contact, whole-body, fluorescence molecular tomography system for small animal imaging. Over the past decade, small animal in vivo imaging has led to a better understanding of many human diseases and improved our ability to develop and test new drugs and medical compounds. Among various imaging modalities, optical imaging techniques have emerged as important tools. In particular, fluorescence and bioluminescence imaging systems have opened new ways for visualizing many molecular pathways inside living animals including gene expression and protein functions. While substantial progress has been made in available prototype and commercial optical imaging systems, there still exist areas for further improvement in the outcome of existing instrumentations. Currently, most small animal optical imaging systems rely on 2D planar imaging that provides limited ability to accurately locate lesions deep inside an animal. Furthermore, most existing tomographic imaging systems use a diffusion model of light propagation, which is of limited accuracy. While more accurate models using the equation of radiative transfer have become available, they have not been widely applied to small animal imaging yet.

To overcome the limitations of existing optical small animal imaging systems, a novel imaging system that makes use of the latest hardware and software advances in the field was

developed. At the heart of the system is a new double-conical-mirror-based imaging head that enables a single fixed position camera to capture multi-directional views simultaneously. Therefore, the imaging head provides 360-degree measurement data from an entire animal surface in one step. Another benefit provided by this design is the substantial reduction of multiple back-reflections between the animal and mirror surfaces. These back reflections are common in existing mirror-based imaging heads and tend to degrade the quality of raw measurement data. Furthermore, the conical-mirror design offers the capability to measure angular-resolved data from the animal surface. To make full use of this capability, a novel equation of radiative transfer-based ray-transfer operator was introduced to map the spatial and angular information of emitted light on the animal surface to the captured image data. As a result, more data points are involved into the image reconstructions, which leads to a higher image resolution. The performance of the imaging system was evaluated through numerical simulations, experiments using a well-defined tissue phantom, and live-animal studies. Finally, the double reflection mirror scheme presented in this dissertation can be cost-effectively employed with all camera-based imaging systems. The shapes and sizes of mirrors can be varied to accommodate imaging of other objects such as larger animals or human body parts, such as the breast, head, or feet.

Table of Contents

List of Figures

List of Tables

List of Acronyms

2D	2-Dimensional
3D	3-Dimensional
AFC	Activation Flow Coupling
AOI	Angle of Light Incidence
APD	Avalanche Photodiode
BFGS	Broyden-Fletcher-Goldfarb-Shanno
BLT	Bioluminescence Tomography
CAD	Computer Aided Design
CCD	Charge Coupled Device
CG	Conjugate Gradient
CT	X-ray Computed Tomography
CW	Continuous Wave
DA	Diffusion Approximation
DOT	Diffuse Optical Tomography
DyCE	Dynamic Contrast Enhanced
ERT	Equation of Radiative Transfer
FD	Frequency Domain
FDA	Food and Drug Administration
FMT	Fluorescence Molecular Tomography
FOV	Field of View
GFP	Green Fluorescent Protein
GMRES	Generalized Minimum Residual
I&Q	In-phase and Quadrature
ICCD	Intensified Charge Coupled Device
ICG	Indocyanine Green
IP	Intraperitoneal
IV	Intravenous
KKT	Karush-Khun-Tucker
MCP	Micro Channel Plate
MRI	Magnetic Resonance Imaging
NIR	Near Infrared
OTI	Optical Tomographic Imaging
PBS	Phosphate Buffered Saline
PCA	Principle Component Analysis
PD	Photodiode
PDE	Partial Differential Equation
PET	Positron Emission Tomography
PMT	Photomultiplier Tube
PDW	Photon Density Wave
QD	Quantum Dot
QN	Quasi Newton
RF	Radio Frequency
ROI	Region of Interest

rSQP	Reduced Hessian Sequential Quadratic Programming
SNR	Signal-to-Noise ratio
SPECT	Single Photon Emission Computed Tomography
SQP	Sequential Quadratic Programming
SSD	Steady State Domain
TCSPC	Time Correlated Single Photon Counting
TD	Time Domain
THb	Total Hemoglobin Concentrations
TPSP	Temporal Point Spread Function
VEGF	Vascular Endothelial Growth Factor

Publications Resulting from This Work

PATENT APPLICATION

[1] **J. H. Lee** and A.H. Hielscher, "Systems and Methods for simultaneous multidirectional imaging for capturing tomographic data," International application number #PCT/US2012/064245, filed on Nov. 11 2012, published May 16, 2013. <http://patentscope.wipo.int/search/en/detail.jsf?docId=WO2013070982>

JOURNAL ARTICLES

[1] **J. H. Lee,** H. K. Kim, C. Chandhanayingyong, F. Y. Lee, and A. H. Hielscher, "Non-Contact Small Animal Fluorescence Imaging System for Simultaneous Multi-directional Angular-dependent Data Acquisition," Biomedical Optics Express **5**(7), 2301-2316 (2014).

[2] H. K. Kim, **J. H. Lee**, and A. H. Hielscher, "PDE-Constrained Fluorescence Tomography with the Frequency Domain Equation of Radiative Transfer," IEEE Journal of Selected Topics in Quantum Electronics, **16**(4), 793-803 (2010).

CONFERENCE PROCEEDINGS

[1] **J. H. Lee**, H. K. Kim, J. Jia, C. Fong, and A. H. Hielscher, "A fast full-body fluorescence /bioluminescence imaging system for small animals," Proceedings of SPIE, Vol. 8578, 857821-1 (2013).

[2] J. Jia, **J. H. Lee**, L. D. Montejo, H. K. Kim, and A. H. Hielscher, "Measurement operator for angular dependent photon propagation in contact-free optical tomography," Proceedings of SPIE, **8578**, 857815-1 (2013).

[3] J. M. Masciotti, **J. H. Lee**, M. Steward, and A. H. Hielscher, "Instrumentation for simultaneous magnetic resonance and optical tomographic imaging of the rodent brain," Proceedings of SPIE, **7171**, 71710Q (2009).

CONFERNCE ABSTRACTS

[1] **J. H. Lee**, H. K. Kim, and A. H. Hielscher, "None Contact Small Animal Fluorescence Imaging System for Angular-Resolved Tomography," OSA, BIOMED, OSA (2014).

[2] **J. H. Lee**, H. K. Kim, J. Jia, and A. H. Hielscher, "Non-contact multi-directional viewing scheme for camera-based optical tomographic small animal imaging system," at Advances in Optics for Biotechnology, Medicine and Surgery XIII, Engineering Conferences International (ECI), Lake Tahoe, NV, June 2-5, (2013).

[3] **J. H. Lee**, T. Pöschinger, S. Hernandez, J. Huang, T. Johung, J. Kandel, D. J. Yamashiro, and A. H. Hielscher, "Dynamic Fluorescence Imaging for the Detection of Vascular Changes in Anti-Angiogenic Drug Therapy," OSA, BIOMED, OSA (2010).

[4] M. L. Flexman, S. L. Hernandez, J. Huang, T.J. Johung, H.K. Kim, **J. H. Lee**, F. Vlachos, D. J. Yamashiro, J, Kandel, and A. H. Hielscher, "Early Detection of Tumor Vascular Response to Anti-Angiogenic Drugs with Optical Tomography," BIOMED, OSA (2010).

[5] **J. H. Lee**, T. Pöschinger, S. L. Hernandez, J. Huang, T. Johung, J. Kandel, D. J. Yamashiro, and A. H. Hielscher, "Monitoring of Anti-Angiogenic Drug Response with Dynamic Fluorescence Imaging," Proceedings of the IEEE 36th Annual Northeast Bioengineering Conference (2010).

[6] M. L. Flexman, S. L. Hernandez, J. Huang, T. Johung, H. K. Kim, **J. H. Lee**, F. Vlachos, D. J. Yamashiro, J. Kandel, and A. H. Hielscher, "Optical Tomographic Imaging of Tumor Response to Anti-Angiogenic Drugs in Small Animals," Proceedings of the IEEE 36th Annual Northeast Bioengineering Conference (2010).

[7] N. Patel, **J. H. Lee**, K. Nair, H. G. Lee, M. Mikami, J. Staples, A. H. Hielscher, and F. Y. Lee, "Heparin-Regulated controlled release of BSA-Doxorubicin conjugate promotes sarcoma apoptosis: A novel site specific method for treating solid tumors," Poster, Orthopedic Research Society, New Orleans, March (2010).

[8] L.D. Montejo, **J. H. Lee**, A. H. Hielscher, and A. D. Klose, "Numerical and Experimental Studies of GFP Expressing Small Animal Models with the Equation of Radiative Transfer", World Molecular Imaging Congress (2009).

Acknowledgments

It's been a long journey to obtain my PhD thesis. My journey began with an email from Dr. Andreas H. Hielscher, which led me into the world of optical tomography and a new challenging life in the U.S. In retrospect, without the help of so many people around me, I could not have arrived at this destination. So, I would like to take this opportunity to thank all of them.

First, I would like to thank Dr. Andreas H. Hielscher who offered me a chance to study in his lab and it has been an honor to receive his insightful mentoring. He is so enthusiastic about his research and has provided me with so many chances to co-work with brilliant researchers at the campus and medical center. His guidance in all aspects has been invaluable to my research pursuits.

I am also thankful to Dr. Andrew Lain and Dr. Elisa E. Konofagou who served on my thesis committee. They previously have sent me feedback on my work and made me see a big picture of my research. In addition, they always encourage me with a big smile. Also, I owe thanks to Dr. Francis Y. Lee for all the experiments using animal models. Without him and the researchers in his lab, I would not have generated any *in vivo* imaging results. I cannot begin to thank them enough.

There are so many other people who I have to mention for their support. Dr. Hyun Keol Kim has patiently taught me a lot of the fundamentals of optics and reconstruction algorithms and has shared with me many different aspects of research and life. I will not forget his and his family's help forever. James Masciotti is another name, which I cannot forget. When I was new to everything and tried to apply myself to different world, he always was beside me and supported me.

I will also never forget the friendship of my colleagues, Ludguier Montejo, Molly Flexman, and Michael Khalil. We spent precious time in school life together, and they always said yes whenever I asked for some help. Also, I would like to thank Chris Fong, Jingfei Jia, Jacqueline Gunther, and Jennifer Hoi, who are smart friends that came to the lab as new members and are currently doing great work. I would like to thank them also for their support. Especially, I would like to thank Jacqueline who has helped me a lot when I was overhasty in my thesis defense. I also want to deliver my thanks to Jinhyup Lee, Jaewoo Kim, Eric Lee, Steven Kim, Sol Lee, and their families. I will remember forever the support of Dr. Kyung-Ok Kim and Hyejin Eum who I also thank from my heart.

Finally, I would like to mention that none of my achievements could have been possible without my family. For my entire life, my mom and dad have always supported me with all their energy and without any hesitation. Whenever I had a hard time, they have always been beside me, given me a shoulder to lean on, and sent me their endless love. I also owe so much to my brother, sister-in-law, and sister. They have taken care of parents so I could focus on my work without too much worry about them and have encouraged me to stand on my own feet. My precious niece Chaeyeong and nephew Seonggyu, I send my love to you.

Dedication

For Mom and Dad

Chapter 1

BACKGROUND AND MOTIVATION

1.1 Overall Goals and Specific Aims

The overall goal of this thesis is to develop a new fluorescence molecular tomography (FMT) imaging system that can overcome the limitations of existing small animal optical imaging techniques. Over the past decade, in vivo small animal imaging has improved our ability to probe underlying biological and morphological features of human diseases. In addition to micro-CT, high-field MRI, ultrasound, and PET systems, optical imaging techniques have emerged as important and powerful tools for in vivo studies. In particular, fluorescence and bioluminescence imaging systems opened new ways for visualizing many molecular pathways inside living animals including gene expression and protein functions. While substantial progress has been made in available prototype and commercial optical imaging systems, further improvement of existing instrumentation is highly desirable. Currently, most small animal optical imaging systems rely on 2D planar imaging that provides limited ability to accurately locate lesions deep inside an animal. Furthermore, most existing tomographic imaging systems use a diffusion model of light propagation, which is of limited accuracy. While more accurate models using the equation of radiative transfer (ERT) have become available, they have not been widely applied to small animal imaging yet. In addition, the full use of the angle-dependent information contained in the ERT models requires angular-resolved transmission and reflection measurements, which currently existing systems do not provide simultaneously.

The work of this thesis aims to overcome the limitations of existing optical techniques for small animal imaging by designing and implementing a novel imaging system that involves the

latest hardware and software advances in the field. In particular, I pursue the following initial exploratory study and three specific aims:

A) Initial Exploratory Study: Use existing commercial system to explore strengths and weaknesses of commercial small animal imagers

The Maestro2 In Vivo imaging system (CRi, Inc., Woburn, MA) was used to perform both bioluminescence imaging and fluorescence imaging. In particular the system was employed to monitor early tumor vascular response to drug therapy. This is a common area of preclinical imaging and a likely future application of any new small animal imaging system. The response of Ewing sarcoma to anti-angiogenic drug was studied and the reliability of extracted biomarkers was tested.

B) Specific Aim I: Development of a frequency-domain, full-body, non-contact, small animal molecular imaging system that can acquire angular-resolved data for the ERT-based image reconstruction.

The experience of the exploratory study was used to design an improved small animal imaging system. The system employs a frequency-domain scheme to provide the separation of scattering from absorption and fluorescence effects. A main component of this system is a double conical mirror design that allows for the acquisition of data from the entire surface of the animal in one image. The projected entire surface image is captured with an intensified CCD camera that is operated in homodyne mode in conjunction with a multi-wavelength free-space illumination scheme. This non-contact design allows for acquiring angular-resolved light emission data from a large number of points on the surface of the animal.

C) Specific Aim II: Characterization and testing of the new system in phantom experiments

The system characterization studies were carried out using tissue phantoms that mimic optical properties of small animals. To this end, the acquired angular-resolved measurements were used as input to a novel ERT-based image reconstruction scheme that allows for multi-wavelength angular-resolved data. The obtained characterization information was used for subsequent animal studies.

D) Specific Aim III: Demonstrate the utility of the system in small animal pilot studies

The utility of the system was tested in pilot studies involving tumor-bearing mice with Green Fluorescent Protein (GFP)-tagged osteosarcoma cells. After injecting the GFP-tagged tumor cells into different areas in the mice, subcutaneously near the kidney and near the pelvis (the center of the abdomen), the mice were imaged every week for three weeks to measure the variation of tumor size. The results were corroborated with CT imaging and the explanted tumor at the end of the study.

The dissertation is organized as follows. The remainder of Chapter 1 reviews the fundamentals of diffuse optical tomography (DOT), including fluorescence molecular tomography (FMT) and bioluminescence molecular tomography (BLT). Chapter 2 presents the initial exploratory study using one of existing commercial systems. Chapter 3 introduces a basic concept of the conical mirror-based imaging head and goes into details of implementation of each system unit. In Chapter 4, the ERT-based image reconstruction algorithm and the ray transfer operator that involves angular-resolved measurement data into the image reconstruction

are described in details. Chapter 5 shows the results of phantom and animal experiments as well as numerical simulations to compare angular-resolved and angular-averaged data. Finally, Chapter 6 concludes this thesis with a summary and possible future work.

1.2 Diffuse Optical Tomography

1.2.1 Introduction

Diffuse optical tomography (DOT) is an optical imaging method that provides three-dimensional spatial distribution of intrinsic optical properties in tissues. This method employs low energy radiation of visible or near infrared (NIR) light and a model-based image reconstruction algorithm to non-invasively probe deep inside biological tissue.

In DOT imaging, external light sources illuminate points or areas on the surface of a target object. Then the detectors at various points on the target surface measure transmitted or back-reflected light intensities after they pass through the target body [1, 2]. Using measurement data and a model-based image reconstruction algorithm, the distribution of optical properties such as absorption coefficient, μ_a , (typically 0.01-2cm^{-1}) and scattering coefficient, μ_s , (typically 10-200 cm^{-1}), are reconstructed in three dimensions. The reconstructed optical properties are then related to physiologically or pathologically important parameters (e.g., oxy-hemoglobin (HbO_2) or deoxy-hemoglobin (Hb)) inside the target.

While DOT is similar to X-ray computed tomography in terms of using electromagnetic radiation for generating imaging contrast, they are different in several aspects. First, X-ray uses shorter wavelengths with higher ionizing energy (~5 to 150 keV), whereas DOT uses longer wavelengths with lower, non-ionizing energy (approximately 1 to 2.5 eV). As a result, DOT

imaging can be used more safely than X-ray imaging in applications and longitudinal studies. Secondly, while X-ray uses Beer-Lambert law and the inverse radon transform for the image reconstruction, direct inversion schemes cannot be used in DOT imaging. Unlike X-ray imaging DOT has to deal with multiple scattering events by cellular and sub-cellular tissue structures. Such scattering effects inside the tissue are taken into account by employing appropriate light propagation model [3-9]. The reconstructed images of optical properties are obtained by solving the associated inverse problems.

A commonly used light propagation model is a diffusion approximation (DA) to the equation of radiative transfer (ERT). The DA requires that the medium under consideration is optically thick (meaning many scattering events occur before the light exists the tissue), that absorption coefficient is considerably smaller than scattering coefficient ($\mu_a \ll \mu_s$), and that no void-like regions with low scattering and low absorption are present. In theses cases, the DA model provides accurate solutions and can be solved much faster than the complex ERT. If one deals with strongly absorbing media ($\mu_a \gg \mu_s$) or tissues in which boundary effects dominate, the ERT provides a much more accurate light propagation model. Recent years have seen considerable efforts to develop accurate ERT-based image reconstruction algorithms for DOT [10-20].

1.2.2 Optical Properties as Imaging Contrast

The absorption coefficient μ_a describes the probability of photon absorption in a medium. It is defined as the inverse of the mean photon penetration depth into a medium. Since each chromophore has its particular spectral absorption shape, the analysis of absorption spectrum can

provide individual concentration of the chromophores in mixed media. The primary absorbers inside tissues in the visible or NIR wavelength range are oxy-hemoglobin (HbO_2), deoxy-hemoglobin (Hb), water (H_2O) and fat as shown in Figure 1-1. Therefore, DOT is particularly suited to provide information about blood and its oxygenation levels.

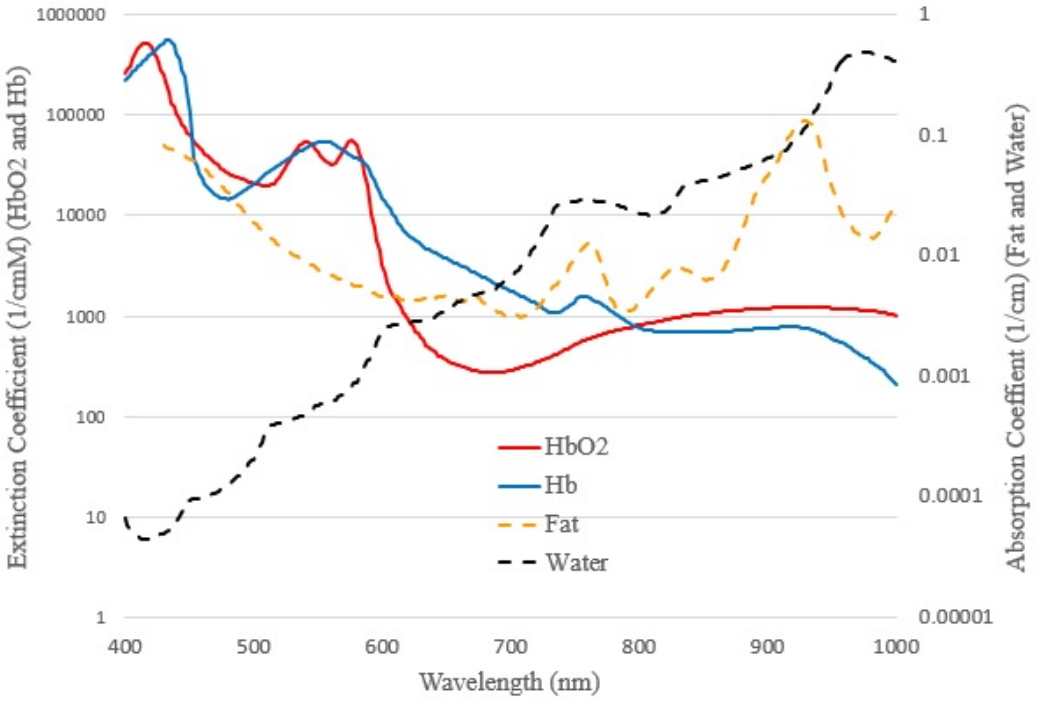

Figure 1-1. Absorption spectra of main chromophores in tissue (Data taken from [21])

The scattering coefficient μ_s represents the inverse of the mean free path of a photon before the photon encounters a scattering process. In tissues, many organelles such as nuclei, mitochondria, etc. act as scattering centers and generate elastic scattering, depending on the wavelength, the size, and the refractive index of matter. The angle of the scattering direction is described by the phase function. The mean cosine of scattering directional angle, called anisotropy factor g, depicts the degree of angular distribution of the phase function. Therefore,

for isotropic scattering, g equals zero. When there is no directional change in scattering, g equals one. The anisotropy of biological medium is close to 0.98 [22].

1.2.3 Signal Detection Techniques for Differentiating Optical Properties

Depending on the measurable parameters, the imaging modes of DOT are divided into three categories: continuous wave (CW) mode (also referred to as steady state domain (SSD) mode), time domain (TD) mode, and frequency domain (FD) mode.

The CW mode uses a constant intensity light as a source and solely measures the attenuation of light intensity passing through tissues. This attenuation is usually wavelength dependent. This approach allows for simple low-cost instrumentation with high signal-to-noise-ratio (SNR) and faster data acquisition for dynamic signal detection. The disadvantage of this approach is its relatively low information content, which makes it difficult to differentiate between the absorption and the scattering effects in tissues [23]. This can be overcome by using a TD system.

In TD systems, pico- or femto-second light pulses illuminate tissues and detectors record temporal profiles of light (Temporal Point Spread Function (TPSP)) at different photon arrival times [24]. This approach yields much more information and helps to differentiate absorption and scattering properties in tissues. As a result, the TD mode can improve spatial resolution and sensitivity compared with the CW imaging mode. However, due to the very short time-gated detection, SNR is low and long data acquisition times are required. These characteristics also prevent the use of TD systems for studying sub-second hemodynamic effects. In addition these systems are rather expensive compared to CW and FD imaging modes, because of the fast time-gated detection technology and related pulse laser electronics that are involved.

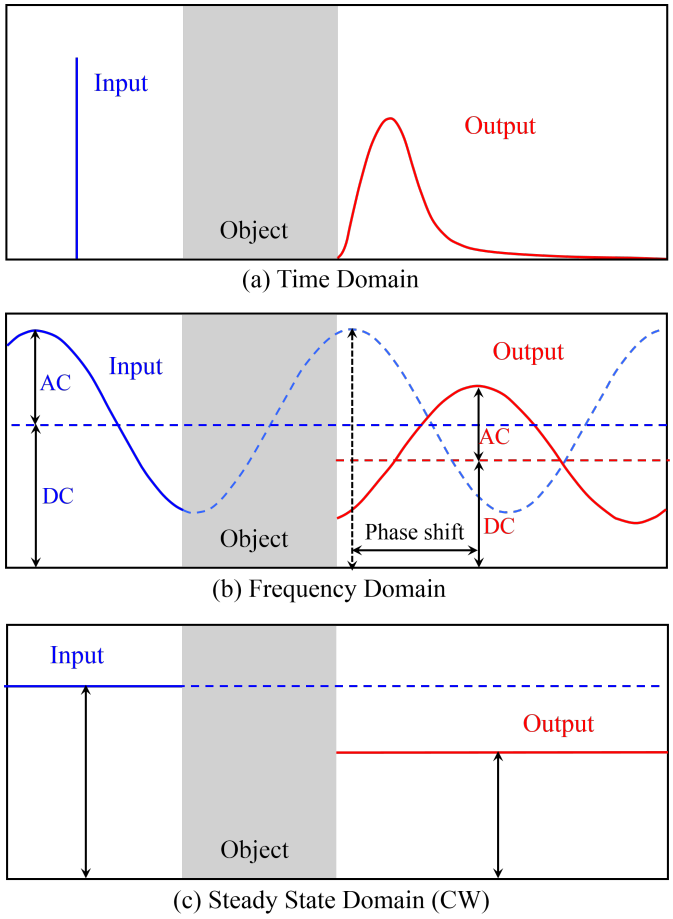

Figure 1-2. Signal detection modes (input (blue) and output (red) after passing through medium) (a) time domain, (b) frequency domain, and (c) continuous wave mode

FD systems constitute a compromise between CW and TD systems [25-27]. In the FD mode, the light source is amplitude modulated at radio frequencies in the hundreds of MHz. If the amplitude-modulated light is injected into biological tissues, a diffuse photon-density wave (PDW) is generated [28, 29]. The intensity attenuation and the phase shift of PDWs can be measured. FD systems are less expensive and offer higher SNR than TD system. In addition, FD systems can differentiate absorption and scattering more precisely and show better spatial resolution than the CW system. However, the FD system is somewhat more expensive and has lower SNR than the CW system [30].

1.2.4 Applications of Diffuse Optical Tomography

DOT has various applications due to its high sensitivity to blood-dependent parameters. Medical problems that involve changes in the blood-related parameters could benefit from the use of DOT. Especially, cancerous tumors often exhibit higher vascularity and higher blood volume than normal tissues; blood oxygenation levels are often used to monitor the status of tumor progression. Currently, DOT imaging for cancer detection has been primarily focused on breast imaging. DOT is a safe, noninvasive and inexpensive imaging method compared to traditional X-ray mammography and MRI [31-34]. In many research studies, high total hemoglobin concentrations (THb) and oxygen saturation level have been used for diagnosis and monitoring the efficacy of cancer treatments [35, 36].

Functional brain imaging for monitoring cerebral hemodynamics is another interesting application of DOT. Activation flow coupling (AFC) is the regional changes in cerebral blood flow by the functional stimulation. Since AFC is a key indicator of neuronal activity, DOT has been shown to monitor these AFC responses non-invasively in the brain [37, 38]. In addition, DOT has been applied to differentiate ischemic strokes and hemorrhage strokes, which have different mechanisms in the outbreak of diseases [39, 40]. Another application is joint disease monitoring. Scattering coefficient changes are observed in the synovial fluid of joints affected by arthritis and inside the bones of patients with osteoarthritis. Hence several groups have focused their efforts on developing DOT systems for joint and bone imaging [41, 42].

The biggest impact has arguably been in small animal imaging. DOT has been used to image small animal models of human diseases, particularly in the fields of oncology and neurology. Recent advances in transgenic manipulation of small animals have led to many human disease models and has opened a whole new field of investigating human diseases on a

molecular level [43-46]. Especially, the variants of DOT (fluorescence molecular tomography (FMT) and bioluminescence molecular tomography (BLT)) allow one to image whole processes of a disease including progression, remission, and treatment at molecular levels [47, 48]. In addition, DOT is increasingly used to test treatment efficacies and molecular imaging for drug developments [49, 50]. Novel fluorescence and bioluminescence biochemical markers that can be used in these studies are constantly being developed in many laboratories and companies around the world [51-53].

1.3 Fluorescence and Bioluminescence Molecular Tomography

While FMT and BLT are similar techniques to DOT in terms of three-dimensional reconstruction of optical properties inside a target body, they are different in terms of contrast mechanism. FMT utilizes appropriate wavelength lights to excite exogenous fluorescent reporters tagged on specific cells or molecules inside the target body [51-53]. Then the emitted light from the fluorescent reporters is collected at a shifted wavelength from the excitation wavelength. Measured signals at the target surface are used to reconstruct absolute concentration and position of fluorescent reporters, namely specific cells or molecules. Therefore, unlike DOT, FMT requires the solution of an inverse source problem. In the case of BLT, chemical reactions within a target body replace the role of the external excitation light of FMT [54-56].

1.3.1 Mechanism of Fluorescence Generation

Fluorescence, one of photoluminescence phenomena, can be described by using Jablonski energy diagram in Figure 1-3. This diagram illustrates that when molecules called fluorophores absorb photons at a particular wavelength, electrons of fluorophores transition from a ground state to

excited electronic states. The excited electrons lose most of their energy through non-radiative processes such as vibrational relaxation (within the same energy band) or internal conversion (between the bands, for example, from S2 to S1 in Figure 1-3) and return to the first excited state. The average time the electrons spend in the excited states is referred to the fluorescence lifetime and can provide information about the microenvironment of flurophore tagged molecules. The excited electrons in the first state (S1) lose the rest energy by radiative process of emitting photons, called fluorescence and return to the ground state (S0).

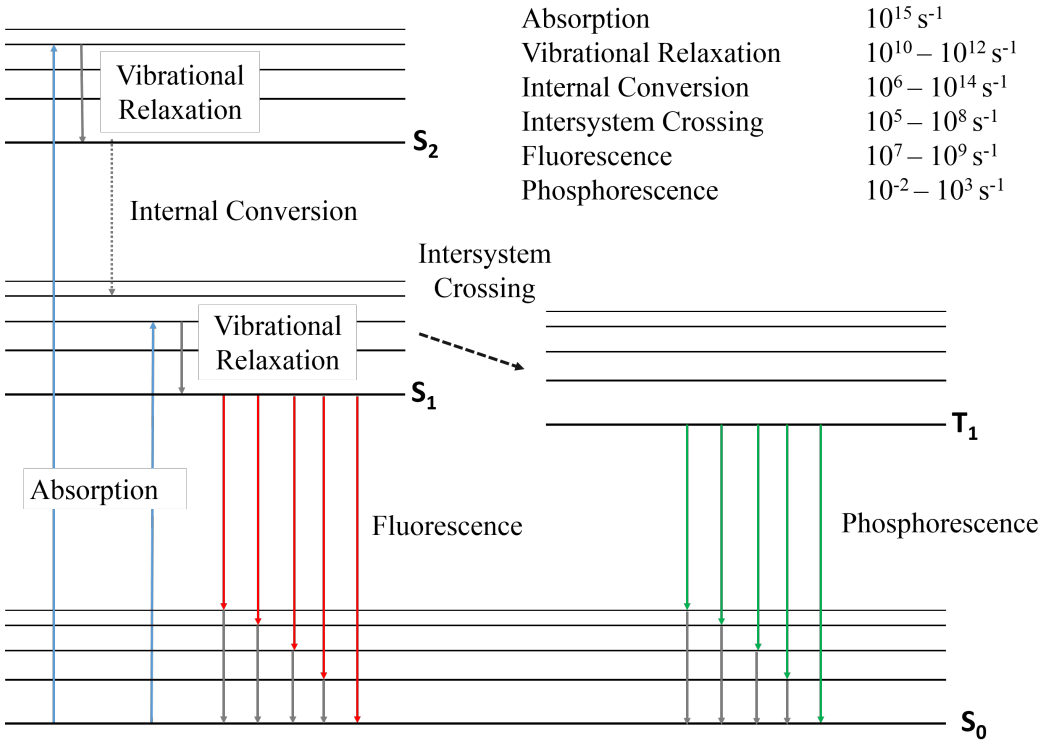

Figure 1-3. Jablonski energy diagram: Blue, red, and green arrows represent radiative transitions (absorption, fluorescence and phosphorescence) and gray and dashed arrows represent non-radiative transitions (vibrational relaxation, internal conversion, and intersystem crossing).

Another path for energy dissipation is intersystem crossing from S1 to T1 in Figure 1-3. This occurs when the electrons change their spin multiplicity from a singlet state to a triplet state

and leads to phosphorescence, which is slower than fluorescence. Finally, the energy difference between the photon absorption and the emission causes the difference in the between the maxima of excitation spectra versus the emission spectra, otherwise known as the Stokes shift. This critical property is the basic principle of fluorescence imaging that one can see only the fluorescent object by blocking the excitation light. A large Stokes shift is better in order to filter out the excitation from the emission under experimental conditions. The excitation and emission spectra of green fluorescent protein (GFP), for example, is shown in Figure 1-4.

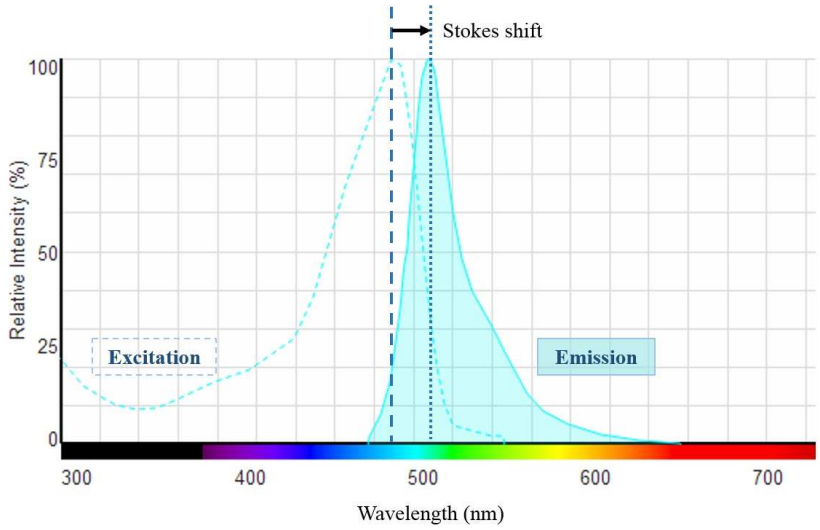

Figure 1-4. Excitation and emission spectra of green fluorescent protein (GFP) (reproduced from http://www.lifetechnologies.com)

Fluorophores can be divided into three categories: Organic dyes, biological fluorophores, and fluorescent nanoparticles. The most popular organic fluorophores are cyanine dyes and green fluorescent protein (GFP) derivatives are well known biological fluorophores. These fluorophores have been widely used in various biological applications since 1990s. In addition, fluorescent nanoparticles, quantum dots (QDs) and semiconductor nano-crystal materials have been employed in small animal imaging under consideration of toxicity [57].

1.3.2 Modeling of Fluorescence Phenomenon

The fluorescence generation process can be briefly modeled by using a simple two energy level system [58, 59]. Assuming that there are only one ground and one excitation states, the rate equation for excited fluorophores can be described as:

$$\frac{d}{dt}N\left(t\right) = -\frac{1}{\tau}N\left(t\right) + \mu_a^{x\to m}\phi^x\left(t\right) \tag{1.1}$$

where $N\left(t\right)$ is the number density of the excited fluorophores in the units of fluorophores cm^{-3}, τ represents the lifetime of fluorophores; $\mu_a^{x\to m}$ denotes the absorption coefficient of the fluorophores; and $\phi^x\left(t\right)$ is the local fluence in units of Watts cm^{-2}. The fluorescence source term $Q\left(r,t\right)$, which represents the density of all emitted photons during τ, can be obtained from the rate equation (1.1) as:

$$Q\left(r,t\right) = \frac{\eta}{\tau}N\left(r,t\right) = \frac{\eta\mu_a^{x\to m}\left(r\right)}{\tau}\int_{t'=0}^{t'=t}\phi^x\left(r,t'\right)\exp\left(\frac{t'-t}{\tau}\right)dt'. \tag{1.2}$$

If the excitation light source is the intensity modulated light at frequency ϖ, $Q\left(r,t\right)$ is reformulated with a Fourier transform of equation (1.2) as:

$$Q\left(r,\varpi\right) = \frac{\eta\mu_a^{x\to m}\phi^x(\mathbf{r},\varpi)}{(1-\varpi\tau(\mathbf{r}))}. \tag{1.3}$$

Therefore the frequency-domain ERT for the generation and propagation of fluorescent light is given as:

$$\left[(\nabla\cdot\Omega)+\mu_a^x+\mu_s^x+\mu_a^{x\to m}+\frac{i\varpi}{c}\right]\psi^x(\mathbf{r},\Omega,\varpi)=\int_{4\pi}p(\Omega',\Omega)\psi^x(\mathbf{r},\Omega',\varpi)d\Omega' \tag{1.4}$$

$$\begin{aligned}\left[(\nabla\cdot\Omega)+\mu_a^m+\mu_s^m+\frac{i\varpi}{c}\right]&\psi^m(\mathbf{r},\Omega,\varpi)\\ &=\int_{4\pi}p(\Omega',\Omega)\psi^m(\mathbf{r},\Omega',\varpi)\,d\Omega'+\frac{1}{4\pi}\frac{\eta\mu_a^{x\to m}\phi^x(\mathbf{r},\varpi)}{(1-\varpi\tau(\mathbf{r}))}.\end{aligned} \tag{1.5}$$

where μ_a and μ_s are the absorption and scattering coefficients. The superscript x and m represent excitation and emission. Ω and c are the angular direction and the speed of light inside the tissues. $\psi(\mathbf{r},\Omega,\varpi)$, η , and $p(\Omega',\Omega)$ denotes light radiance, quantum efficiency, and a phase function respectively. More discussions on the above fluorescence system are provided in Chapter 4.

1.3.3 Mechanism of Bioluminescence Generation

In bioluminescence, the light emission process is a result of a chemical reaction within living organisms. The binding of a specific substrate and an enzyme in organisms catalyzes an oxidation-reduction reaction of small molecules and relaxes an electronically excited intermediate, which emits light. This light generation process in biological tissues can be accurately modeled by the ERT as [60-62]:

$$\left[\Omega\cdot\nabla+\mu_t\left(r\right)\right]\psi(\mathbf{r},\Omega)=\mu_s\left(r\right)\int_{4\pi}p(\Omega\cdot\Omega')\psi(\mathbf{r},\Omega')\,d\Omega'+\frac{Q\left(r\right)}{4\pi} \quad (1.6)$$

Where $\mu_t\left(r\right)=\mu_a\left(r\right)+\mu_s\left(r\right)$ is the attenuation coefficient.

Although various bioluminescent systems have been identified in nature, the most widely used bioluminescent reporter in preclinical imaging has been luciferase from the North America firefly (Photinus pyralis; FLuc). Other luciferases have come from jellyfish (Aequorea), and the sea pansy (Renialla; RLuc), which have also been cloned for molecular imaging [63].

1.3.4 Comparison between FMT and BLT

Though FMT and BLT both employ exogenous optical reporters to investigate cellular or sub-cellular biological events, they are different in several aspects [64]. First, signals from fluorophores are generally much stronger than those from bioluminescent probes. This typically leads to much shorter data acquisition times in FMT. While fluorescence signals can be acquired in a few milliseconds, bioluminescence signals typically require several minutes of integration time. As a result, BLT is limited to the CW domain imaging mode, whereas fluorescence measurements can be conducted in all three imaging modes, CW, FD and TD. If the FD or TD imaging mode is applied to FMT, fluorophore lifetime measurement can be obtained. The lifetime measurement provides more robust raw data than fluorescent intensity measurement because it is independent from the intensity of excitation light and the fluorophore concentration. Moreover, it can be also used for filtering out the autofluorescence in tissues [65-68]. Table 1-1 summarizes the features of each imaging mode (CW, FD, and TD) of FMT and BLT.

Another advantage of FMT is that there are far more fluorescent probes than bioluminescent probes with emission wavelengths in the NIR range. The NIR fluorescent probes provide longer penetration depth in tissues than the visible wavelength ranges of bioluminescence probes. On the other hand, autofluorescence of tissues in the visible wavelength range is much stronger than autobioluminescence. Hence bioluminescence signals have much higher signal-to-noise ratios (SNRs) in the visible range spectrum than fluorescence signals. Accordingly, fluorescence imaging has higher sensitivity in the far-red and NIR range and bioluminescence imaging has higher sensitivity in the visible range due to the wavelength dependence of absorption, autofluorescence and autobioluminescence of tissues.

Lastly, the reconstruction algorithms for FMT use two coupled equations for excitation and emission light, while those of BLT employ an equation only for emission light. Consequently, the image reconstruction problems of BLT without an excitation part, are much more ill-posed than those of FMT [69-71].

Table 1-1. Comparison of features and performance among three major imaging modes (from the references [30, 72])

	Continuous Wave (Steady-State)	Frequency-Domain	Time-Domain
Signal Biochemical properties (Contrast)	**Intensity** Fluorescence Concentration and quantum yield Bioluminescence	**Intensity and phase** Absorption/scattering Fluorescence lifetime Concentration and quantum yield	**Time-gated signal,** **Point-spread function** Absorption/scattering Fluorescence lifetime Concentration and quantum yield
Excitation Sources	Virtually any light source Filament and gas lamps LED Laser diode Gas Laser Solid-state laser	Frequency modulated source LED Laser diode Other modulated sources	Pulsed source Laser diode Tunable lasers
Detection Instrumentation	Virtually any light detector CCD ICCD EMCCD PMT APD	Homo or heterodyned detection ICCD EMCCD PMT APD	Time correlated single photon counting, time-gated detection ICCD EMCCD PMT APD
Filtering Techniques	Interference or absorption filters, Liquid crystal tunable filters, Spectrograph gratings, Dichroic mirrors		
*Resolution	1 mm	0.5-1 mm	0.5-1 mm
*Sensitivity	Picomoles-femtomoles	Picomoles	Picomoles
Depth	< 50 mm	< 30 mm	< 30 mm
Signal-to-noise ratio	High	Medium	Medium
Cost	Low/medium	Medium/high	High

* Obtained with 10 picomoles of an organic fluorophore at the center of 15 mm thick tissues.

1.4 Review of Existing Small Animal Imaging Systems

1.4.1 Introduction

In vivo small animal imaging has emerged as a critical tool in preclinical and translational research to understand biological foundation and morphological features of human diseases. In contrast to traditional *in vitro* or *ex vivo* analysis of tissue samples, *in vivo* small animal imaging allows for non-invasive longitudinal assays of complex physiological and pathological phenomena. Therefore, *in vivo* studies facilitate the systemic investigation of many diseases and fill the gap between the results from *in vitro* (or *ex vivo*) studies and clinical findings. As animal models have become more accurate in mimicking human diseases, the entire history of human diseases from inception to its final stage can be traced. In addition, non-invasive imaging methods provide the benefit of more data from significantly reduced animal numbers.

In general, non-invasive imaging modalities for small animals have evolved from the imaging modalities employed in human clinical imaging. For example, information about soft tissue structures can be obtained using magnetic resonance imaging (MRI). Computed tomography (CT) and ultrasound (US) provide anatomical imaging with high spatial resolution. Positron emission tomography (PET) and single photon emission computed tomography (SPECT) can detect specific molecular or cellular targets by using radiotracers. Table 1-2 summarizes the features of the above imaging modalities for small animals and compares their capabilities and performances.

However, since the dimensions of small animals and their organs are substantially different from humans, these clinical imaging devices cannot be used directly and need to be modified for the purpose of small animal imaging. For example, by using higher field-strength magnets between 4.7 and 21 Tesla [73], the spatial resolution of MRI in small animals has been

improved up to ≤100 μm. Small animal imaging with US employs higher frequencies than human US, typically in the range from 15 to 50 MHz. Furthermore micro-bubbles have recently been introduced as a contrast agent to enhance the performance of small animal imaging.

1.4.2 Small Animal Optical Imaging Systems

Over the last decade, the use of small animal optical imaging has increased rapidly with the advancement of optical markers such as bioluminescent and fluorescent probes. High sensitivity and high throughput can be obtained at a lower cost compared with other imaging modalities for small animals. A recent survey also found that optical imaging was the single most used imaging modality in preclinical applications [74]. The main drawback is the shallow penetration depth by strong absorption and scattering in tissues. As a result, one cannot obtain any reliable quantification of target molecules with 2-dimensional (2D) planar imaging of diffuse light distribution on the animal surface. These limitations can be overcome by using tomographic imaging techniques that allow for a three dimensional distribution of targeted molecules in the animal. While considerable progress has been made in small animal optical tomographic imaging (OTI), there is still room for improvement. This thesis has been motivated by such unmet need.

Table 1-2. Summary of current small animal imaging modalities (Reproduced from the references [75-77])

Modality	Intrinsic Contrast	Signal	Spatial Resolution	Sensitivity	Dynamic Imaging	Radiation Dose (cGy)	Time per Study	Number of animals per study	Advantages	Disadvantages	Equipment cost
MRI	High	RF waves	≤ 100μm	μM - mM	Yes	0	Up to ~ 60 min with set-up	1	Nonionizing radiation Qualitative and Quantitative function High spatial and temporal resolution and contrast	Expensive Long acquisition time Limited sensitivity for some functional measures	~$ 1M
CT	High among lung, bone, and heart; none among soft tissues	X-rays	≤ 200μm	mM	No	10-20	10-15 min	1	Unlimited depth penetration High spatial resolution Whole-body imaging Short acquisition time	Ionizing radiation Poor soft-tissue contrast Currently only anatomical and functional imaging	$200-400K
US	Low; high between cystic and solid structures	Sound waves	≤ 100μm		Yes	0	Real time /short	1	Nonionizing radiation Real-time imaging/short acquisition time High spatial resolution Inexpensive	Not whole-body imaging Limited Contrast Agent usage Operator dependency	$200K

Table 1-2 continued

PET	None	γ-ray	1-2 mm	Sub pM	Yes	10-100	5-60 min	1 or 2	Quantitative molecular imaging High sensitivity Molecular targeting Dynamic Imaging	Ionizing radiation Low resolution	$600-800k
SPECT	None	γ-ray	0.5-2mm	Sub pM	No	10-100	30-90 min	1	Quantitative molecular imaging High sensitivity Molecular targeting	Ionizing radiation Low resolution	$600-800k
Optical: Bioluminescence	None	Light waves	~1 cm	nM	No	0	~5 min	1-a few	Non ionizing radiation Inexpensive Molecular targeting	Limited penetration depth Low resolution	$200-400K
Optical: Fluorescence (and NIR)	Variable (None)	Light waves	< 5 mm	nM (pM)	Yes	0	~5 min	1-a few	Non ionizing radiation Inexpensive Molecular targeting	Limited penetration depth Low resolution	$100-200K ($200-300K)

Currently available DOT and FMT tomographic small imaging system can be classified according to their methods for light delivery to the animal and light collection from the animal. The traditional optical tomographic imaging systems have been fiber-based systems (Figure 1-5a). These systems employ light-guiding optical fibers to deliver light from sources to the animal and to collect light from the animal to bring it to the detection components. These detection components are typically PIN diodes, avalanche photo diodes (APDs), or photomultiplier tubes (PMTs). The fibers are in physical contact with the object either directly or indirectly through the wall of an imaging container. While some imaging systems employed direct contact methods in previous clinical applications [78, 79], many systems rely on using imaging containers with simple shapes such as cylindrical or rectangular boundaries. In these cases, the geometrical positions of optical fibers for sources and detectors are fixed on the container wall without considering the irregularity of boundary shapes or the surface area of the object under investigation. The empty space between the animal surface and the container is usually filled with a matching fluid that has tissue-like optical properties. Consequently, the fixed-position fiber setups and the use of matching liquids provide simplified boundary conditions for the image reconstructions process.

However, the fiber-based contact systems exhibit several limitations. A fixed-position geometry of fibers has a limited number of source-detection pairs. Consequently, the amount of available measurement data is limited. Furthermore, the matching fluid that fills the empty space between the object and the container boundary causes signal loss, and light tunneling through the container wall plays a role in additional undesirable signal loss. This results in the degradation of the SNR of the measurement data. Furthermore, since the image reconstruction process involves the surface boundary of the imaging container instead of the object, it is difficult to estimate

precise positions of biomarkers in the object body from the reconstruction results having the container boundary. In addition, these setups can make the imaging procedures and experimental conditions more cumbersome depending on the object being imaged. Particularly, in small animal *in vivo* imaging, an animal has to be submerged in a matching fluid of an imaging container. Handling the anesthetized animal in the matching fluid and maintaining all vital body functions including stable breathing are challenging and can introduce artifacts.

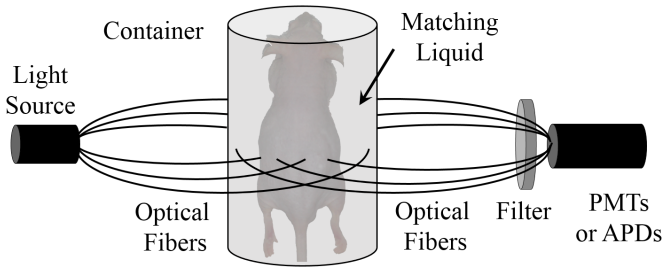

(a) Fiber-based Multi-directional Imaging Setup

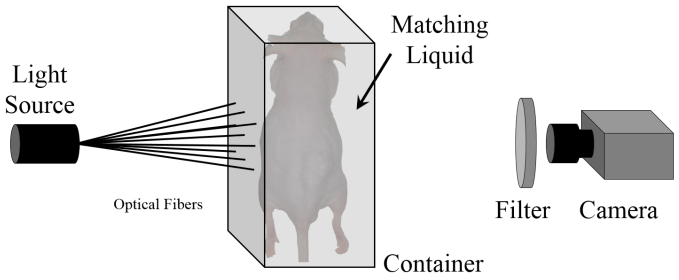

(b) Camera-based Planar Imaging Setup

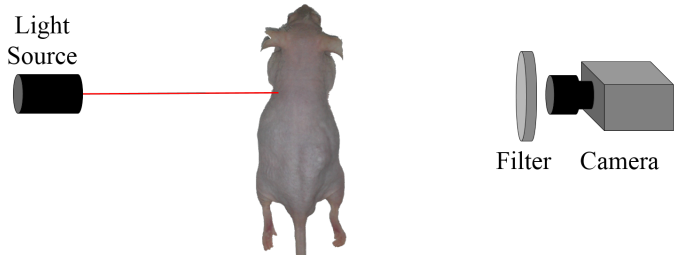

(c) Full noncontact Multi-directional Imaging Setup

Figure 1-5. Different Generations of FMT systems for small animals (a) a first-generation system, employing a fixed pattern of light-guiding fibers for detection and excitation from 360° of view around a cylindrical geometry. (b) a second-generation system with planar geometry, using a CCD camera for detection. (c) a third-generation systems yielding high image performance with a surface rendering of a subject.

The second generation of tomographic imaging system emerged with the advancement of the CCD cameras (Figure 1-5b). Optical fibers fixed on an imaging container are still used for light source delivery. However, a large number of pixels on the CCD camera replace the detection components such as the APD or PMT used in the first generation systems. Typically, an optical fiber bundle for light source delivery is fixed on the one side of a parallel slab geometry. The CCD camera is positioned at the other side to measure transmitted signals. Pixels on the image sensor serve as detectors allowing for a much higher spatial sampling than the first generation systems. The increased measurement data sets in turn improve the image reconstruction results. The systems employing this setup were implemented for preclinical and clinical applications [80, 81]. Nevertheless, the detection using the CCD camera cannot provide full angular coverage of measurement projection, which the fiber-based systems have. The one directional viewing angle of a CCD camera restricts the imaging to transmission (or reflectance) only measurements. However, a recent study demonstrated that both transmittance and reflectance measurements around 60 degrees away from the source are needed to improve the reconstruction results of mouse sized objects [82]. In addition, the animal being imaged still needs to be submerged in a matching liquid. Thus, the issues related with using an imaging container and a matching liquid in the first generation systems still exist.

To circumvent the above difficulties of the first and second-generation systems, non-contact camera-based imaging systems (Figure 1-5c) have recently been developed by some groups [83-87]. Full non-contact imaging systems employ free space source illuminations and CCD-camera-based detections. A collimated light source illuminates an animal directly without optical fibers. The CCD camera directly collects the signals from the animal without a matching liquid and an imaging container. The implementation of this setup has been reported in both

preclinical and clinical applications [88-91]. As the availability of both reflectance and transmittance measurement data in the image reconstruction process lead to more accurate results, non-contact imaging systems have been developed to allow for a full 360° detection [92, 93]. To achieve these multi-directional projection data in small animal imaging, researchers have designed different types of devices that use multiple cameras [92], or rotate the animal in front of a camera [83], or rotate a camera around the animal [93]. A conical shape mirror was also proposed to detect an entire surface of the animal in one acquisition step [94]. However, since the mirror-based schemes place mirrors right next to the animal to include different directional views in the camera's field of view, the schemes are prone to generate multiple reflections of photons between the animal surface and highly reflective mirror surfaces. Consequently, the paths of the detected light become ambiguous and the accuracy of raw measurement data decreases.

In addition, the direct collection of signals from the animal surface requires the information of the boundary to involve the collected data into image reconstruction processes. The surface geometry extraction is one of the major difficulties in full noncontact imaging system implementations, together with co-registration of geometrical information of illumination and detection points on the animal surface.

In reconstruction algorithm development, researchers have begun to use the equation of radiative transfer (ERT) as a light propagation model. Though diffusion approximation to the ERT is a good approximation in many cases, ignoring angular dependence of emitted signals can lead to inaccurate results in media that are optically thin and dominated by boundary effects, e.g., small animals. Kienle et al also showed that scattering by aligned cylindrical microstructures like myofibrils, axons, or collagen fibers results in anisotropic light propagation in tissues [95]. Thus,

the use of isotropic models for determining optical properties in anisotropic tissues can generate inaccurate reconstruction results.

Furthermore, Gao and Zhao demonstrated that using the ERT and angular-resolved measurement data; image reconstruction results can be substantially improved [96]. However, all current measurement systems use integrated signals over all angles within a detector's numerical aperture and do not consider angular-dependent exit of light from tissues.

1.4.3 Commercially Available Small Animal Optical Imaging Systems

Though the systems for tomographic imaging have advanced as described in Section 1.4.2, the majority of tomographic imaging systems have been prototypes developed in laboratories. All available commercial small animal imagers are still limited to camera based 2D planar imaging.

As shown in Table 1-3, commercial small animal imagers mostly employ CCD cameras as detectors and an epi-broad beam illumination scheme to measure emitted signals. This scheme only allows for images of emitted light intensities on the tissue surface but no information about the volumetric distribution (i.e., depth and strength) of fluorescent probes inside tissues. This results in highly surface weighted images and leads to inaccurate measurement of deeply seated fluorescent probes. On the other hand, high sensitivity, high throughput up to 5 mice with one single acquisition and easy operation setups are attractive to many biomedical researchers. Recently, a few commercial imaging systems began to provide tomographic reconstructions using similar imaging schemes.

To achieve multi-directional projection data for tomographic reconstructions, commercial systems utilized multiple detectors or mirrors. The most recently developed commercial imaging system, BioFLECT (TriFoil Imaging, CA) in Table 1-3 achieves a 360° multi-directional view

using 48 photodiode detectors on a rotational gantry instead of using cameras as detectors. The Maestro 2 In vivo imaging system (two side mirrors, PerkinElmer Inc.) and the PhotonIMAGER^{TM} (two mirrors, Biospace Lab, France)) simply employ multiple flat mirrors to include side views of the animal in a single image.

Table 1-3. Summary of the main technical features associated with high-end commercially available in vivo whole-body fluorescence imaging systems (from the reference [30] and the companies' websites)

Instrument (Company)		NightOWL II - LB 983 NC 100 (Berthold Tech.)	Maestro (Perkin-Elmer)	KODAK in vivo imaging system (Carestream Health)	Pearl Imager (Li-COR Biosciences)	iBox (UVP)	Optix MX3 (ART)	IVIS Spectrum (Caliper Life Sciences)	FMT 2500 LX (VisEn Medical)	BioFLECT (TriFoil Imaging)	PhotonIMAGER™ (BIOSPACE LAB)
Applications	Planar mode	Epi-	Epi-	Epi-	Epi-	Epi-	Epi-	Epi- & trans-	Epi-	Epi- & trans-	Epi- & trans-
	3D Tomography	No	No	No	No	No	Yes (Topography)	Yes (Diffusion Model)	Yes (Diffusion Model)	Yes (Limited ERT)*	Yes (Limited ERT)*
	Surface Rendering	No	No	No	No	No	Yes	Yes	Yes	Yes	Yes
Illumination	Light source	Lamp	Lamp	Lamp	Laser diodes	Lamp	Pulse laser & external CW tunable laser	Lamp	Laser diodes	Laser diodes	Lamp
	Method	Epi-broad beam	Epi-broad beam	Epi-broad beam	Epi- (NA)	Epi-broad beam	Epi-raster scanning	Epi-broad beam & trans-aster scanning	Epi-broad beam & trans-laser scanning	Epi- & trans- laser scanning	Epi-broad beam
Detection	Technology	CCD (1.0 MP)	CCD (1.4MP)	CCD (4.2 MP)	CCD (NA)	CCD (4.2 MP)	PMT (TCSPC)	CCD (4.2 MP)	CCD (NA)	48 Photodiodes	ICCD (NA)
	Filtering	300-1050 nm (selectable, 4 filter positions)	500-950 nm (Liquid crystal tunable filters)	440-830 nm (selectable, 4 filter positions)	700, 800 nm (selectable, 2 filter positions)	450-850 nm (5 filter positions)	450-900 nm (selectable, 24 filter positions)	300-1100 nm (selectable, 28 filter positions)	700, 800 nm (selectable, 8 filter positions)	500-850 nm (selectable, 11 filter positions)	450-1000 nm (selectable, 10 filter positions)
	FOV (optics)	1x1 - 25x25 cm^2	11.2x8.4 cm^2	2x2 - 20x20 cm^2	12x9 cm^2 (NA)	8x8 - 30x30 cm^2	20x8.4 cm^2	4x4 - 25x25 cm^2	5x5 and 8x8 cm^2	Axial 120 mm	22x16.5 - 32x24 cm^2
	Simultaneous Multiple views	-	3 directions	-	-	-	-	-	-	360°	4 directions

**Proprietary finite-difference code – full details not known.*

Table 1-3. Continued

	Instrument (Company)	NightOWL II - LB 983 NC 100 (Berthold Tech.)	Maestro (Perkin-Elmer)	KODAK in vivo imaging system (Carestream Health)	Pearl Imager (Li-COR Biosciences)	iBox (UVP)	Optix MX3 (ART)	IVIS Spectrum (Caliper Life Sciences)	FMT 2500 LX (VisEn Medical)	BioFLECT (BIOSCAN)	PhotonIMAGER™ (BIOSPACE LAB)
Multi-modal Imaging	Biolumi-nescence	Yes	-	-	-	-	Yes	Yes	-	-	Yes
	Multi-modal	CT, MRI, PET/SPECT, US	-	X-ray	-	-	CT-coupling stage	CT, MRI, digital mouse atlas	Adapters (CT, MRI, PET/SPECT)	X-Ray, CT	X-ray, CT modules
	Coregistration software	Yes	-	Yes	-	-	Yes (to CT imaging)	Yes	Yes	Yes	Yes
Animal Handling	Number per image	Up to 2	Up to 3	NA	1	Up to 3	Up to 5	Up to 5	1	1	Up to 5

Chapter 2

IMAGING OF ANTI-ANGIOGENIC DRUG EFFECTS

2.1 Anti-angiogenic Cancer Therapy

To explore the potential and limitations of currently commercially available optical small animal imaging systems, I used the Maestro2 In Vivo imaging system (CRi, Inc., Woburn, MA) to perform both bioluminescence and fluorescence imaging studies. In particular this system was employed to monitor early tumor vascular response to a drug therapy. This is a common area of preclinical imaging and a likely future application of any new small animal imaging system.

Angiogenesis, the growth of new blood vessels, is an important process for the proliferation and metastasis of tumor cells. Blood vessels surrounding the tumor cells provide pathways for supplying oxygen, nutrients, and immune cells, and for removing waste matter from the tumor. In addition, tumor cells can penetrate through blood or lymphatic vessels and can spread to distant organs through the intravascular network. Judah Folkman was the first to hypothesize that inhibition of tumor angiogenesis can be a therapeutic method for cancer treatments [97]. Since then numerous studies have addressed the effects of angiogenesis in tumor progression [98, 99], considerable efforts have been devoted to developing anti-angiogenic drugs [100-103]. Several potential anti-angiogenic drugs, which attack the vascular endothelial growth factor (VEGF), have been tested since the late 1990s. The first anti-angiogenic drug, bevacizumab (Avastin®) was approved by the Food and Drug Administration (FDA) in 2004 for cancer treatments [104, 105].

Bevacizumab-based treatments have shown a diverse array of responses including recurrence of angiogenesis via another signaling pathways over time [106]. In order to obtain a

robust quantification of the angiogenic or anti-angiogenic responses, reliable monitoring methods have been demanded [107]. Additionally, due to the expensive cost of the therapy, non-invasive imaging methods for investigating the early responses of treatments could be very useful for deciding the optimal therapeutic regimen for patients [108]. While many different methods have been tested, using a cost-effective optical imaging method for this application is still challenging [109, 110].

For this exploratory study, I hypothesized that the responses of anti-angiogenic treatment are related to the simultaneous changes of vascular density, perfusion and permeability [111]. Furthermore I expect that dynamic fluorescence imaging of the circulation of a fluorescent probe may extract more information compared with static fluorescence imaging. However, since dynamic fluorescence imaging using a non-targeted fluorophore cannot differentiate tumor areas from other benign tissues, bioluminescence imaging provides tumor boundaries for the dynamic signal analysis [112, 113].

2.2 Dynamic Fluorescence Imaging for Vascularization Monitoring

Both dynamic fluorescence and bioluminescence imaging methods require an intravenous (IV) or intraperitoneal (IP) injection of chemical compounds before imaging. However, excessive injection of these chemical compounds at a time can be burden to the functions of kidneys, lungs and other organs and can cause death of the recipient animals. The sensitivity and parameter setup of the imaging system are also important in determining the injection volume of chemical compounds. Thus, the imaging protocol and the injection volumes for each imaging method were carefully designed and determined based on other published dynamic imaging researches and preliminary tests with the imaging system [114].

2.2.1 Tumor Model

A Human Ewing sarcoma (SK-NEP1) cell line, which has already shown nearly complete inhibition of tumor growth under anti-angiogenic treatment [115], was engineered to express bioluminescence. After anesthetizing a mouse with IP injection of a mixture of Ketamine (50 mg/kg) and Xylazine (5 mg/kg), the left flank of the mouse was sterilely prepared and incised to expose the left kidney. About 10^6 tumor cells (SK-NEP1-luc) in 0.1 ml of Phosphate-buffered saline (PBS) were injected with a 25-gauge needle into the kidney. Then the flank muscles and the skin were closed with a suture and staples respectively. In total, 9 NCR nude mice bearing Ewing sarcoma cells were prepared 3-4 weeks prior to the experiments. Subsequent tumor growth was monitored bi-weekly by bioluminescence imaging with the Xenogen IVIS imaging system (Caliper Life Sciences, MA). The animals were treated with 20 mg/kg bevacizumab (IV injection) every three-day after the tumor weight reached approximately 1g.

2.2.2 Contrast Agent and Imaging System

Indocyanine Green (ICG) is a water-soluble and non-toxic tricarbocyanine dye approved by FDA for human use. Also, ICG has been widely used as an optical contrast agent in the near infrared wavelength range. The fluorescent properties of ICG, such as excitation and emission spectrum shown in Figure 2-1 have been well characterized in many preclinical and clinical applications. One of the well-known features of ICG is that it binds to albumin almost completely in plasma. Consequently, the effective molecular weight of ICG-albumin binding reaches 67 kDa so that ICG behaves like a macromolecular contrast agent in plasma. In studies of the dynamics of ICG, it was shown that the uptake slope and the peak value of the ICG time-series traces are correlated with the permeability of the vasculature. In other words, ICG dynamics showed higher vascular

permeability in leaky tumor vasculature than in normal vasculature. Using optical spectroscopy and magnetic resonance imaging demonstrated that a necrotic tumor shows lower peak concentration and lower permeability of ICG.

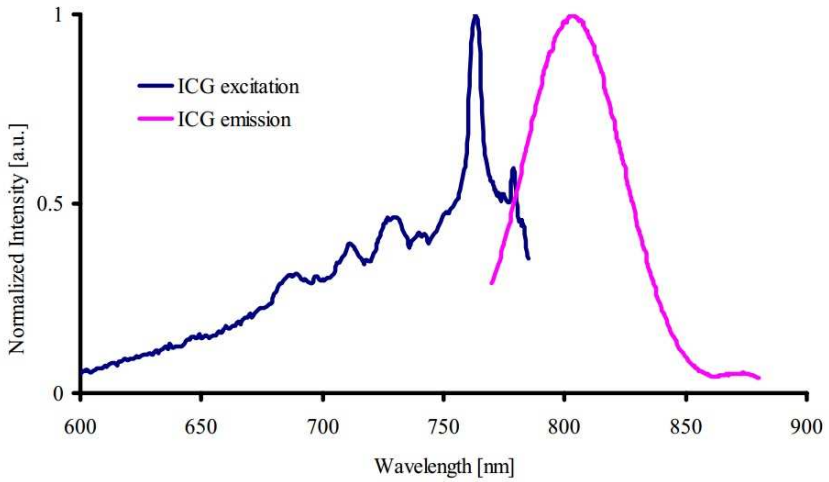

Figure 2-1. Normalized fluorescence spectrum of indocyanine green (ICG) [116]. The absorption of ICG depends on its concentration and solute. The spectrum was taken under the conditions: (1) 1-μM concentration of ICG was dissolved in deionized ultra-filtered water; (2) the excitation spectrum was taken with the emission monochromator at 830 nm; (3) the emission spectrum was taken with the excitation monochromator at 785 nm.

I conducted both bioluminescence and dynamic fluorescence measurements with a commercial imaging system, Maestro 2 In Vivo Imaging system (CRi, Inc., Woburn, MA). This system can cover any fluorescent wavelengths between 500 – 950 nm by using a tunable filter set and a Sony ICX285 camera. The maximum frame rate of this imaging system is 10 frames/sec. A maximum of three mice can fit into the camera's field of view. Using Maestro's C3 mirror accessory, three sides of an animal can be captured simultaneously. In addition, the time-based Dynamic Contrast Enhanced (DyCE) technique is embedded in the software package of this system. This software can provide an anatomical organ map by using time series data and different interaction aspects between contrast agents and tissues [117].

Figure 2-2. Photograph of Maestro 2 In Vivo Imaging system

2.3 Data Acquisition

2.3.1 Imaging Protocol

The imaging procedure followed the timetable shown in Figure 2-3. At first, the mouse was anesthetized and the tail vein was catheterized with a customized catheter (a 50 cm long PE10 tubing with a 30-gauge needle at one end). To obtain a time-series data from the chemical injection, the imaging began at the same time as the injection of chemical compounds. Therefore, ICG was delivered from the outside of the imaging system to the mouse inside the imaging chamber by using the catheter through a small hole on the side of the imaging system. While under the anesthetization of a gas mixture of 1.5% isoflurane and oxygen, the catheterized mouse was placed between two 45-degree angled mirrors on the imaging stage to get three different directional views. The breathing rate of the mouse was maintained around 60 breaths/minute.

Bioluminescence imaging began two minutes after the IV injection of 70μL luciferin. IV injection of luciferin was used because the commonly used IP injection of luciferin did not provide enough signals in preliminary tests with the Maestro2 imaging setups. To remove

residual bioluminescence signals from a mouse before the dynamic fluorescence imaging, the mouse was kept in place without changing its position and posture for 25 minutes. The autofluorescence of the mouse body and the residual of bioluminescence signal were measured 5 minutes before the fluorescence imaging using the same setup for the dynamic fluorescence imaging. 35 minutes after the luciferin injection, 200 μM, 60 μL ICG was injected through the catheter. The dynamic fluorescence imaging began at the same time point of the ICG injection.

This procedure was repeated at four different time points. After the baseline measurement, 0.2 mL bevacizumab was administered through the catheter. Then, the imaging experiments were repeated at 1, 24 and 72 hours after this initial treatment. For the same mouse, the same batch of ICG was used and the signal intensity of pure ICG was also measured before each experiment to calibrate the intensity degradation.

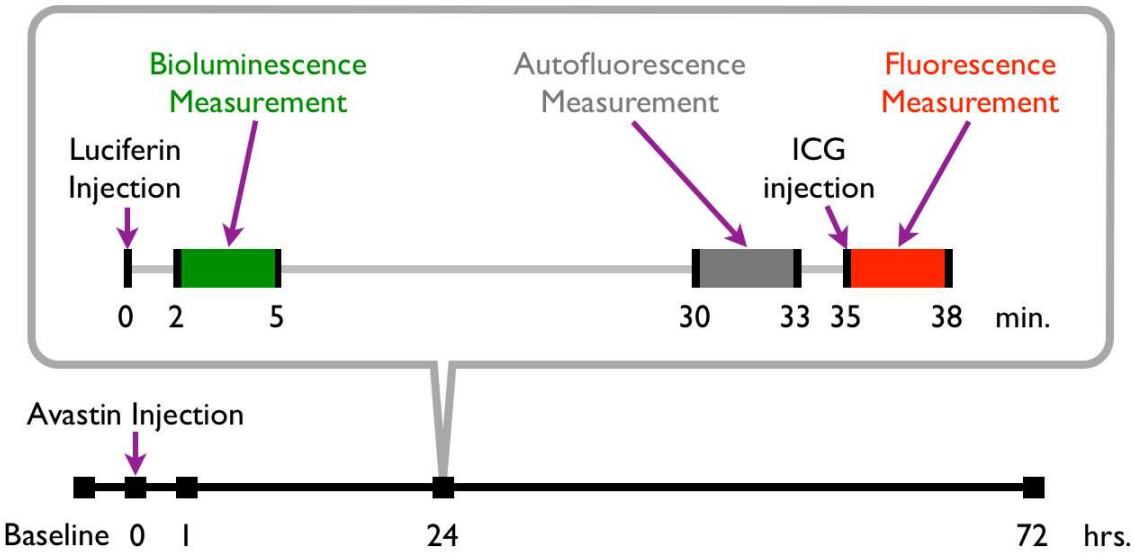

Figure 2-3. Timetable for the imaging procedure

2.3.2 System Setup

For the bioluminescence imaging to define the tumor area in the mouse body (Figure 2-4), I employed a 560 nm (±10 nm) emission filter and the low-light-mode setup of the imaging system. A 3-minute exposure time was chosen based on the examination of bioluminescence signal levels depending on the exposure time. The dynamic fluorescence images in Figure 2-5 were obtained with 704 nm (± 20 nm) excitation and 820 nm (±10 nm) emission filter sets and 65 msec exposure time. 4×4 binning was used for the full 3.3"×4.4" field of view. By imaging at a frame rate of 5 frame/sec, a total of 900 frames of time series data were acquired for 3 minutes.

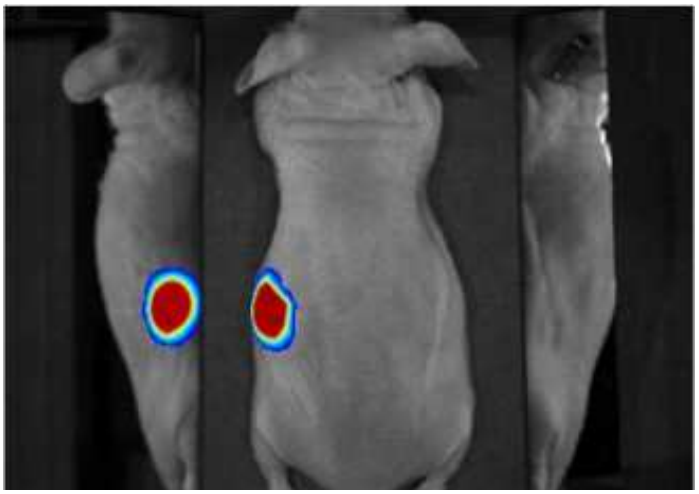

Figure 2-4. Bioluminescence signals on a mouse surface

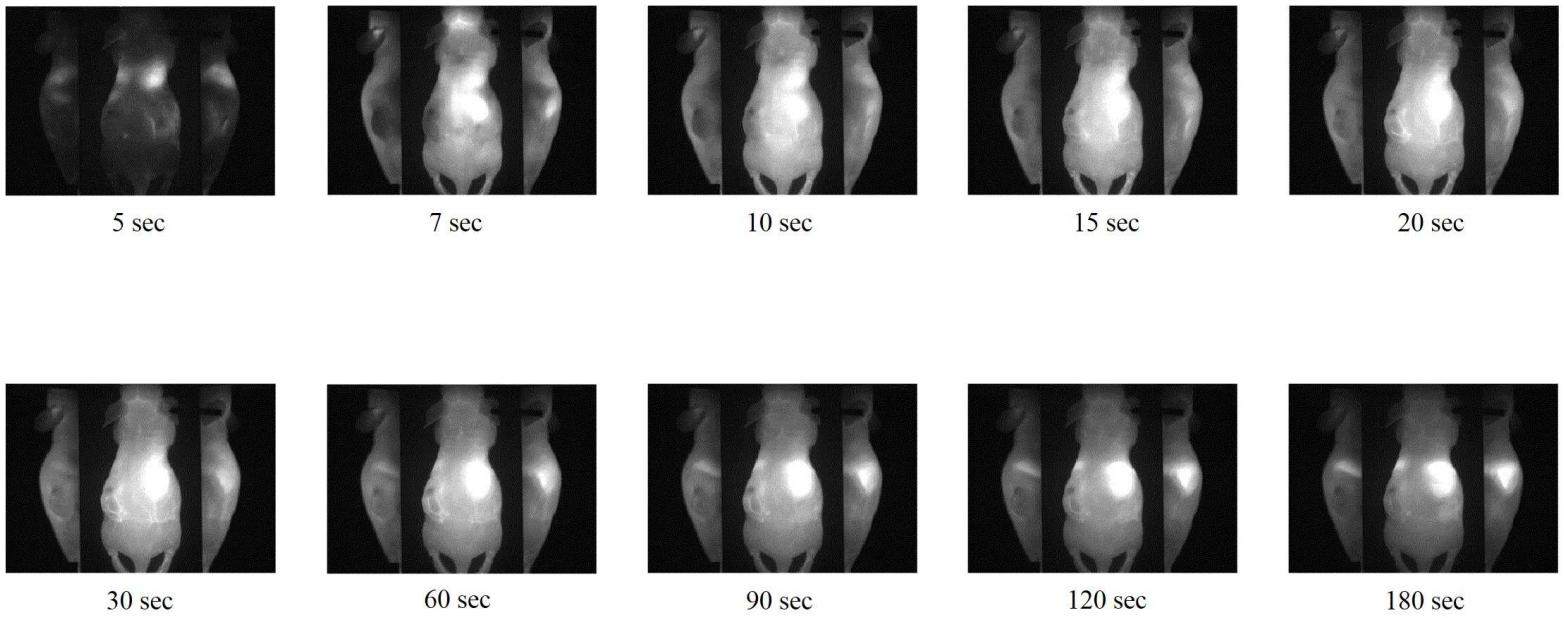

Figure 2-5. Fluorescence signals at different time points

2.4 Data Analysis

2.4.1 Tumor Boundary

The obtained tumor boundary is shown in Figure 2-4. I compared Figure 2-4 to the color-coded organ and tumor map in Figure 2-6a. Figure 2-6a was generated by the DyCE technique of the imaging system, to double-check the tumor area on the mouse surface.

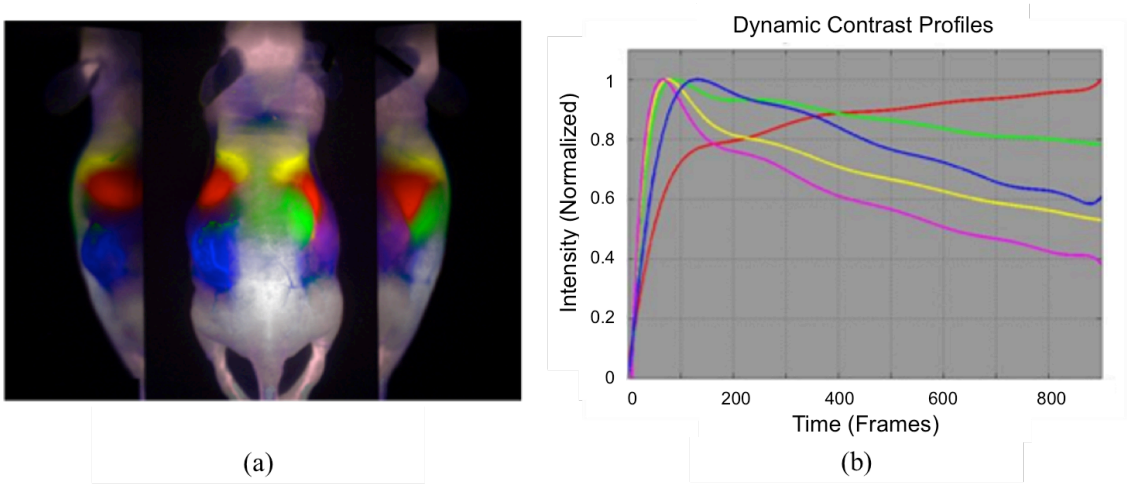

Figure 2-6. Color-coded organ map using the DyCE technique (a) generated color-coded organ and tumor map based on ICG time trace similarity and (b) ICG time traces of each organ (blue-tumor, red-liver, yellow-lungs, green-kidney, and pink-brain)

Although the boundary of tumor area and the organ map were not exactly the same, the tumor area defined by bioluminescence measurements was interpolated onto the color-coded organ map. The mismatch of the boundaries comes from the characteristics of the DyCE technique. The color-coded organ map is generated mathematically based on the Principle Component Analysis (PCA) and non-negative least square fitting of the uptake and clearance similarity of a fluorophore. Thus, depending on the choice of a reference pixel(s) in the estimated organ areas, the organ boundary in the color-coded map can slightly change due to this nature of

the DyCE technique. In the dynamic fluorescence signal analysis, the tumor areas defined by bioluminescence imaging were used, which provided more precise tumor boundaries.

2.4.2 Dynamic Signal Analysis

The signal intensities of pixels in each image were normalized by the average signal level of all pixels in each frame. Figure 2-7 depicts ICG time trace changes in the tumor area at different time points. After the initial bevacizumab treatment, the time traces (red-1 hr., blue-24 hr., green-72 hr.) showed slower uptake and lower peak signal intensity of ICG in comparison to the baseline (black).

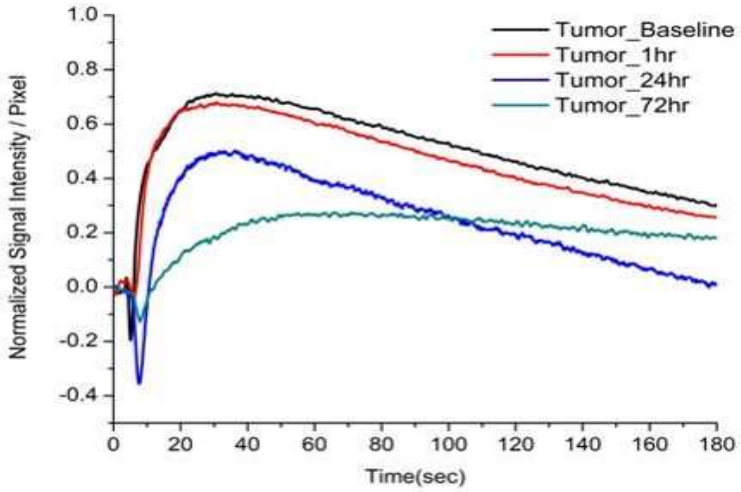

Figure 2-7. ICG time trace changes in tumor area

However the experimental conditions such as the hemodynamic status of the mice and injection timing cannot be exactly the same at every measurement in the longitudinal study. Therefore, ICG time trace changes in the brain area defined by the color-coded organ map were also extracted and compared to those in the tumor area to check the influence of experimental conditions depending on measurement time points. In contrast with the tumor, the ICG time

traces in brain area (Figure 2-8) typically showed similar signal traces for measurements performed at different time points.

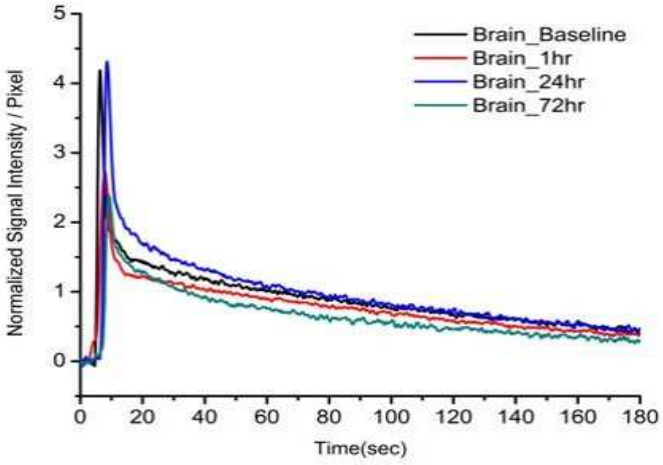

Figure 2-8. ICG time trace changes in brain area

Next, by fitting these normalized time traces to equation 2.1 and 2.2, the slope of uptake (b), and the clearance time constant (t1), and the peak intensity (P), of the ICG kinetics in tumor and brain areas were extracted.

$$y = a + b \times X \tag{2.1}$$

$$y = A \times \exp\left(-\frac{X}{t1}\right) + y0 \tag{2.2}$$

To eliminate the influence of the experimental conditions at different time points, the ICG time trace parameters of the brain were used as references to calculate the ratio of extracted parameters of the tumor.

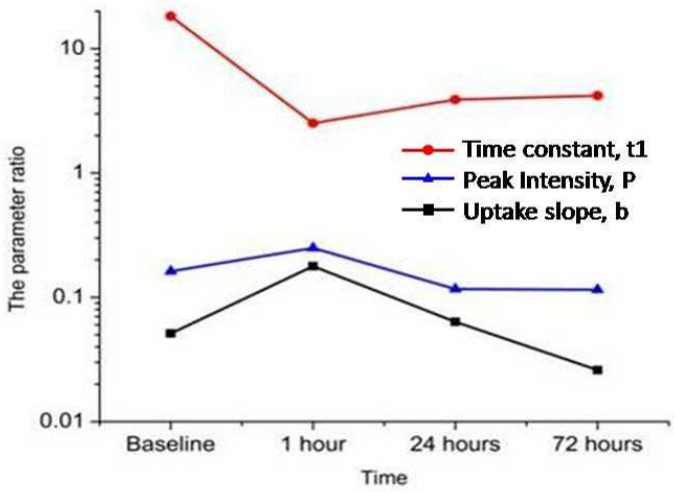

Figure 2-9. Extracted parameter ratio changes

As shown in Figure 2-9, 24 and 72 hours after the anti-angiogenic treatment, the uptake slope and peak intensity decreased and the clearance time constant increased over three days as compared with those at the1 hour time point.

In addition to the ICG kinetic parameter comparison, I also extracted the integrated signal levels in different organs such as tumor, lung, and brain. Organ areas were defined by the DyCE technique except for tumor area, which was defined by bioluminescence measurement. All normalized signal intensities in each organ area of the entire 900 image frames were summated and the average intensity per each pixel in the organ areas was calculated. Since this integrated signal intensity is proportional to the vascular density in an organ area, Figure 2-10 describes that the tumor area showed the decrease of vasculature over three days. This is a different trend compared with the lung and brain areas.

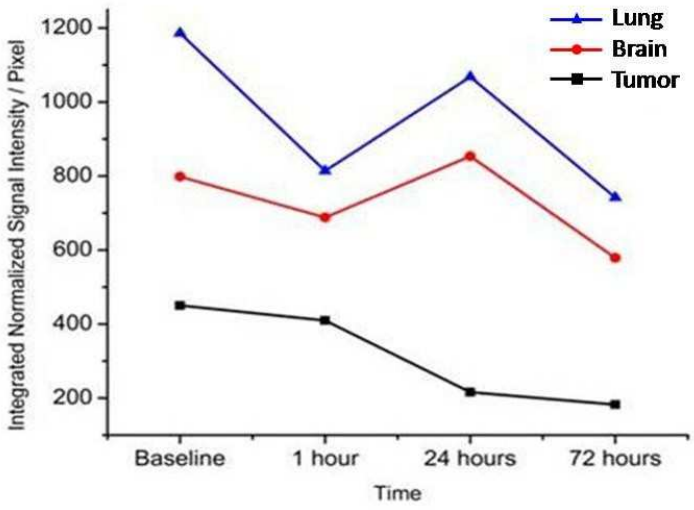

Figure 2-10. Integrated signal level changes in the different areas (blue-Lung, red-brain, and black-tumor)

The lectin perfusion studies in the histological analysis showed a similar decrease of vasculature in tumor area like Figure 2-11. This result also corresponds with the changes measured by DOT and MRI T2 relaxometry [118].

All observations are related to the alleged vascular normalization, which can be explained by decrease in the permeability of tumor vasculature. These results are in agreement with the studies of Cuccia et al [112] and Tong et al [113].

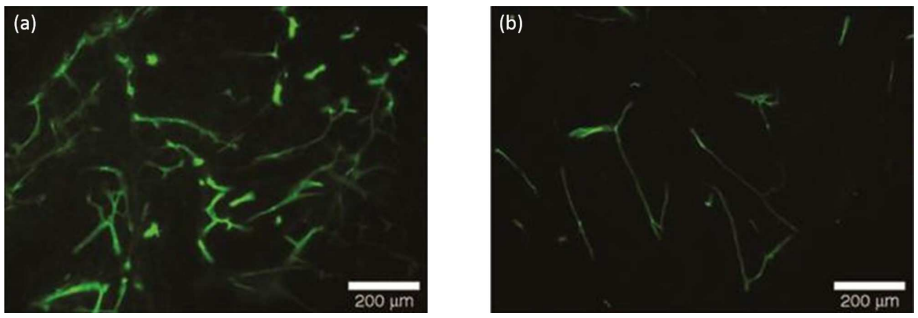

Figure 2-11. Lectin perfusion images of tumor area in (a) day 0 and (b) day 3 after the treatment

2.5 Conclusion

This preliminary study explored the potential of dynamic fluorescence imaging for monitoring tumor vascular responses during anti-angiogenic drug therapy in preclinical studies. Bioluminescence imaging provided well-defined tumor areas for the fluorescence data analysis. The chemical kinetics of a non-targeted fluorophore, ICG, facilitated to extract the information of vascular permeability in the tumor area. Both imaging methods are well known and commonly used in biomedical research. Due to the simplicity and low cost, this combined method can be easily and cost-effectively applied for obtaining vasculature information of tumors.

While this study showed that some information about the hemodynamics and vascular structure changes could be obtained, limitations of 2D planar imaging were also obvious. Since the Ewing sarcoma grew so rapidly in the imaging time period (72 hrs.), tumor sizes at baseline and 72hour later were largely different. Since 2D planar imaging has a limited penetration depth, it could not fully probe the hemodynamic changes in deeply positioned tumor areas and showed only the vascular changes near the detectable surface area. As a result, the reliable quantification of vascular responses covering the entire tumor volume could not be achieved.

Chapter 3

DEVELOPMENT OF A FREEQUENCY-DOMAIN NON-CONTACT SMALL ANIMAL IMAGING SYSTEM

3.1. Requirements for the New Small Animal Imaging System

Based on the experience of the preliminary in vivo small animal study with the Maestro 2 imaging system, the desirable characteristics of a new system were identified and listed based on their priorities:

(1) Full projection coverage

To acquire epi- and trans-illumination data at the same time, the system should allow for simultaneous acquisition of multi-directional projection data. The animal should be imaged in its natural posture through the imaging procedures. The CCD camera should be fixed at one position due to its heavy weight and complicated connections with other electrical components. In addition, the camera's field of view should cover the entire animal size.

(2) Minimization of measurement error

Using optical components to achieve the first design goal may cause errors in the accurate signal measurements. For example, unwanted optical paths and multiple reflections between mirrors and the animal surface can degrade the accuracy of the measurements. Thus these factors should be considered and eliminated (or minimized) in the system design.

(3) Free space source illumination

The imaging setup should allow for free space source illumination at any point on the animal's surface. In addition, the source illumination components and their movements should not obstruct the data acquisition by the CCD camera.

(4) Surface boundary extraction

The surface scanner should extract the animal's surface geometry without changing the position and posture of the animal during the imaging process. It should also be integrated into the imaging system for easy operation.

(5) Other minor considerations

Convenient access and anesthetization of the animal through the imaging process are considered together with fewer moving components in the imaging system. The feasibility of combining the system with other gantry-based imaging modalities such as MRI, CT, PET, and SPECT is also taken into account.

The new small animal imaging system was developed based on the above requirements. It consists of four main parts: (1) A light input unit for generating and positioning an intensity modulated laser beam, (2) an imaging head for projecting omni-directional views of the animal surface onto a CCD camera, (3) a detection unit for measuring amplitude modulation and phase shift of the collected light, and (4) a surface scanner for extracting a surface geometry of the animal being imaged. The schematic overview of the system is shown in Figure 3-1.

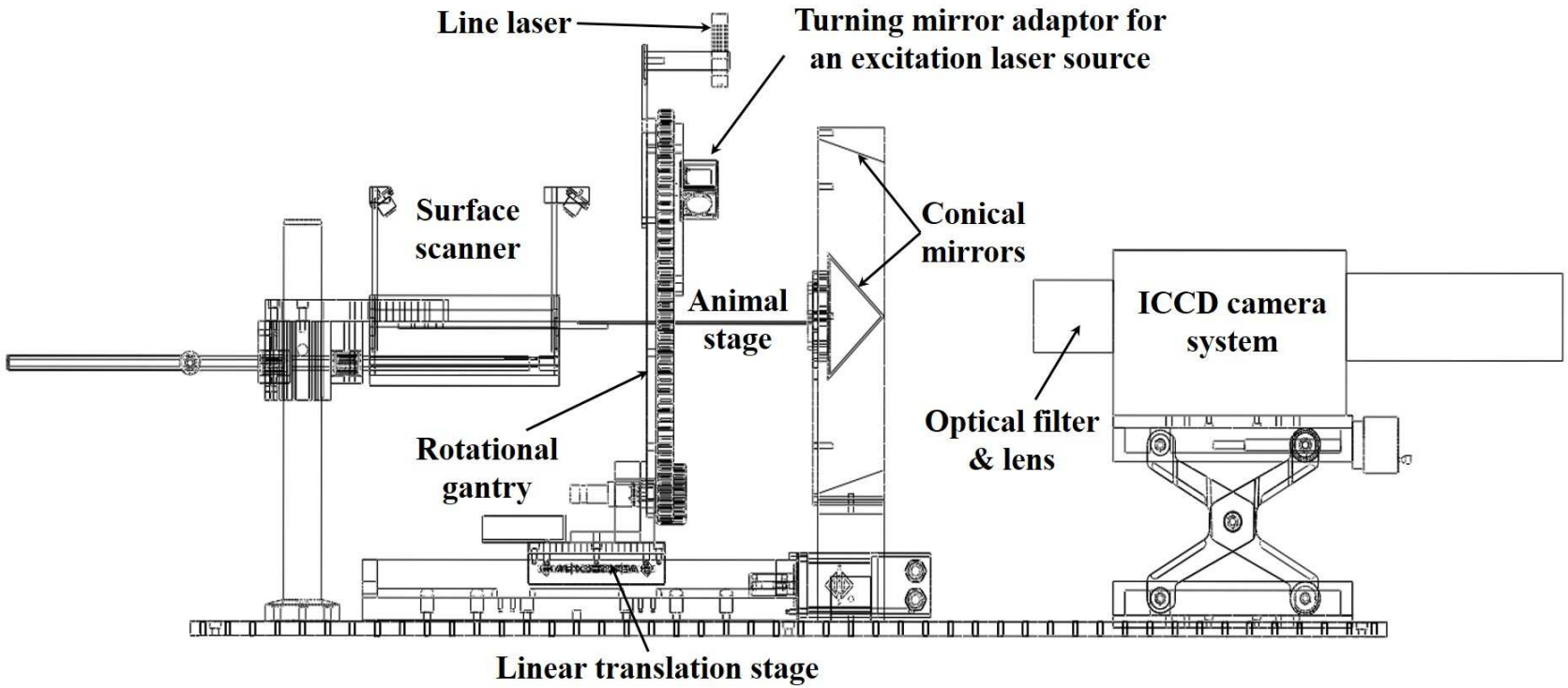

Figure 3-1. Schematic overview of the FMT small animal imaging system. The light input unit consists of a mirror adaptor, a rotational gantry, a linear translation stage, and laser diodes and drivers for generating light at various wavelengths (not presented in this view). The two conical mirrors are the main components of the imaging head that collect light from the animal and transfer it to the ICCD camera system. The detection unit is composed of filter sets, a lens, and the intensified CCD camera system including signal generators and a high rate image intensifier controller (not presented in this view). A line laser on the rotational gantry is the component of the surface scanner.

3.2 Light Input Unit

The role of the light input unit is to deliver intensity modulated light sources to the target animal to measure the intensity modulation and phase shift of light that passes through the animal body for frequency domain data acquisition.

3.2.1 Light Source

The light sources of the input unit are compact semiconductor laser diodes (LDH-M-C Series, PicoQuant GmbH, Germany). The unit has five different wavelength laser diodes of visible and near-infrared light at $\lambda 1$ = 475 nm, $\lambda 2$ = 661 nm, $\lambda 3$ = 757 nm, $\lambda 4$ = 828 nm, and $\lambda 5$ = 926 nm. Electrical current initiates the laser emission at a unique wavelength. Since the wavelength of the laser and the stability of output power depend on the diode temperature, each laser head is equipped with a thermoelectric cooler for control of the operation temperature.

The laser driver (MDL 300, PicoQuant GmbH, Germany) provides the intensity modulation for the laser with internal or external modulation frequencies that range from 100 kHz up to 2 GHz. The output power is regulated by a control loop that compares the laser power setting and the monitor diode current. The modulation depth of the laser output can be adjusted by the voltage of the external modulation signal and the modulation depth control on the front panel of the driver. The external source of modulation frequencies is the signal generator (2023A, Aeroflex Inc., NY) covering the frequency ranges from 9 kHz to 1.2 GHz.

Table 3-1. Specification of Laser diodes

	Laser 1	Laser 2	Laser 3	Laser 4	Laser 5
Model No.	LDH-M-C-470	LDH-M-C-650B	LDH-M-C-760	LDH-M-C-830	LDH-M-C-930
Average Power	8 mW	22.8 mW	8 mW	15.3 mW	33.3 mW
Average wavelength	474.6 nm	661 nm	757.3 nm	828 nm	926 nm
Spectral width	0.54 nm		0.85 nm		

For the flexibility of the laser illumination, all laser heads are coupled with optical fibers. A fiber coupler is directly mounted to the laser head and a 2 m long fiber optic patch cable is connected to the coupler. To optimize the coupling efficiency for the output power, multimode fibers were chosen (>80% coupling efficiency compared with >40% of single mode), an 8° angled output Ferrule Connector (FC/APC) was used to avoid back-reflections of laser emission into the fiber, which could influence the stability of the output. After passing through the optical fiber, the collimated laser beam at the laser head diverges. Therefore, a collimator (60fc-4, Schäfter + Kirchhoff GmbH, Germany) was attached to the end of the patch cable to converge the laser beam to have a 1~2 mm diameter. Then the collimator was clamped to the mounted turning mirror (CM1-P01, Thorlabs, Inc. NJ) on the rotational gantry in the next light source-positioning unit.

3.2.2 Light Source Positioning Unit

The laser should be able to precisely illuminate any spot on the animal surface. Additionally, since the CCD camera detects the entire surface of the small animal simultaneously, the components for the source positioning and their movements should not obstruct data acquisition

by the CCD camera. Considering the specification of the imaging head for the small animal and the constraints for the source-positioning unit, a rotation gantry combined with a linear translation stage was applied to the positioning unit design (Figure 3-2).

Figure 3-2. Light illumination using the source-positioning unit

The rotational gantry provides 360° angular freedom for the laser illumination around the animal. The size of the gantry was chosen so that it would be large enough to be out of field of view of the camera (gray areas in Figure 3-5). Three different size gears, a turntable ring, a brushless DC motor, and a motor controller were employed to implement the rotation of the gantry. As shown in Figure 3-2, the collimator of an optical patch cable from a laser head was clamped to the turning adaptor with a protected silver coated mirror (CM1-P01, Thorlabs, Inc., NJ). The adaptor was mounted on the large ring gear (inside bore Ø 296 mm, 120 teeth), which was attached on a turntable ring. The turntable ring and a planetary gear are affixed to the mount and the mount supports the weight and rotation of the components. To rotate the large ring gear, a brushless DC motor (40 Watt, EC16, Maxon Precision motors Inc., USA) is used. The torque

of the motor is delivered to the large ring gear via a planetary gear head (84:1, GP16, Maxon Precision Inc., USA) and a spur gear (16 teeth, 54 mm outside ∅, Quality Transmission Component, NY). The gear ratio between the motor and the large ring gear is 630:1. A motion controller (EPOS2 24/5, Maxon precision motors Inc., USA) operates the rotational movements with 0.25° resolution.

All components of the rotational gantry were mounted on a motorized linear translation stage (Pro115-05MM-200-TTM, Aerotech Inc., USA). A motion controller (Soloist CL, Aerotech Inc., USA) operates all linear displacements of the stage. A 200 mm travel range with 0.5μm resolution of the stage provides a full coverage of a whole mouse body and fine positioning of a laser beam in the longitudinal direction of the target animal. A LabVIEW graphical user interface on the host computer was developed to facilitate the control of all source-positioning components (Figure 3-4).

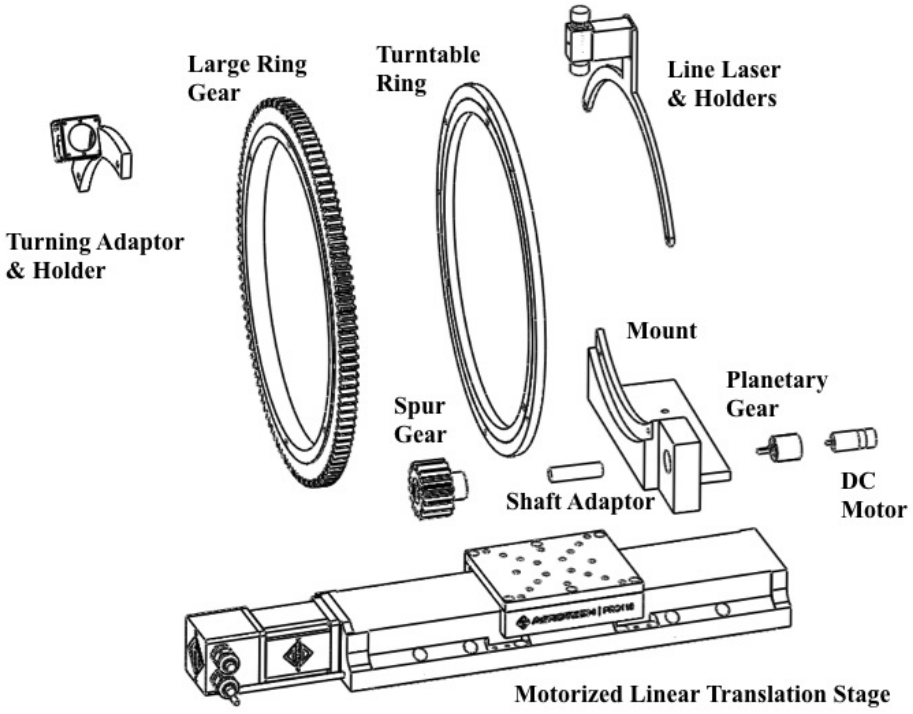

Figure 3-3. Disassembled components of the source-positioning unit

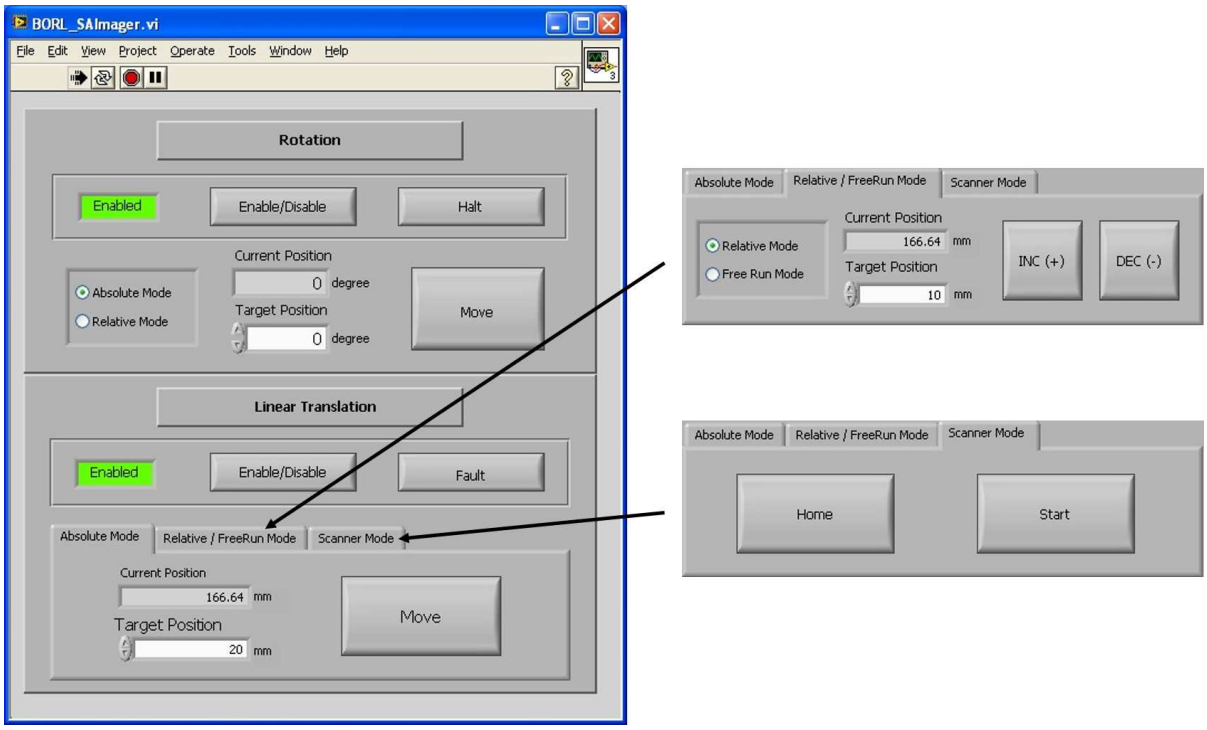

Figure 3-4. Screen shots of the user interface for the source-positioning unit

3.3 Imaging Head

3.3.1 Basic Concept of the Imaging Head

The main limitation of current non-contact imaging systems using a single camera is the limited projection angle of the measurement. To overcome this limitation and to achieve the listed design goals, I implemented a consecutive double reflection scheme using mirror components (from here imaging head) to obtain different viewing angles of the object being imaged. The basic configuration of the consecutive double reflection scheme uses two mirrors between the object and the detection camera for the half angle of the camera's view (Figure 3-5).

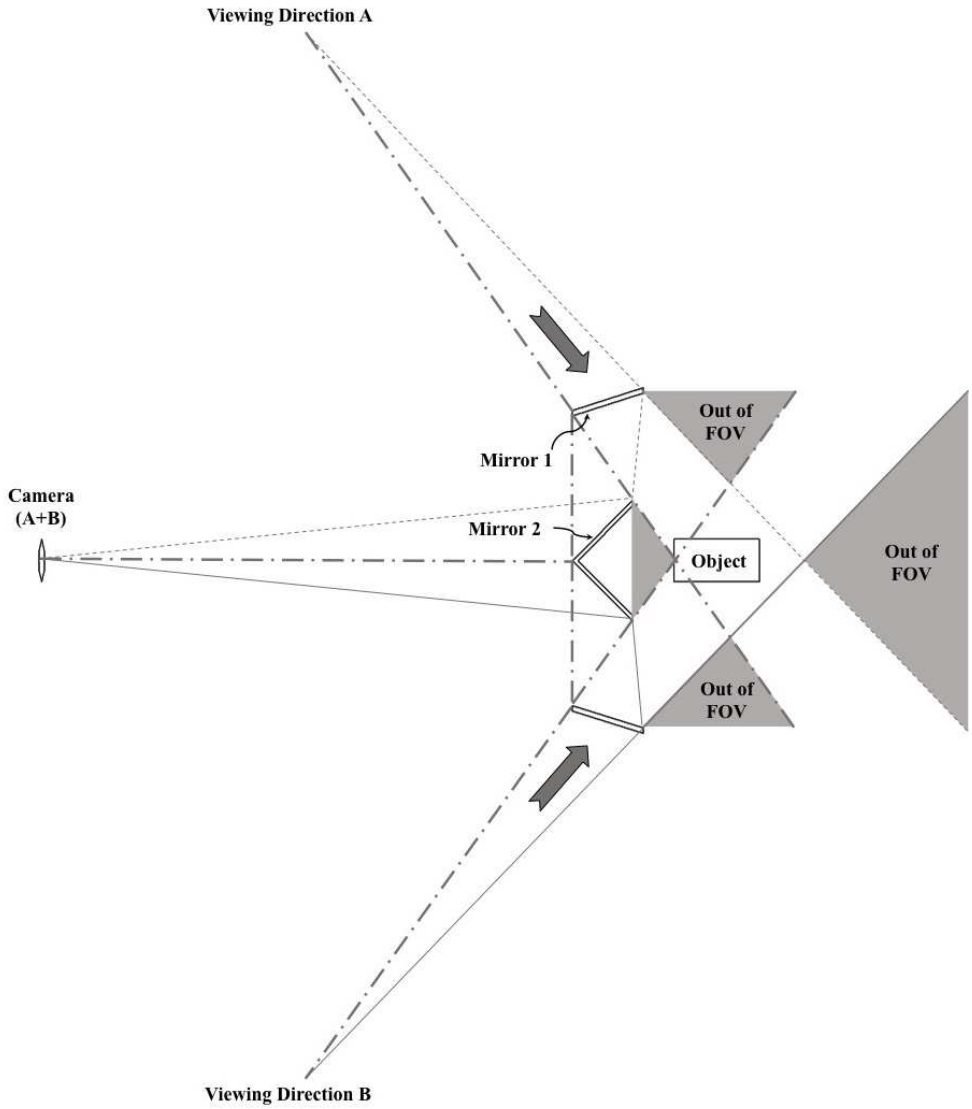

Figure 3-5. Double reflection mirror scheme (Cross-sectional View)

In this design, two mirrors are facing the object to be imaged and the detection camera respectively. Mirror 1, which faces the object, captures and reflects the optical signals emanating from the object to Mirror 2. Then Mirror 2, which faces the camera, projects reflected signals onto the detection camera. Accordingly, the upper half view of the camera has the viewing direction A, and the lower half view of the camera follows the same principle.

3.3.2 Specification of the Imaging Head for Small Animals

I extended the 2D cross sectional double-reflection mirror scheme for the imaging head in Figure 3-5 to three dimensions for small animals. To maximize the detection area of the animal surface, conical shape mirrors were chosen. This provides a full coverage of the entire surface of the animal.

I began the extraction of the mirror specifications and positions with measuring the viewing angle of the imaging system. The camera system, unlike ordinary cameras, has an intensifier between the camera lens (AF Nikkor 50 mm f/1.8D, Nikon, Japan) and the CCD camera to amplify weak light signals. For that reason, the real viewing angle of the CCD camera is influenced by the mismatch between viewing angle coverage of the lens and the photocathode screen size. I measured the camera's viewing angle (11.58°) using a grid paper and the thin lens equation. Furthermore, the dimensions of the cylinder that mimics an animal are given by a 40-mm diameter and 80-mm length. In addition, the bias angle of the mirror facing the CCD camera is predefined as 45°. Under the given conditions and assumptions, 7 parameters $(\overline{ABCD}, \overline{BC}, \overline{DE}, M1, M2, \alpha, \gamma)$ defined in Figure 3-6 were calculated.

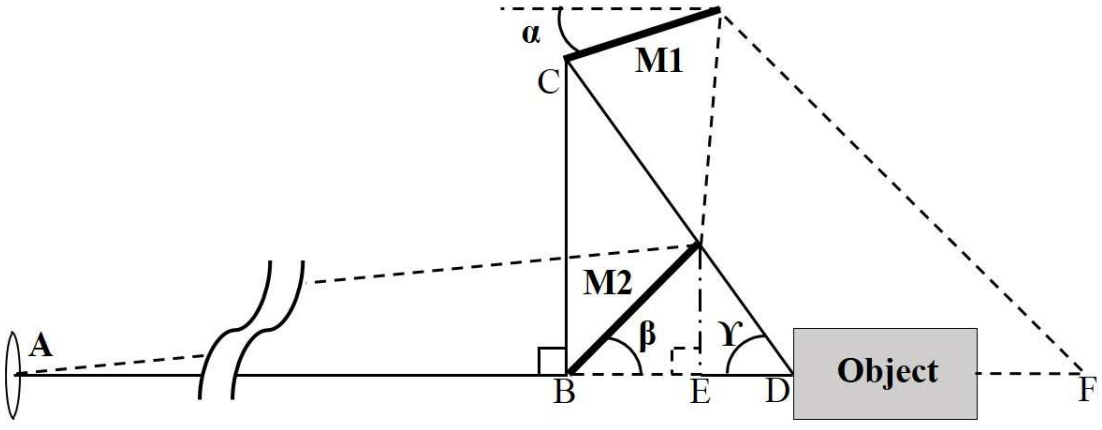

Figure 3-6. Parameters for the conical mirror design. The animal shape was assumed to be a cylinder.

The departure angle δ at the optical center A is 5.79° from the measured viewing angle. The distance from the optical center to the object, $\overline{ABCD}$, and the bias angle, γ, were set as independent variables in the ranges between 500 mm and 1400 mm and between 30° and 60° respectively. $\overline{BC}$, $\overline{DE}, M1, M2, \alpha$ were calculated based on the variation of $\overline{ABCD}$ and γ. Each variable can be calculated from:

$$\overline{AB} = \frac{M2}{\sqrt{2}}\left(\frac{1}{\tan(\delta)} - 1\right) \tag{3.1}$$

$$\overline{BC} = \frac{M2}{\sqrt{2}}\left(\tan(\gamma) + 1\right) \tag{3.2}$$

$$\overline{CD} = \frac{M2}{\sqrt{2}}\frac{\left(\tan(\gamma) + 1\right)}{\sin(\gamma)} \tag{3.3}$$

$$\overline{ABCD} = \overline{AB} + \overline{BC} + \overline{CD} \tag{3.4}$$

$$\overline{DE} = \frac{M2}{\sqrt{2}\tan(\gamma)} \tag{3.5}$$

$$M2 = \frac{\overline{ABCD} \times \sqrt{2}}{\left\{\frac{1}{\tan(\delta)} + \tan(\gamma) + \frac{\left(\tan(\gamma) + 1\right)}{\sin(\gamma)}\right\}} \tag{3.6}$$

$$M1 = \frac{M2}{\sqrt{2}\cos(\gamma)} \frac{\sin(90° + \delta - \gamma)}{\sin(90° - \alpha - \delta)} \tag{3.7}$$

$$\alpha = 45° - \frac{\gamma}{2} \tag{3.8}$$

Since various combinations of these parameter values can be chosen, we considered four main aspects: (1) Focusing of the CCD camera, (2) efficient pixel usage without leaving too many pixels for the background, (3) machinability of mirror shapes and sizes, (4) available space for the system. With these in mind, the final parameter values for the imaging head were determined. A summary of all final values is given in Table 3-2.

Table 3-2. Specification Summary of conical mirrors

Parameter	$\overline{ABCD}$	$\overline{BC}$	$\overline{DE}$	$M1$	$M2$	α	β	γ
Value	800 mm	136 mm	39 mm	70 mm	80 mm	17.5°	45°	55°

3.3.3 Simplified Mock-Up Test

Before fabricating the conical mirrors, the calculated parameters were confirmed with a simplified mock-up test. A cross sectional model using flat mirrors was made and the field of view of the CCD camera was tested. As shown in the Figure 3-7a, 4-cm-wide flat mirrors are positioned in accordance with the extracted specification. A transparent acrylic stage (2 mm thickness, 4 cm width) was placed 3 mm below the central axis of the mirror considering the

animal height. A test image using a toy mouse (Figure 3-7b) was taken. The result showed that the calculated specifications lead to full coverage of the entire animal, as expected.

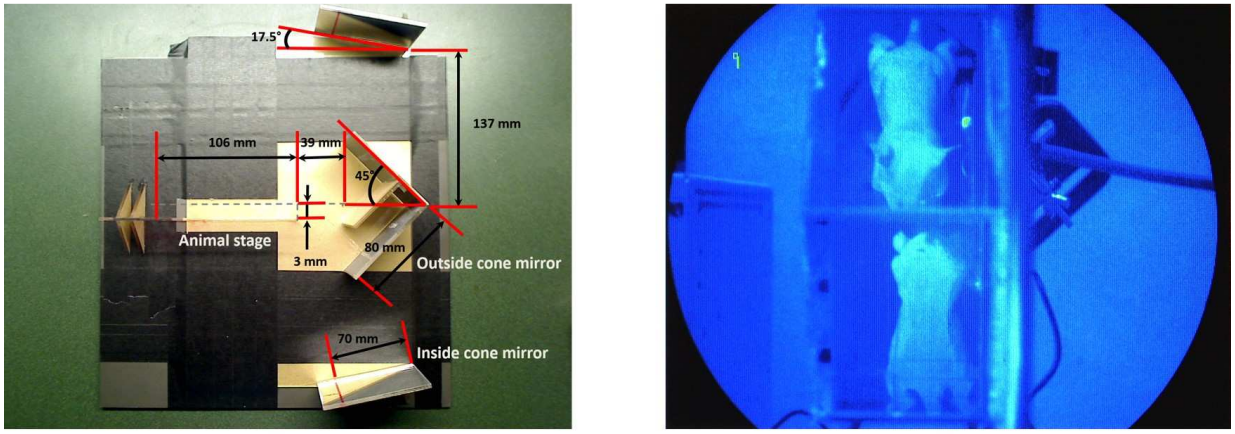

Figure 3-7. Preliminary tests of the mirror design (a) Mockup tests using flat mirrors and calculated mirror specifications and (b) an imaging coverage test with a mouse size toy

3.3.4 Simulation of Back Reflections in the Imaging Head

The second design requirement in Chapter 3 was to eliminate (or minimize) error factors, which influence the accuracy of the measurement data. Placing mirror components close to the animal to be imaged tends to create multiple reflections between the animal and mirrors. This can degrade the accuracy of the measurement raw data.

I performed Monte Carlo ray tracing simulations to quantify the effects of back reflections between the animal and highly reflective mirror surfaces in the conical mirror imaging. For this study a commercial software package LightTools (Synopsys Inc., USA) was used. The simulation conditions were: (1) A 4-cm-diameter 8-cm-long digital cylinder similar to a mouse size is placed inside the imaging head for the camera's field of view, (2) a point source that mimics light emission on the object surface moves along the object surface, (3) the surface

of the digital cylinder is a perfect absorber for detecting returned photons. By assuming the cylinder surface to be a perfect absorber, the simulations traced the emitted photons from the cylinder surface and back only in the first reflections off the mirror surfaces. Therefore, multiple reflections are not considered here. In addition to the double-conical-mirror system, I also performed simulations with a single-conical-mirror imaging head. Both types of imaging heads have the capability to gather data from 360° projections. The mirror specifications proposed by Li et al [119] were employed in the simulations, and the results for both types of imaging heads were compared.

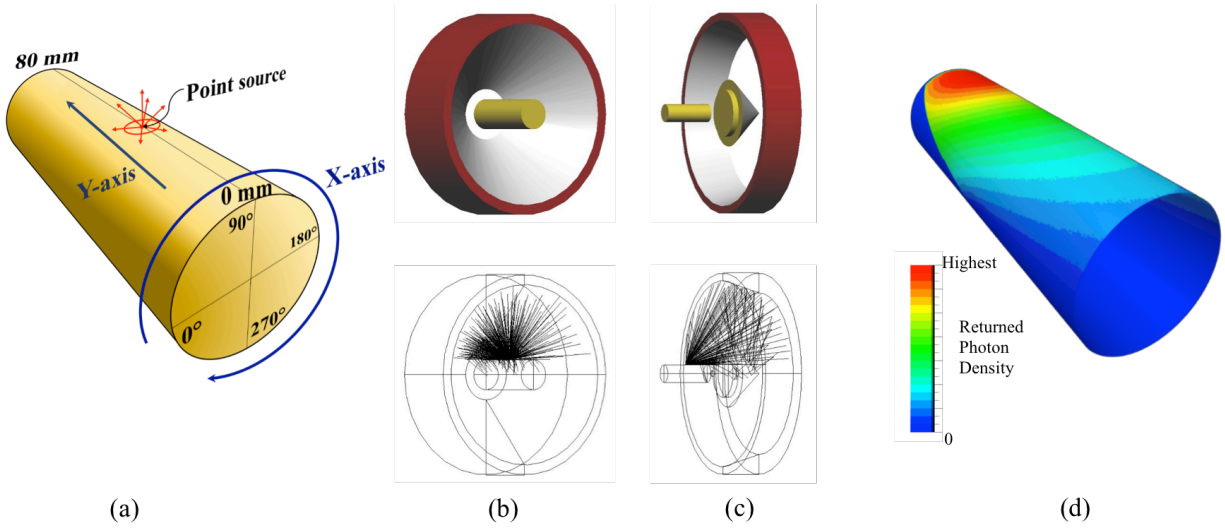

Figure 3-8. Simulation setups (a) Back reflection simulation setup, (a) a cylindrical phantom and displacement of a point source on the surface, (b) single conical mirror scheme, (c) double conical mirror scheme and (d) density distribution of returned photons on the phantom surface.

Figure 3-8 illustrates the setup for the simulations. A one watt point source positioned on the cylinder surface moves in 10 mm steps along the y-axis on the cylinder's surface from y = 10 mm to y = 70 mm (Figure 3-8a). At each step the point source emits isotropically 50,000,000 photons into the upper hemisphere. The placement of the cylinder phantom inside each imaging

head and the traces of photons are depicted in Figure 3-8b and c. The resulting density distributions of returned photons on the cylinder surfaces were calculated and displayed in Figure 3-8d.

The simulation results for each imaging head are plotted in Figure 3-9. Shown here are the fraction of photons (in % of all photons emitted from the point source) that are back reflected from the mirror surfaces of the imaging heads to the surface of the cylinder. The results show that for the single conical mirror scheme (dash line), 8.3 % to 11.7 % of emitted photons return back to the cylinder surface depending on the source position. On the other hand, for the double conical mirror scheme (solid line), back reflections are below 2% for all source positions. Even at the source position of 10 mm from the edge only 1.6% backreflections were observed. Beyond source position of 40 mm, the backreflections diminishes to zero.

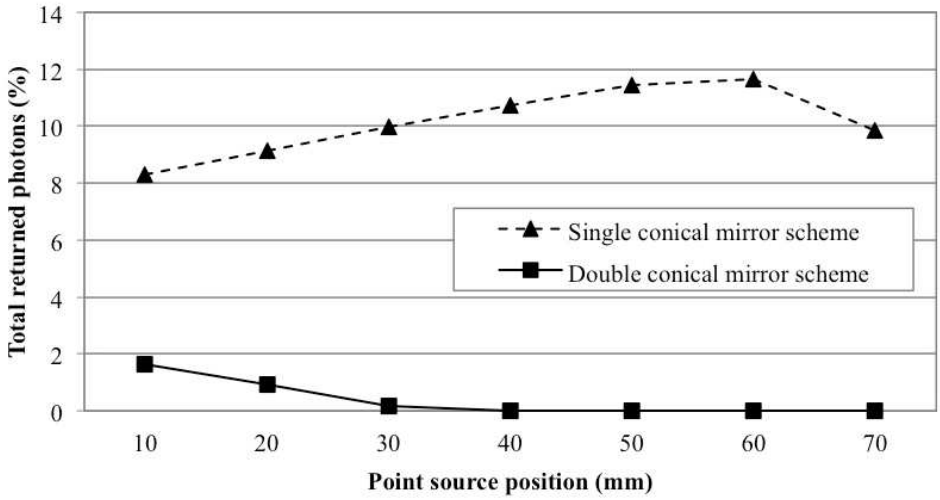

Figure 3-9. Comparison of back reflection levels as a function of the location of a point source on the cylinder surface (see Figure 3-8)

In Figure 3-10 and 3-11, the density distributions of returned photons for the single and double conical mirror schemes are shown in two dimensions by unfolding the surface layer in Figure 3-8d.

The simulation results showed that in the single conical mirror scheme (Figure 3-10), the affected area and the amount of back reflections are considerably larger than in the double conical mirror scheme (Figure 3-11). A closer inspection of Figure 3-10 reveals that as a point source (shown as a black dot) moves inside the single conical mirror (from 10 mm to 70 mm), the affected area on the cylinder surface becomes smaller. However, from Figure 3-9, the total percentage of returned photons slightly increases and peaks at 60 mm. Therefore, depending on the placement of the animal and the light sources inside the single conical mirror, the distribution and total number of back-reflected photons varies and can be converged in small surface areas. In turn this will negatively affect the accuracy of the measurement raw data.

On the other hand, Figure 3-11 shows that for the double conical mirror scheme, the affected areas on the cylinder surface disappear for the source positions beyond 40 mm. Therefore, by placing the animal more than 40 mm away from the double conical mirrors, back reflection effects can be completely avoided.

3.3.5 Fabrication and Assembly of Conical Mirrors

After the performance of the new imaging head design was confirmed, the mirrors were fabricated. Aluminum was chosen as a substrate for the mirrors because of its relatively low cost, mechanical stability, and ease of machining. Though glass materials (Pyrex, fused silica, and plate glass) and metallic materials (beryllium and invar alloys) are also known as common substrates for highly reflective mirrors, these materials are difficult to machine into the complex shapes as required here. In addition, their mechanical properties lack the stability for relatively large sized structures.

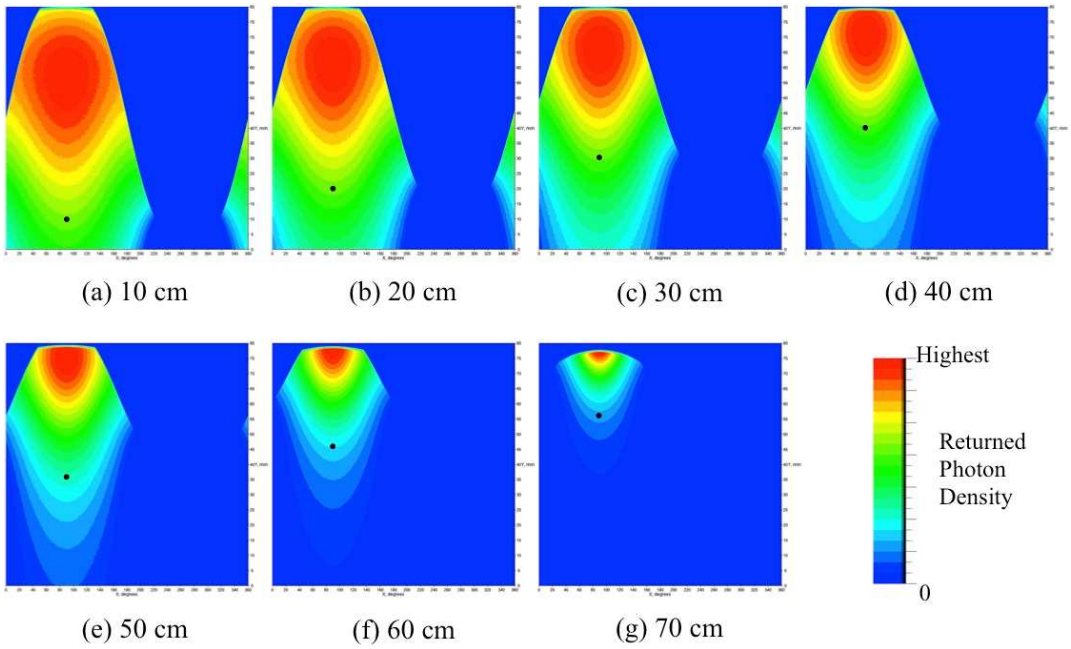

Figure 3-10. Simulation results of the single conical mirror scheme depending on a point source positions (black dot). For clear visualization, each result at different source positions is auto scaled based on the individual total returned photon results in Figure 3-9.

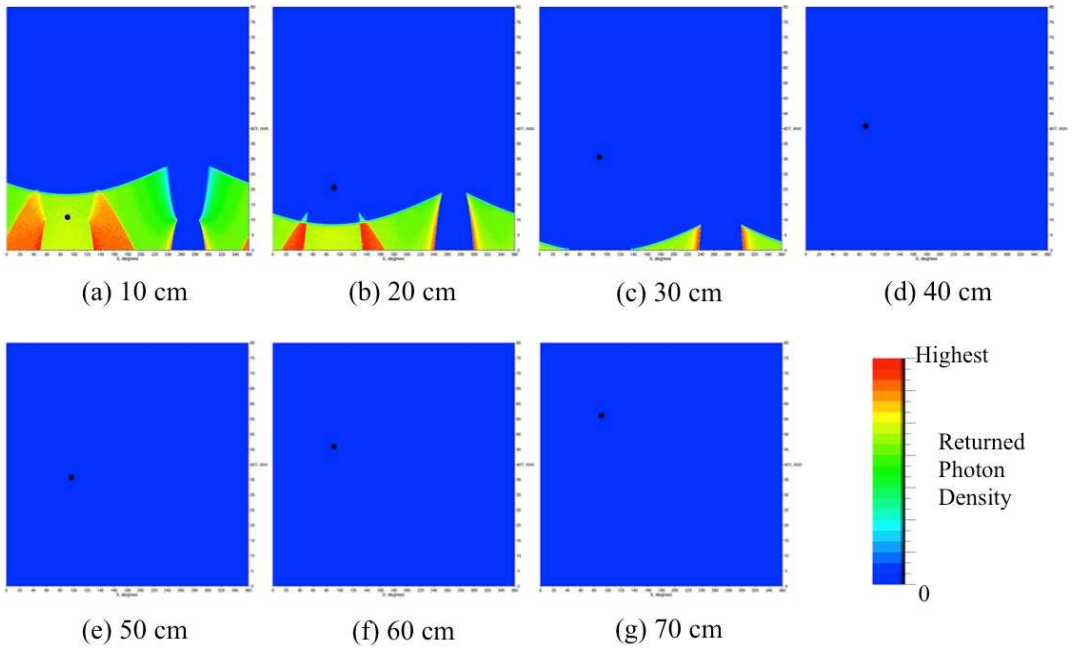

Figure 3-11. Simulation results of the double conical mirror scheme depending on a point source positions (black dot). For clear visualization, each result at different source positions is auto scaled based on the individual total returned photon results in Figure 3-9.

The aluminum mirror substrate was machined using a computer numerical control (CNC) lathe to hold tight tolerance (<±5μm) (ZeroHour Parts, MI). To achieve a higher surface reflectivity (>95%) over the visible and near-infrared wavelength range, the surfaces were polished using a diamond turning finish (70 Å rms surface roughness) and coated with protective silver that has a higher reflectivity than gold or aluminum (Rocky Mountain Instrument Co., CO and Nu-TEK Precision Optical Co., MD). This polishing method provides 80~85% reflectivity in the visible wavelength range without any additional metal coatings. The protective silver coating increases the reflectivity more than 10%. Additionally, higher damage thresholds by the coating layer make the mirror surfaces more robust and less susceptible to scratches and other damages.

The fabricated conical mirrors were assembled concentrically by using a customized aluminum mirror holder (Proto Labs, Inc., MN). The horizontal placement of an animal stage in the center of the single conical mirror head, results in shadows that appear in the images captured by the ICCD camera. These shadows are generated by both edges of the animal stage (Figure 3-12a) [119]. Since the placement of the animal stage in the double conical mirror imaging head was the same as the single conical mirror head, these shadow areas were used for the design of the mirror holder to minimize the obstructed area. Though the position and area of the shadow can vary depending on the position of light sources, the specification of a holder was decided with the assumption that a light source is positioned at the center of concentric circles.

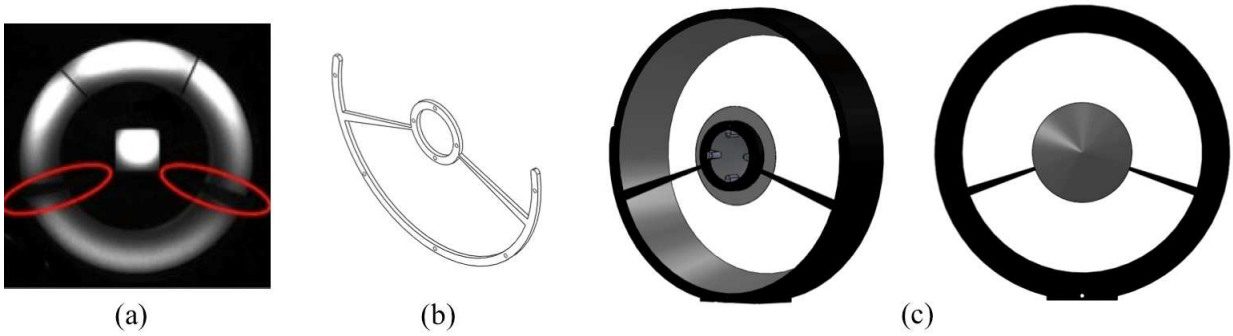

Figure 3-12. Mirror holder design: (a) Shadow areas by the edges of an animal stage in the single conical mirror scheme (red circles) [87], (b) developed mirror holder, and (c) the images of back and front sides of assembled mirrors

The outer surfaces of the conical mirrors and their holder, which do not contribute to the image formation, were painted with a highly absorptive suede coating paint (Nextel Suede-Coating 3101, Mankiewicz Gebr. & Co., Germany). This eliminates undesirable reflections by the component surfaces. Figure 3-13 shows a test image, which demonstrates that all sides of a soda can can be imaged at the same time and displayed in one image.

Figure 3-13. Test imaging using the developed imaging head with a soda can

3.4 Detection Unit

The detection unit consists of a filter wheel (AB302-T, Spectral Products, NM), optical filter sets, an optical lens (AF Nikkor 50 mm f/1.8D, Nikon, Japan), and an intensified CCD (ICCD) camera system. Each of these components is described in more detail in the following sub-chapters

3.4.1 Optical filter

The emission filter is used to filter out the excitation light leakage coming into the lens aperture of the CCD camera. First, a thin film interference bandpass filter was employed depending on the emission wavelengths. Interference filters are composed of multiple dielectric thin layers on transparent substrates. They provide maximized wavelength selectivity and transmission using sharp cut-ons and cut-offs. However, since the transmission of interference filters depends on the angle of light incidence (AOI) on the filters, the interference filter by itself could not block the excitation light perfectly in the system using the double conical mirror head. For that reason, an absorptive longpass filter is additionally used in front of the interference filter. Absorptive longpass filters are inexpensive colored glass filters and insensitive to the AOI. In the experiments, the combinations of one absorptive longpass filter and one interference filter (Chroma Technology Corp., USA) were used depending on the excitation and emission spectra of the applications.

3.4.2 Intensified CCD (ICCD) Camera System

The main component of the detection unit is the intensified CCD (ICCD) camera system (PicoStar HR 12, LaVision GmbH, Germany). It consists of a lens, an image intensifier (HRI, Kentech Instruments Ltd., England) for amplifying low intensity light, and a Charge Coupled Device (CCD) camera.

The image intensifier is comprised of a photocathode, a Micro Channel Plate (MCP), and a phosphor screen (Figure 3-14). The photocathode is coated on the inner surface of the intensifier input window. When a photon hits the photocathode, the photoelectric effect generates the emission of electrons. The spectral response and sensitivity (or Quantum Efficiency) of the camera system depends on the photocathode material. In the intensifier, a multi-alkali-antimonide S25 photocathode is used that has better wavelength properties in the visible and near infrared ranges than the S20 or the S20G. The high voltage gating pulses applied to the photocathode controls the gate width of the camera system from 300 ps to 1 ms and this gate control was used for the frequency domain measurement later. The emitted photoelectrons from the photocathode are drawn towards the MCP by a strong electric field.

The MCP is an electron multiplier using a bundle of tiny glass channels to generate secondary electrons. The inside of glass channels was coated with a resistive material. Electrons entering the glass channels collides with the inside walls and secondary electrons are released from the walls. An applied high potential gradient across the MCP determines the gain of amplification. The two dimensional electron output from the MCP is re-converted to photons by the luminescent phosphor (P43, 1% decay time: 3ms) on the output window. The generated image by reconverted photons reaches the CCD camera through the lens coupling. The specifications of the camera system are summarized in Table 3-3.

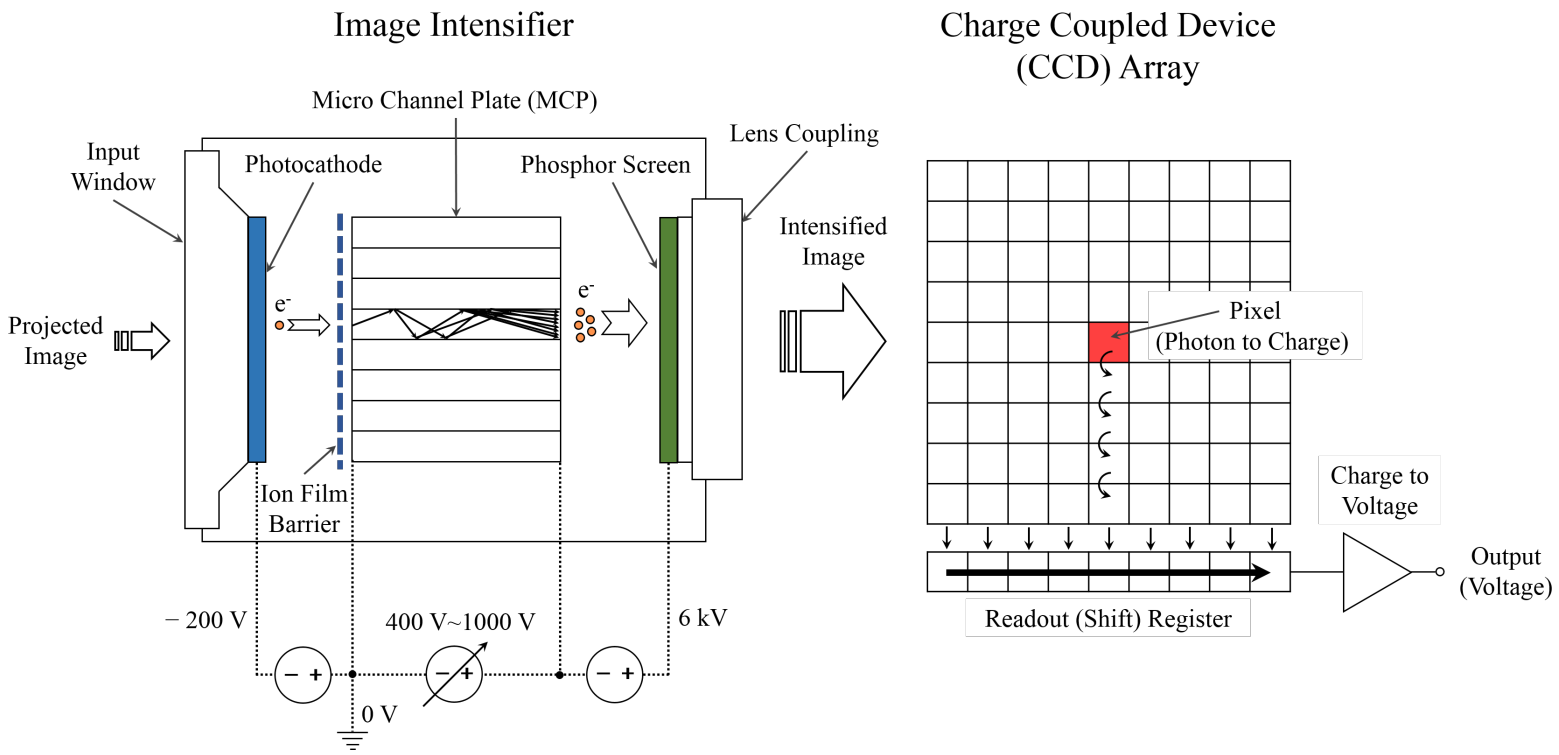

Figure 3-14. Schematic diagram of the intensified CCD (ICCD) camera system (Image intensifier + CCD array): Each channel of the MCP can be considered as a single photomultiplier tube and provides the amplification of electrons.

Table 3-3. Specifications of the intensified CCD camera system

Parameter	Value
Active Pixel Array	1370 (H) × 1040 (V) (Progressive Scan Sensor)
Pixel size	CCD: 6.5 μm × 6.5 μm Intensifier + CCD: 14.11 μm × 14.11 μm
Spatial Resolution	> 15 lp/mm
Spectral Range	350 – 900 nm
Sensitivity	> 200 counts/photoelectron at max. gain
Quantum Efficiency	65% at 550 nm
Full Well Capacity	18,000
Read Out Noise	< 5 e- (high gain) < 6 e- (low gain)
Average dark current	< 0.1 e-/pixel.sec
System Dynamic	3600:1 (71.1 dB)
CCD A/D Converter	12 bit at 16 MHz
Binning	H (1-8), V (1-32)
Exposure Time	Min. 20 ms
Frame rate	10 frames/s (full frame) 20 frames/s (2 × 2 binning)
Intensifier Type	Gen. II single stage MCP
MCP diameter	18 mm
Lens connector	Nikon-F (optional C-mount)
Cooling	2-Stage Peltier with forced air cooling
Communication	RS 232, USB, TTL-I/O

3.4.3 Frequency Domain Measurement

I designed the system to operate in so-called homodyne mode to collect frequency domain data within the range of 100 to 800 MHz [120-122]. In general, the homodyne mode technique uses a local RF oscillator to modulate a light source and to provide a demodulation reference signal to an in-phase and quadrature (I&Q) demodulator coupled with a detector. Typically, photomultiplier tubes (PMT) or avalanche photodiodes (APD) are used as detectors. After detecting the attenuated RF modulated signal, the I&Q demodulator including a phase shifter computes the amplitude attenuation and phase shift of the detected signal with respect to the given reference signal.

In the ICCD camera system, the gain-modulated image intensifier replaces the role of I&Q demodulator and acts as a multichannel RF mixer across the camera's field of view. Two synchronized signal generators of the light input unit provide a RF reference signal to the photocathode of the image intensifier. The frequency of the provided reference signal is the same or a harmonic frequency of the laser-diode modulation. Since the gating of the image intensifier is synchronized with the applied RF reference signal, only the pixel signals that are in phase with the photocathode modulation are amplified. In addition, since the decay time of the phosphor screen and the exposure time of the CCD camera are much longer than the modulation period, the incident light on the CCD camera is virtually constant over time at any given phase. By shifting the phase of the intensifier sequentially over 2π, one cycle of oscillation of every pixel can be acquired.

This information is saved as images at each phase shift step (Figure 3-15). Then, using a complex Fast Fourier transform of every pixel on the acquired images over one cycle, the average intensity, the amplitude and the phase information of the AC signal are calculated in the

range from -π to π. All of the detection process related to the camera system is controlled by the custom imaging software (DaVis by LaVision, Germany).

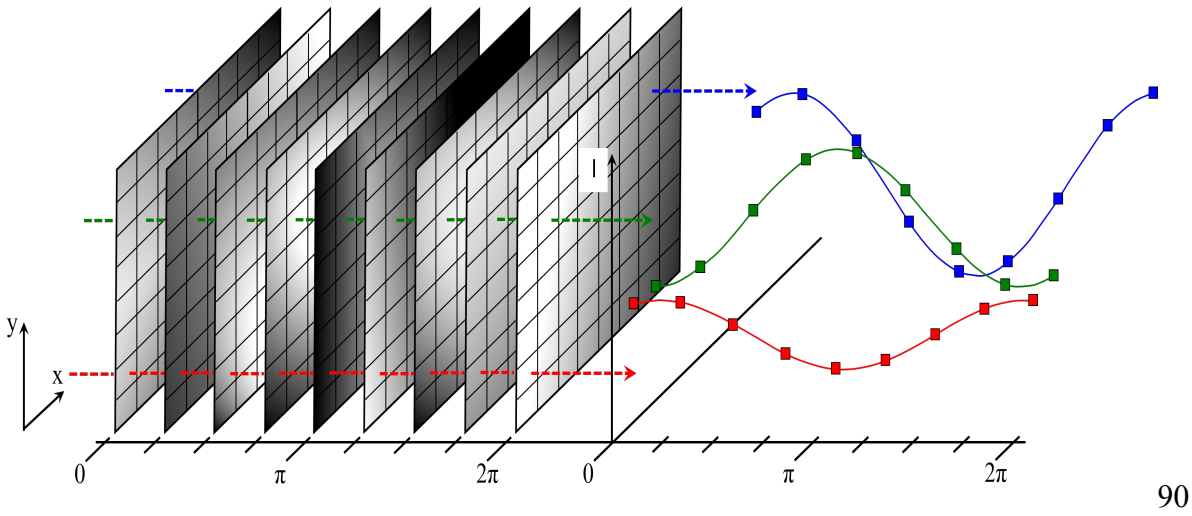

Figure 3-15. The stack of images over one cycle of oscillation: The profile of each pixel is extracted to calculate intensity, amplitude, and phase information.

3.5 Surface Scanner

In the imaging system, emitted light from the surface of the animal is directly imaged onto a CCD camera. To use this data in a suitable image reconstruction code that provides cross-sections through the animal, the animal's surface geometry needs to be extracted. To obtain this information, the surface scanner is developed and incorporated into the imaging system.

I considered various constraints and features for the scanner design: (1) First, the scanner should not obstruct the data acquisition using the developed imaging head; (2) second, the scanner should not disturb the motion of the light input unit; and (3) third, the animal to be imaged should be in its natural posture and at a fixed position through the entire imaging process. Since these constraints provide very limited space for the scanner and do not allow moving or rotating a small animal for a scan, a movable platform was incorporated in the scanner design.

The surface scanner consists of a focusable line laser, mirror backgrounds and two webcams. A green laser (LC532-5-3F, 532 nm, < 5 mW, Apinex.com Inc., Canada), which is less diffusive in tissues than a red laser, was chosen to enable the scanner software to extract boundary lines more precisely from the scan data. This line laser is attached on the linear translation stage of the light input unit. The moving laser plane intersects the animal and the background surfaces at the same time. These intersections are captured by two fixed position webcams (960×780, 15fps, Quickcam Pro 9000, Logitech, CA) and are used to triangulate three-dimensional coordinates of point clouds with known background geometries. Two 105° angled flat surfaces, which have mirror surfaces in part, are used as a background. This mirror-surfaced background reflects two opposite side views of the animal into each webcam so that total of six directional scans of a whole animal body are obtained. A scan of a whole mouse body takes about 7~10 seconds.

All components except for the line laser are fixed on the movable platform. In the scan mode, the scanner platform is positioned under the animal stage as shown in Figure 3-17d. After the scan of the animal surface is completed, the scanner can be removed from the FOV of the CCD camera (Figure 3-17c). The David Laser scanner software (DAVID Vision Systems GmbH, Germany) is used to determine the xyz coordinates of point clouds and to combine six partial surface meshes into one surface mesh. Lastly, the generation of a volume mesh and post-processing of surface and volume meshes are performed with the ICEM CFD software package (ANSYS Inc., Lebanon, USA).

In a last step, the local coordinates of the generated animal mesh are converted into the global coordinates of the imaging system based on a priori geometrical information of a reference block (35×10×15 mm). This reference block is placed on the transparent animal stage

so that it is scanned together with the animal in the scan process. The accuracy between the real (measured) object and the generated surface scan is accurate within ± 0.5 mm as shown in Figure 3-17b.

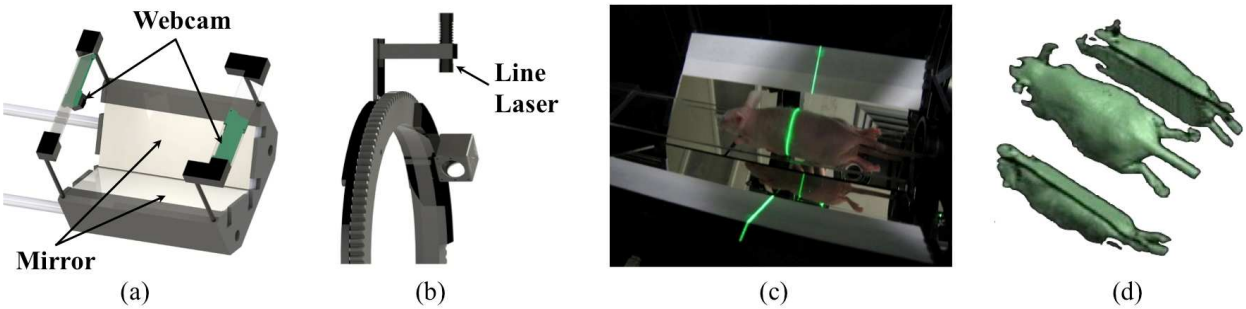

Figure 3-16 Surface boundary extraction (a) scanner components on a movable platform, (b) a line laser on the linear translation stage, (c) a photograph of a mouse scan, and (d) scan result from one webcam

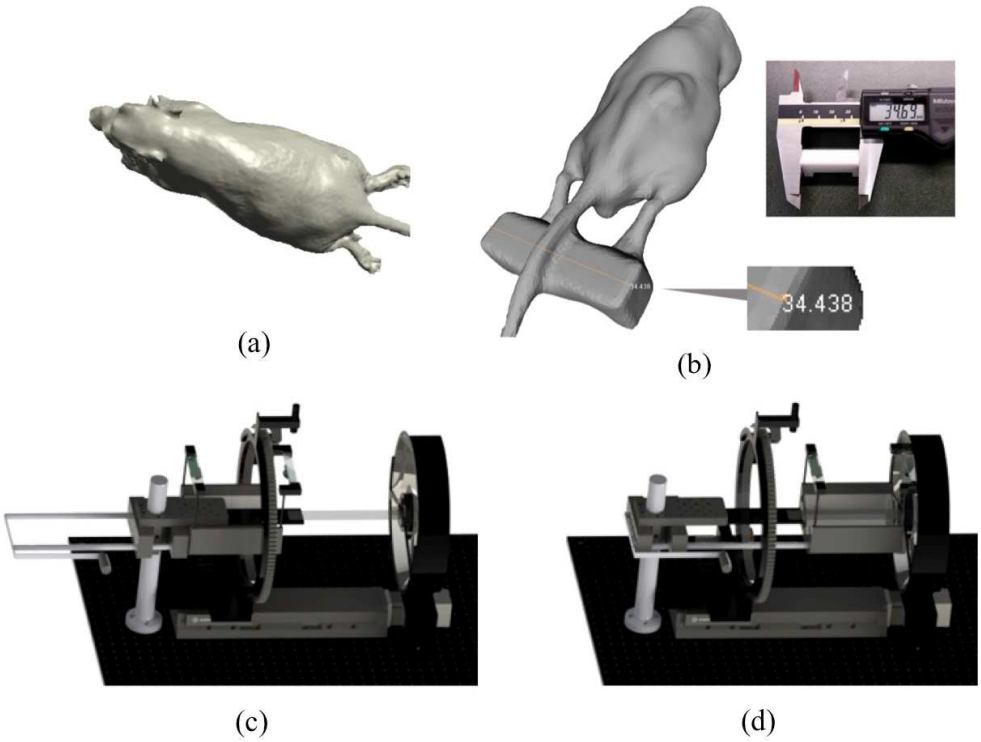

Figure 3-17. Generated surface meshes and operation modes of the scanner (a) a generated surface mesh from the scan data (see Figure 3-16d), (b) the comparison of the reference block size between the real (measured) and the generated by the scan, (c) imaging mode, and (d) scan mode of the surface scanner

3.6 System Configuration

Since the system employs a non-contact imaging geometry using conically shaped mirrors and the free space source illumination setup, the alignment of the system components is critical to reduce the errors from image distortion and inaccurate coordinate information of the laser illumination point on the animal surface. To minimize these errors, each mechanical component was designed using a computer aided design (CAD) software package, Solidworks (Dassault Systèmes SolidWorks Corp., MA). In the CAD design, the specification figures of components were considered up to two decimal places for the precise component fabrication, assembly and configuration.

All components were assembled on a solid aluminum breadboard (MB60120/M, Thorlabs, Inc., NJ) to enable accurate positioning of each component. Following the assembly on the breadboard, the height of the CCD camera, the transparent small animal stage, the surface scanner, and other related subunits were finely tuned using a labjack (M-EL120), a rod platform (M-300-P), and the fine positioner (M-32A, Newport Co., CA) of a rod platform to align with the fixed-height conical mirror pairs.

The pan and tilt of the camera was calibrated using a predefined grid pattern (5 mm, 15° interval) on a white derlin cylindrical bar (Figure 3-19a). This calibration enables accurate modeling of a three-dimensional object on two-dimensional images. The process of the calibration involves making no variation of azimuth angles and symmetrical distribution of radial lines on the cylindrical bar in the captured image (Figure 3-19b). This results in the concentric alignment of the camera, the conical mirrors, and the cylindrical object bar. The captured image of the calibration bar provides optical geometry information of the imaging setups.

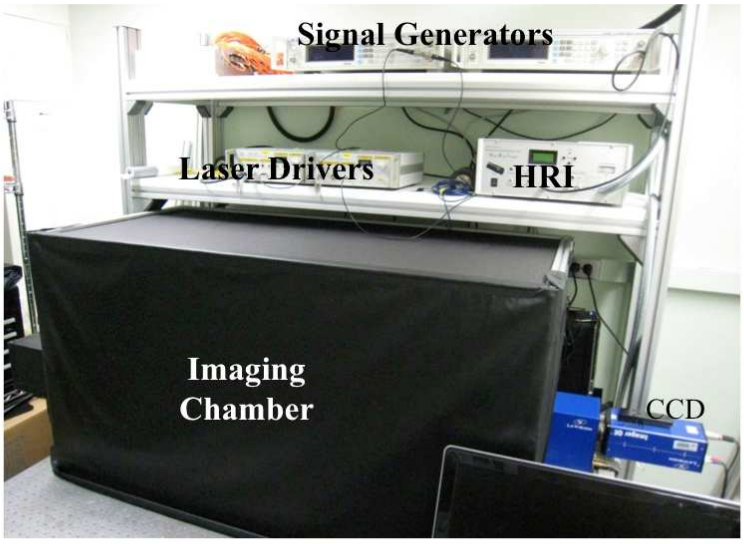

(a)

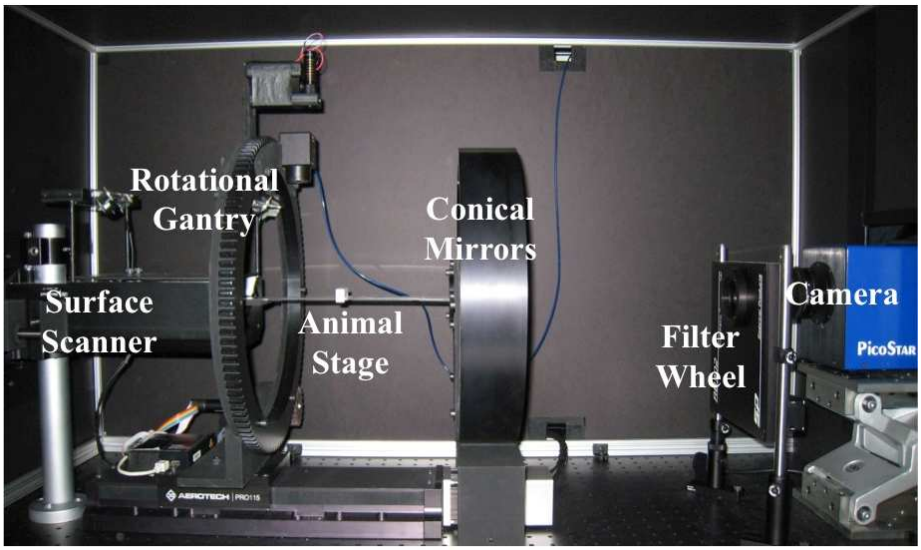

(b)

Figure 3-18. Photos of the completed FMT small animal imaging system (a) the overall appearance of the system, and (b) the inside view of the imaging chamber in (a).

Finally, the location of a source illumination spot was finely tuned based on the same cylindrical bar grid used in the camera calibration, as shown in Figure 3-19c.

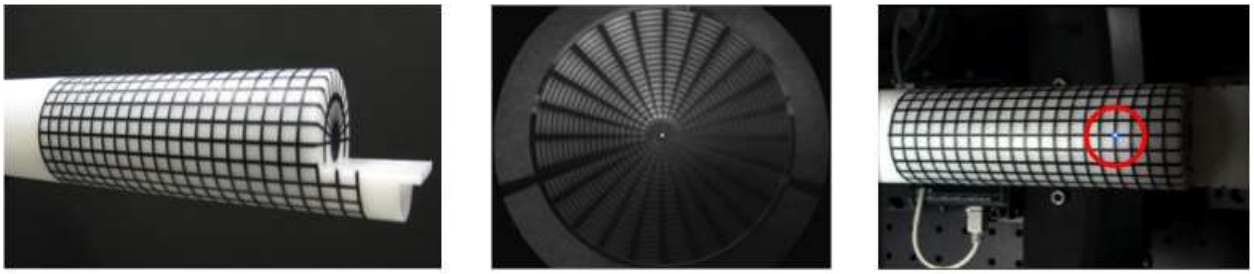

(a) (b) (c)

Figure 3-19. Alignment of system components (a) the calibration bar, (b) an image of the calibration bar obtained with the developed imaging head and the ICCD camera system, and (c) laser spot alignment with a calibration bar.

Chapter 4

IMAGE RECONSTRUCTION SCHEME FOR NON-CONTACT OPTICAL TOMOGRAPHY

4.1 Ray Transfer Operator

4.1.1 Angular-Resolved Data and Angular-Averaged Data

When light exits the tissue surface, the light intensity typically varies as a function of exit angle due to the microstructures in the tissues [123-127]. However, current tomographic imaging systems do not include the angular dependence of the intensity in tomographic image reconstructions.

As shown in Figure 4-1, fiber-based imaging systems integrate the light over all the angles within a fiber's numerical aperture and hence measure the angular-averaged data. Similarly, current camera based systems also cannot obtain the angular-resolved boundary data, due to a limited viewing angle of the camera. The angular-averaged data is typically input to a diffusion model-based reconstruction code, which does not consider the angle-dependent information in the image reconstructions. Indeed, unlike the ERT, the diffusion equation does not even contain an angular-dependent parameter. ERT-based reconstruction codes could use angular-dependent data, but because experimental data is currently unavailable potentially valuable information is lost. In a theoretical study, Gao et al recently demonstrated that using angular-resolved boundary data with the ERT based reconstruction algorithm substantially improves both the localization and the quantification of reconstruction results (Figure 4-2) [128].

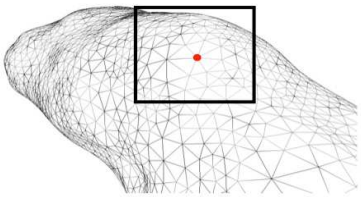

Surface boundary of an animal

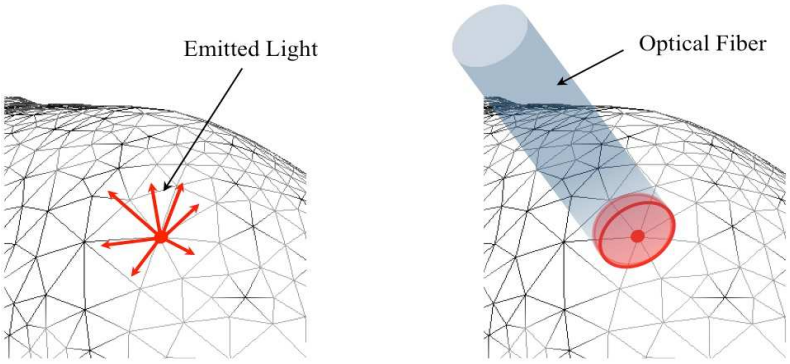

Angular-resolved boundary data Angular-averaged boundary data

Figure 4-1. Angular dependence of emitted light from the tissues (left) and the collection of emitted by using an optical fiber (right).

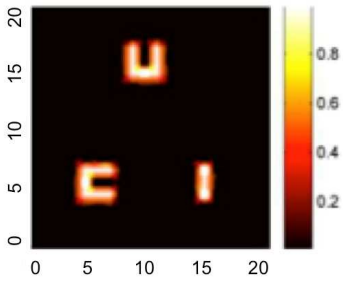

(a) True Source Position

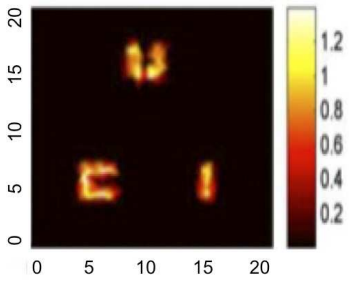

(b) Angular Resolved Data

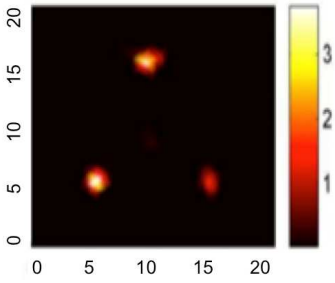

(c) Angular Averaged Data

Figure 4-2. Numerical simulation results using different data type (a) true source positions, reconstruction result using (b) angular-resolved data, and (c) angular-averaged data (from the reference [128]).

Acquiring angular-resolved data is a challenging issue in experiments as well as in imaging system development. The proposed conical-mirror scheme as described in Chapter 4 provides the capability to obtain measurements of angular-resolved-data. A conceptual illustration of this idea is given in Figure 4-3. Consider, for example, a single point positioned at the concentric axis of two conical mirrors inside the camera's field of view. The conical mirrors distribute the viewing angle of the camera to the entire 360º around a single point. As a result, the captured image in the image plane is not a point, but a ring. Therefore, within the angular coverage of the conical mirror pairs, the exit angle as well as the intensity of photons, so called angular-resolved data can be obtained. Consequently, the measurement using the conical mirror imaging head can lead to substantial improvement of the image reconstruction results.

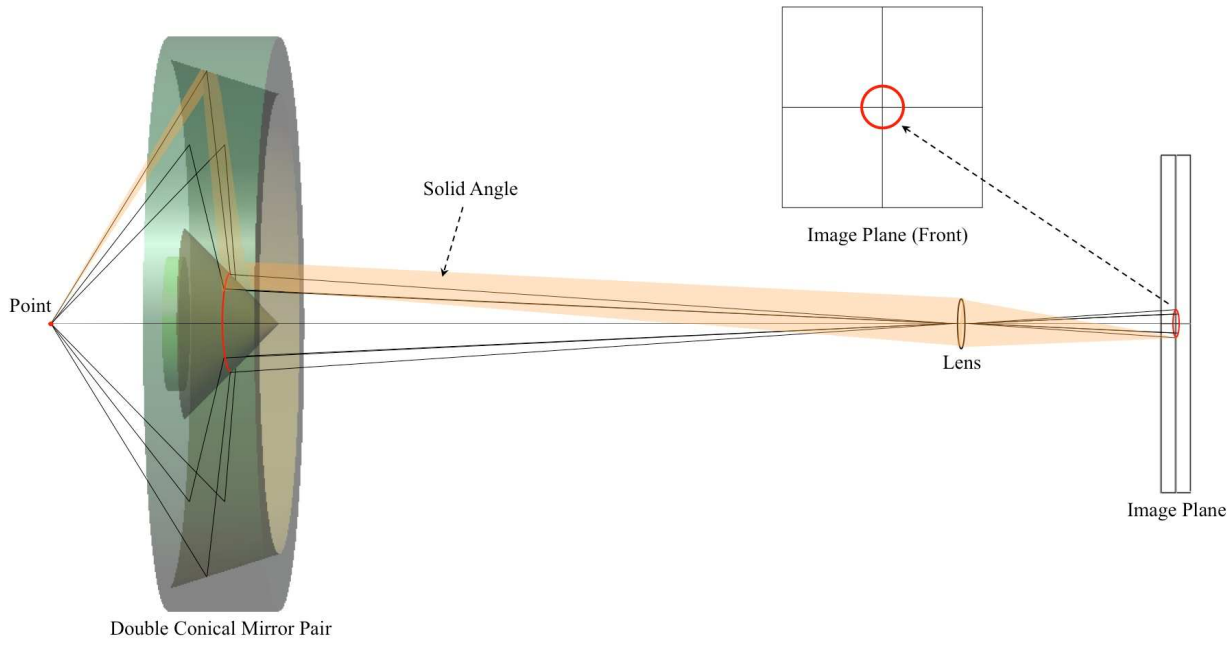

Figure 4-3. Angular-resolved measurements using the conical mirror pair. The captured image of a single point in the conical mirror pair scheme is a ring.

4.1.2 Development of Ray Transfer Operator

An ERT-based free space ray transfer operator was developed to make use of angular-resolved data in the image reconstruction. The new ray transfer operator provides a mapping of the spatial and angular distribution of the light radiance $\psi\left(\vec{r},\vec{s}\right)$ observed on the tissue surface onto pixels of the ICCD camera and goes beyond the existing operators for diffuse light or angular-averaged measurement data. The ray transfer operator was constructed by using the surface radiation theory [129]. This allows for exact treatment of light propagation in free space through the conical mirror imaging head.

Assuming an angular-dependent emitting surface as shown in Figure 4-4, the radiation power, dJ, emitted from the differential area, dA at $\vec{r}$, in the direction of $\vec{s}$ toward the lens, is given by:

$$dJ\left(\vec{r},\vec{s}\right)=\psi\left(\vec{r},\vec{s}\right)\vec{n}\cdot\vec{s}d\Omega dA \tag{4.1}$$

where $\vec{n}$ is the unit normal vector to the surface and $d\Omega$ is the differential solid angle in the direction of $\vec{s}$. The total radiation power J that is emitted from dA and captured by the lens aperture is described as:

$$J\left(\vec{r}\right)=dA\int_{\Omega_A\left(\vec{r}\right)}\psi\left(\vec{r},\vec{s}\right)\vec{n}\cdot\vec{s}d\Omega \tag{4.2}$$

where $\Omega_A\left(\vec{r}\right)$ is the solid angle subtended by the projected area of dA on the lens aperture.

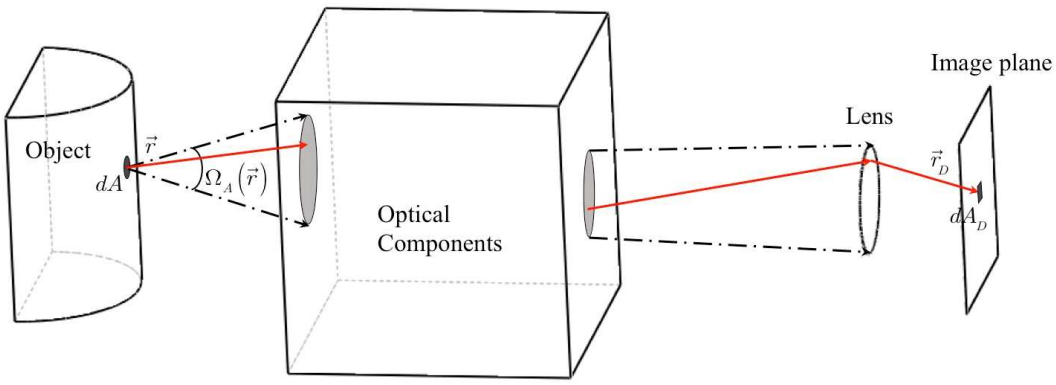

Figure 4-4. Light propagation from an object's surface to the aperture of the camera through optical components

Assuming that all the photons within $\Omega_A(\vec{r})$ passing through the lens aperture are deposited on the image plane of a camera without any loss, the total radiant power $J(\vec{r})$ passing through the lens aperture is equivalent to the total radiant flux $z(\vec{r}_D)$ on the differential area dA_D in the image plane, given by:

$$J(\vec{r}) = dA \int_{\Omega_A(\vec{r})} \psi(\vec{r},\vec{s})\vec{n}\cdot\vec{s}d\Omega = dA_D z(\vec{r}_D) \tag{4.3}$$

$z(\vec{r}_D)$ is the measurable quantity being compared to the prediction during the reconstruction process. Finally, $z(\vec{r}_D)$ can be expressed as a function of angular-dependent radiance $\psi(\vec{r},\vec{s})$:

$$z(\vec{r}_D) = \frac{\vec{n}dA}{dA_D}\cdot \int_{\Omega_A(\vec{r})} \psi(\vec{r},\vec{s})\vec{s}d\Omega = Q(\vec{r},\vec{s})\psi(\vec{r},\vec{s}) \tag{4.4}$$

The ray transfer operator $Q\left(\vec{r},\vec{s}\right)$ is constructed by using a ray tracing method like Monte Carlo method and depends on the direction $\vec{s}$, the position $\vec{r}$, the solid angle $d\Omega$, and the area ratio dA/dA_D. Therefore, $z\left(\vec{r}_D\right)$ provides the data with angular-dependent information.

4.2 ERT-based Image Reconstruction Algorithm

A three-dimensional distribution of fluorescent sources in tissue is achieved by using a partial differential equation (PDE)-constrained optimization method that is based on the frequency domain equation of radiative transfer.

4.2.1 Forward Model for Light Propagation

The generation and propagation of fluorescent light in biological tissue can be accurately modeled by two coupled frequency-dependent equations of radiative transfer [130, 131], given by

$$\left[(\nabla\cdot\Omega)+\mu_a^x+\mu_s^x+\mu_a^{x\to m}+\frac{i\varpi}{c}\right]\psi^x(\mathbf{r},\Omega,\varpi)=\int_{4\pi}p(\Omega',\Omega)\psi^x(\mathbf{r},\Omega',\varpi)d\Omega' \tag{4.5}$$

$$\begin{aligned}\left[(\nabla\cdot\Omega)+\mu_a^m+\mu_s^m+\frac{i\varpi}{c}\right]&\psi^m(\mathbf{r},\Omega,\varpi)\\ &=\int_{4\pi}p(\Omega',\Omega)\psi^m(\mathbf{r},\Omega',\varpi)d\Omega'+\frac{1}{4\pi}\frac{\eta\mu_a^{x\to m}\phi(\mathbf{r},\varpi)}{(1-\varpi\tau(\mathbf{r}))}.\end{aligned} \tag{4.6}$$

Equations (4.5) and (4.6) represent the propagation of excitation light from the external light source and the emission light propagation from the fluorescent source inside the tissues, respectively. The superscripts x and m in equations denote the excitation and emission respectively. The parameters μ_a and μ_s are the absorption and scattering coefficients in units of cm^{-1} respectively. The absorption coefficient of the fluorescent source is denoted by $\mu_a^{x\to m}$. The source modulation frequency is ϖ and c is the speed of light inside the tissue. The light radiance $\psi(\mathbf{r},\Omega,\varpi)$ is represented in units of $W\cdot cm^{-2}\cdot sr^{-1}$; η denotes the quantum yield of the fluorescent source; $\phi(\mathbf{r},\varpi)$ is the excitation fluence in units of $W\cdot cm^{-2}$ defined by $\phi(\mathbf{r},\varpi)=\int_{4\pi}\psi^x d\Omega$; $\tau(\mathbf{r})$ is the local lifetime of the fluorescent source; $p(\Omega',\Omega)$ is the commonly used Henyey-Greenstein phase function given by

$$p=\frac{1-g^2}{\left(1+g^2-2g\cos\theta\right)^{\frac{3}{2}}}. \tag{4.7}$$

The boundary conditions for the two coupled equations are given by (4.8) and (4.9):

$$\psi_b^x\Big|_{\vec{n}_b\cdot\Omega<0}=\psi^{x0}\Big|_{\vec{n}_b\cdot\Omega<0}+R(\Omega',\Omega)\cdot\psi^x\Big|_{\vec{n}_b\cdot\Omega'>0} \tag{4.8}$$

$$\psi_b^m\Big|_{\vec{n}_b\cdot\Omega<0}=R(\Omega',\Omega)\cdot\psi^m\Big|_{\vec{n}_b\cdot\Omega'>0}. \tag{4.9}$$

In summary, the excitation light is absorbed in part by the fluorescent source inside the tissues and the excited fluorescent source re-emits radiation typically at longer wavelength with strength

being proportional to the local fluorophore absorption, the lifetime of the fluorescent source, and the quantum yield.

For discretization of the light propagation model, an unstructured node-centered finite-volume discrete-ordinates method is employed to make use of the beneficial properties of finite-element and finite-volume methods such as the conservation properties of the finite volume formulation and the geometric flexibility of the finite-element approach [129, 132]. The discretized forms of the two ERTs (4.10 and 4.11) are obtained as

$$\left[(\nabla\cdot\Omega)+\mu_a^x+\mu_s^x+\mu_a^{x\to m}+\frac{i\varpi}{c}\right]\psi^x(\mathbf{r},\Omega,\varpi)=\int_{4\pi}p(\Omega',\Omega)\psi^x(\mathbf{r},\Omega',\varpi)\,d\Omega', \tag{4.10}$$

$$\begin{aligned}\sum_{j=1}^{N_{surf}}(\vec{n}_j\cdot\Omega^l)\psi_j^{m,l}dA_j+(\mu_a^m+\mu_s^m+\frac{i\omega}{c})\psi_N^{m,l}\\ =\int_{4\pi}p(\Omega',\Omega)\psi^m(\mathbf{r},\Omega',\varpi)\,d\Omega'+\frac{1}{4\pi}\frac{\eta\mu_a^{x\to m}\phi(\mathbf{r},\varpi)}{(1-\varpi\tau(\mathbf{r}))}\end{aligned} \tag{4.11}$$

where N_{surf} is the number of surfaces surrounding the node $N(=1,...,N_t)$ and N_Ω is the discrete ordinates. The vector $\vec{n}_j$ denotes the surface normal vector and ψ_j^l represents the radiance defined on j^{th} surface in the direction l. These surface intensities are related to the nodal intensities ψ_N^l by the second-order spatial differencing scheme [129]. Each ERT involving N_t (nodes) coupled into N_Ω (directions) leads to the total $N_t\cdot N_\Omega$ unknowns. A matrix-based iterative linear solver is employed here, which enables updating all the radiation intensities ψ_N^l simultaneously, thus leading to fast convergence compared with source iteration-based techniques.

Two linear systems of algebraic equations are finally obtained as

$$A^x \psi^x = b^x \tag{4.12a}$$

$$A^m \psi^m = b^m \tag{4.12b}$$

Each line denoted by $i(i = 1,\ldots, N_t N_\Omega)$ of the matrix A contains the coefficients of the discretized forms (4-10) and (4-11), established at the node number N and the direction l. The excitation light source and the fluorescent source term come into the term b^x and b^m respectively after the discretization on the boundary node N_b and the internal node N .

$$b_{N_b}^{x,l} = -\sum_j \left[1 - \max(n_j \cdot \Omega^l / \left| n_j \cdot \Omega^l \right|, 0)\right](n_j \cdot \Omega^l) A_j \psi_{N_b}^{0,l} \tag{4.13a}$$

$$b_N^{m,l} = \frac{1}{4\pi} \frac{\eta \mu_a^{x \to m} \phi(\mathbf{r}, \varpi)}{(1 - \varpi \tau(\mathbf{r}))} \Delta V_N \tag{4.13b}$$

where $\psi_{N_b}^{0,l}$ is the external light source function on the boundary node N_b in direction l.

The resulting frequency-domain system of complex valued algebraic linear equations is solved using a complex version of the generalized minimum residual (GMRES) solver [133, 134]. The solutions of two equations provide the predictions of the excitation radiance $\psi_j^{x,l}$ and transmitted emission radiance $\psi_j^{m,l}$ on the boundary surface. These two equations are used as the

constraints within the PDE-constrained optimization method that solves for the spatial distribution of the fluorescent sources inside the tissue.

4.2.2 Inverse Problem

4.2.2.1 PDE-constrained Optimization

The optical tomographic problem can be formulated in more general terms as

$$\begin{aligned} &\min \quad f(x,u) \\ &\text{s.t.} \quad c(x,u)=0 \end{aligned} \tag{4.14}$$

where $x \in R^n$ and $u \in Z^m$ are the vectors of the inverse and forward variables respectively. The function $f(x;u)$ is the objective function that quantifies the difference between measured and predicted light intensities on the medium surface and $c(x;u)=0$ is a discretized version of coupled excitation and emission equations. Traditional methods for solving (4.14) is to treat the forward variable u as a dependent variable of the inverse variable x, i.e., $u=\tilde{c}(x)$, which reformulates the original problem (4.14) into the following:

$$\min \quad \tilde{f}(x)=f(x,\tilde{c}(x)) \tag{4.15}$$

which is referred to as 'unconstrained' since the equality constraint, $c(x,u)=0$ is eliminated in (4.15). Thus, the complete solution of forward model, $u=\tilde{c}(x)$ should be obtained at each optimization iteration for the evaluation of $\tilde{f}(x)$, which leads to a computationally very

demanding process in the associated optimization procedure. Nevertheless, this approach has been widely used due to easiness of implementation, which includes existing codes such as the conjugate gradient (CG) approach [135], the quasi-Newton (QN) approach [136-138], and the Jacobian approach [139-145].

On the other hand, the "PDE-constrained" optimization approach treats x and u independently, which solves for the variables x and u simultaneously at once. Typically, an extended objective function called "Lagrangian" is introduced as follows:

$$L(x,u;\lambda) = f + \lambda^T c \tag{4.16}$$

where $\lambda \in Z^m$ is the vector of Lagrange multipliers. The solutions of both forward and inverse problems can be simultaneously obtained at points satisfying the first-order Karush-Khun-Tucker (KKT) conditions [146-148] where the gradient L vanishes with respect to λ, u and x respectively. This type of PDE-constrained approach allows for using the inexact solution of the forward problem to solve for the inverse problem solution, which leads to a significant time saving in the total image reconstruction time.

4.2.2.2 Inverse Problem of the Fluorescence Molecular Tomography

The fluorescence tomographic problem is to find a vector of unknown sources $x = (\mu_a^{x\to m}, \tau, \eta)$ inside the medium, assuming that all other intrinsic optical properties inside medium such as the absorption coefficient μ_a and the scattering coefficient μ_s are already known at the excitation and emission wavelengths, such that:

$$\begin{aligned} &\min \quad J(\psi^m) = \frac{1}{2}\sum_{s,d}\left|\mathrm{Q}_d\psi_s^m - z_{s,d}\right|^2 \\ &\text{subject to} \\ &C_s^x = A^x\psi_s^x - b_s^x = 0; s = 1,...,N_s \\ &C_s^m = A^m\psi_s^m - b_s^m = 0; s = 1,...,N_s \end{aligned} \tag{4.17}$$

where $J(\psi_s^m)$ is the objective function that quantifies the difference between measurements and predictions of emitted light from the tissue surface. C^x and C^m are the discretized radiative transfer equations for the excitation and emission equations. By assuming homogeneous τ and η inside the medium, this work focuses on reconstructing the spatial distribution of the fluorophores absorption $\mu_a^{x\to m}$ (hereafter denoted as μ) is to be reconstructed. The above inverse problem (4.17) can be restated using a Lagrangian function as

$$L(\mu;\psi^x,\psi^m;\lambda^x,\lambda^m) = \frac{1}{2}\left|\mathrm{Q}\,\psi^m - z\right|^2 + \lambda^{xT}\left(A^x\psi^x - b^x\right) + \lambda^{mT}\left(A^m\psi^m - b^m\right). \tag{4.18}$$

The solutions of the forward and inverse problems can be simultaneously obtained at the points where the following first derivatives of the Lagrangian function (4.18) with respect to each variable become zero.

$$L_\mu \equiv \frac{\partial L}{\partial \mu} = (\psi^{xT}A^{xT})_\mu\lambda^x - (b^{mT})_\mu\lambda^m = 0 \tag{4.19a}$$

$$L_{\psi^x} \equiv \frac{\partial L}{\partial \psi^x} = A^{xT}\lambda^x - (b^{mT})_{\psi^x}\lambda^m = 0 \tag{4.19b}$$

$$L_{\psi^m} \equiv \frac{\partial L}{\partial \psi^m} = Q^T(Q\psi^m - z) + A^{mT}\lambda^m = 0 \tag{4.19c}$$

$$L_{\lambda^x} \equiv \frac{\partial L}{\partial \lambda^x} = A^x\psi^x - b^x = 0 \tag{4.19d}$$

$$L_{\lambda^m} \equiv \frac{\partial L}{\partial \lambda^m} = A^m\psi^m - b^m = 0 \tag{4.19e}$$

where the first equation L_μ is the sensitivity equation with respect to the inverse variable μ, and the second and third equation can be viewed as the adjoint equations for λ^x and λ^m. The last two equations are the two forward equations. Then the KKT system given by (4.19) is solved by using Newton's method as

$$\begin{bmatrix} W & A^T \\ A & 0 \end{bmatrix}\begin{bmatrix} \Delta p \\ \Delta\lambda \end{bmatrix} = -\begin{bmatrix} L_p \\ L_\lambda \end{bmatrix} \tag{4.20}$$

where the block matrix W and A denote the Hessian matrix of the Lagrangian function L and the Jacobin matrix of constraints C^x and C^m with respect to each of unknowns $p = (\mu, \psi^x, \psi^m)$. The vector Δp represents $[\Delta\mu, \Delta\psi^x, \Delta\psi^m]^T$ and $\Delta\lambda$ denotes $[\Delta\lambda^x, \Delta\lambda^m]^T$. The above algebraic system (4.20) is then solved efficiently by using the reduced Hessian Sequential Quadratic Programming (SQP) scheme.

4.2.2.3 Reduced Hessian Sequential Quadratic Programming

The reduced Hessian SQP method is a method that enables solving nonlinear constrained optimization problems with relatively low cost and fast convergence [149]. The rSQP method solves the KKT system (4.20) through finding the minimum of a quadratic approximation of the Lagrangian function L subject to the linearized constraints C^x and C^m. Thus, the KKT system (4.20) is equivalent to the following quadratic programming problem.

$$\begin{aligned} &\min \quad \Delta p^T g + \frac{1}{2}\Delta p^T W \Delta p \\ &\text{subject to} \\ &A\Delta p + C = 0 \end{aligned} \tag{4.21}$$

where $g = \nabla J = \left[g_\mu , g_{\psi^x} , g_{\psi^m} \right]$ represents the gradients of the objective function f with respect to each of unknowns $(\mu \ , \psi^x , \psi^m)$ and W is the full Hessian (or approximations) of the Lagrangian function. The linearized constraints in (4.21) correspond to the last block of the KKT system (4.20) as:

$$L_{\mu\lambda^x}\Delta\mu + L_{\psi^x\lambda^x}\Delta\psi^x + L_{\psi^m\lambda^x}\Delta\psi^m = -L_{\lambda^x} \tag{4.22a}$$

$$L_{\mu\lambda^m}\Delta\mu + L_{\psi^x\lambda^m}\Delta\psi^x + L_{\psi^m\lambda^m}\Delta\psi^m = -L_{\lambda^m} \tag{4.22b}$$

where

$$L_{\mu\lambda^x} = (A^x\psi^x)_\mu,\ L_{\psi^x\lambda^x} = A^x,\ L_{\psi^m\lambda^x} = 0 \tag{4.23a}$$

$$L_{\mu\lambda^m} = (-b^m)_\mu,\ L_{\psi^x\lambda^m} = (-b^m)_{\psi^x},\ L_{\psi^m\lambda^m} = A^m \tag{4.23b}$$

The linearized constraints in (4.22) can be rewritten as

$$A^x\Delta\psi^x = -\left\{C^x + (A^x\psi^x)_\mu\Delta\mu\right\} \tag{4.24a}$$

$$A^m\Delta\psi^m = -\left\{C^m - (b^m)_\mu\Delta\mu - (b^m)_{\psi^x}\Delta\psi^x\right\} \tag{4.24b}$$

However, the full Hessian of the Lagrangian function is often difficult to obtain and its approximation by the updating scheme tends to create large dense matrix $(n+m)\times(n+m)$. These difficulties are overcome by dropping certain non-critical second-order terms of the full Hessian matrix. Here the standard reduced Hessian SQP method based on the separation of variable is employed and described as follows.

Because A^x and A^m are invertible, the vector Δp can be decomposed into two parts as:

$$\Delta p = Z + Y\Delta\mu \tag{4.25}$$

where

$$Z = \begin{bmatrix} 0 \\ -(A^x)^{-1}C^x \\ -(A^m)^{-1}\{C^m + (b^m)_{\psi^x}(A^x)^{-1}C^x\} \end{bmatrix} \tag{4.26}$$

and

$$Y = \begin{bmatrix} I \\ -(A^x)^{-1}(A^x\psi^x)_\mu \\ (A^m)^{-1}\left\{(b^m)_\mu - (b^m)_{\psi^x}(A^x)^{-1}(A^x\psi^x)_\mu\right\} \end{bmatrix} \tag{4.27}$$

Since the choice of Z and Y is a challenging problem in practical implementation of the reduced SQP, the popular choice for Z and Y by many authors is used in this study [150-153].

By substituting (4.25) into (4.21) and differentiating the resulting expression with respect to $\Delta\mu$, and using the identity $Y^T A^T = 0$, the reduced Hessian is given by

$$H_r \Delta\mu = -(g_r + d) \tag{4.28}$$

where $H_r = Y^T W Y$ denotes the reduced Hessian and $g_r = Y^T g$ represents the reduced gradient. $d = Y^T W Z$ is called the cross-term. Accordingly the reduced SQP method needs to maintain and update only a small $(n \times n)$ matrix at each iteration of optimization; therefore it requires much less memory than the full SQP one. From (4.28) and (4.25), the inverse solution $\Delta\mu$ and the forward solution $\Delta\psi$ can be obtained as

$$\Delta\mu = -(H_r)^{-1}(g_r + d_r) \tag{4.29}$$

$$\Delta\psi = \begin{bmatrix} \Delta\psi^x \\ \Delta\psi^m \end{bmatrix} = Z - Y(H_r)^{-1}(g_r + d_r) \tag{4.30}$$

At the new iterate, the Largrangian multiplier vectors are updated from

$$\lambda^m = \left[A^{mT}\right]^{-1} Q^T (Q\psi - z) \tag{4.31}$$

$$\lambda^x = \left[A^{xT}\right]^{-1} (b^{mT})_{\psi^x} \lambda^m. \tag{4.32}$$

Then the updated Largrangian multiplier vectors are applied to the reduced gradient rewritten as:

$$\begin{aligned} g_r &= Y^T g \\ &= (b^{mT})_\mu \lambda^m - (\psi^{xT} A^{xT})_\mu \lambda^x. \end{aligned} \tag{4.33}$$

The direct computation of the reduced Hessian H_r and its matrix inversion $(H_r)^{-1}$ are avoided here by using a direct approximation to the matrix-vector product of $(H_r^k)^{-1} g_r^k$ through the limited-memory Broyden-Fletcher-Goldfarb-Shanno (BFGS) updating algorithm [146, 148]. This approach enables the proposed rSQP scheme to be applied to large-scale optimization problems. It should also be noted that the cross-term vector $d_r^k = Y^{kT} W^k Z^k$ is ignored as in other works [149-152].

The global convergence of the rSQP scheme is ensured by line search on the real-valued l_1 merit function (4.34), which is chosen due to its simplicity and low computational cost.

$$\varphi_\eta(\mu,\psi^x,\psi^m) = J(\psi^m) + \eta\left\|C\right\|_1 \tag{4.34}$$

The directional derivative of $D\varphi_n\left(\mu,\psi^x,\psi^m\right)$ along the descent direction of Δp is presented as

$$D\varphi_\eta = g^{kT}\Delta p - \eta\left\|C\right\|_1. \tag{4.35}$$

Thus, the decent property $D\varphi_\eta(\mu,\psi^x,\psi^m) < 0$ can be maintained by choosing [154]

$$\eta > g^T\Delta p / \left\|C\right\|_1. \tag{4.36}$$

At each iteration given by $p^{k+1} = p^k + \alpha^k\Delta p$, the merit function (4.34) is successively monitored to ensure the global convergence while line search provides a step length for the sufficient decrease in the merit function as [153].

$$\varphi_{\eta^k}(p^k + \alpha^k\Delta p^k) \le \varphi_{\eta^k}(p^k) + 0.01\alpha_k D_{\eta^k}(p^k;\Delta p^k). \tag{4.37}$$

4.2.3 Computational Implementation of the rSQP Scheme

The reduced Hessian SQP algorithm can be summarized into the following structure.

Algorithm

Reduced Hessian Sequential Quadratic Programming (rSQP) scheme
for reconstructing the spatial distribution of the absorption coefficient μ of the fluorescent source

1: Set $k=0$ and initialize $\mu^0, \psi^{x,0}, \psi^{m,0}$ and $H_r^0 = I$

2: Solve $A^{mT}\lambda^{m,0} = -Q^T(Q\psi^{m,0} - z)$ for λ^{m0}, and solve $A^{xT}\lambda^{x,0} = (-b^{mT})_{\psi^{x0}}\lambda^{m,0}$ for λ^{x0}

3: Compute $g_r^0 = (b^{mT})_\mu \lambda^{m,0} - (\psi^{xT}A^{xT})_\mu \lambda^{x,0}$

4: Check the stopping criteria: if satisfied, stop

5: Solve $H_r^k \Delta\mu^k = -g_r^k$ for $\Delta\mu$ via a limited-memory BFGS updating formula.

6: Solve the two QP problems for $\Delta\psi^{xk}$ and $\Delta\psi^{mk}$

$$A^x \Delta\psi^{x,k} = -\left\{C^x + (A^x\psi^x)_\mu \Delta\mu^k\right\}$$
$$A^m \Delta\psi^{m,k} = -\left\{C^m - (b^m)_\mu \Delta\mu^k - (b^m)_{\psi^x}\Delta\psi^x\right\}$$

7: Set $\alpha_k = 1$ and check if it ensures the sufficient decrease in the merit function

$$\varphi_{\eta_k}(p^k + \alpha^k \Delta p^k) \le \varphi_{\eta_k}(p^k) + 0.01\alpha_k D_{\eta_k}(p^k; \Delta p^k)$$

where $\varphi_\eta(\mu, \psi^x, \psi^m) = J(\psi^m) + \eta\left\|C\right\|_1$

8: If the sufficient decreasing condition is satisfied by the searched step length, then set

$$\mu^{k+1} = \mu^k + \alpha^k \Delta\mu^k$$
$$\psi^{x,k+1} = \psi^{x,k} + \alpha^k \Delta\psi^{x,k}$$
$$\psi^{m,k+1} = \psi^{m,k} + \alpha^k \Delta\psi^{m,k}$$

; otherwise,

$$\alpha^k = \max\left\{ \frac{-0.5 D\varphi_{\eta_k}(\alpha^k)^2}{\varphi_{\eta_k}(p^k + \alpha^k \Delta p^k) - \varphi_{\eta_k}(p^k) - \alpha^k D\varphi_{\eta_k}}, 0.01 \right\}$$

9: Evaluate C^{k+1}, g^{k+1} and A^{k+1}, and compute Y^{k+1} and Z^{k+1}.

10: Solve for $\lambda^{x,k+1}$ and $\lambda^{m,k+1}$ with a GMRES solver

$$\lambda^{m,k+1} = \left[A^{mT}\right]^{-1} Q^T (Q\psi^m - z)$$
$$\lambda^{x,k+1} = \left[A^{xT}\right]^{-1} (b^{mT})_{\psi^x} \lambda^{m,k+1}$$

and update the merit function parameter h_k by

$$\eta_{k+1} = 1.001 + \left\|\lambda_{k+1}\right\|_\infty$$

11: Evaluate $g_r^{k+1} = (b^{mT})_\mu \lambda^{m,k+1} - (\psi^{xT} A^{xT})_\mu \lambda^{x,k+1}$

12: Get $y^k = Y^{T,k+} g^{k+} - Y^{T,k} g^k$ and $s^k = \mu^{k+1} - \mu^k$.

13: Set $k = k+1$ and return to Step 4 to check the convergence.

As mentioned earlier, the rSQP algorithm makes use of the incomplete solutions of the two forward equations during the reconstruction process. Thus the GMRES iteration for the linearized forward solution of the rSQP scheme is stopped with the loose tolerance in the range $10^{-2} \sim 10^{-3}$, whereas for the forward solution of the unconstrained lm-BFGS method, the tolerance of $10^{-10} \sim 10^{-14}$ is used [132, 148].

Chapter 5

SIMULATIONS AND EXPERIMENTAL RESULTS

5.1 Numerical Simulations

Numerical studies involving a digital mouse phantom were conducted to demonstrate the advantages of the angular-resolved measurement in the reconstruction processes.

A 3D volume mesh of the numerical mouse phantom was generated based on the surface geometry of a live mouse that was extracted using the developed surface scanner. The optical properties of the background medium inside the numerical mouse phantom were set to $\mu_a = 0.4$ cm^{-1} and $\mu_s' = 15$ cm^{-1} at both 475 nm excitation and 515 nm emission wavelengths. Two sphere (Ø 5 mm) fluorescent sources were placed 1 cm apart at the depth of ~8 mm below the surface as shown in Figure 5-1. The optical properties of fluorescent sources were assumed to be $\mu_a = 1$ cm^{-1}, a quantum yield of $\eta = 0.9$, and a fluorescence lifetime of $\tau = 4$ ns.

The numerical phantom was illuminated at a single point around the middle of the top surface directly above the two fluorescent sources inside the medium. The synthetic excitation and emission radiances on the mouse phantom surface were generated by solving the frequency domain ERT-based forward problem with the given distribution set of optical properties and fluorescent sources (Figure 5-2).

A mesh of 43,290 tetrahedron elements was used in the image reconstructions, for both angular-resolved and angular-averaged data sets. Each mesh node employed 80 discrete ordinates for the image reconstruction using angular-resolved data.

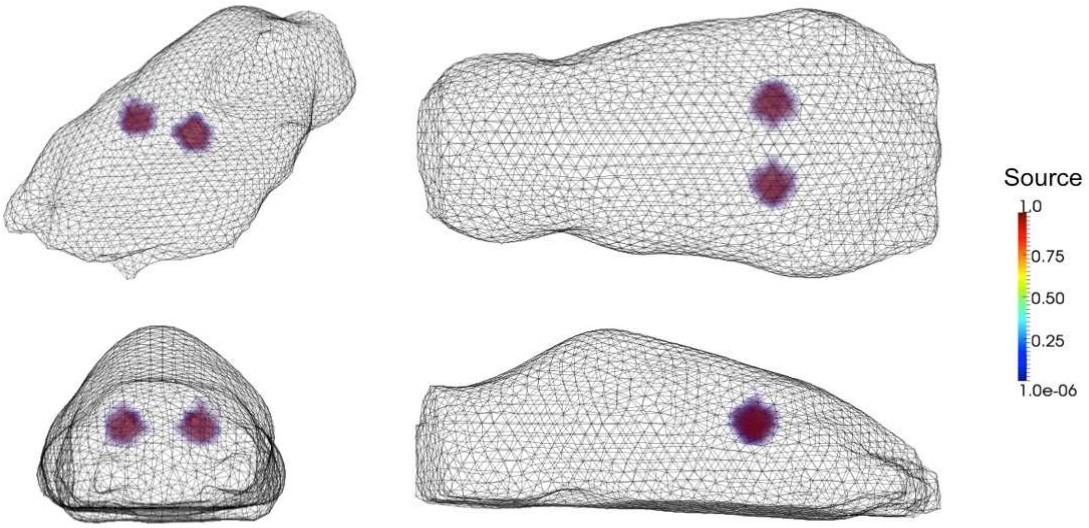

Figure 5-1. True source positions of two virtual fluorescent sources inside a digital mouse phantom (in clockwise direction, direction, perspective, top, side, and front views)

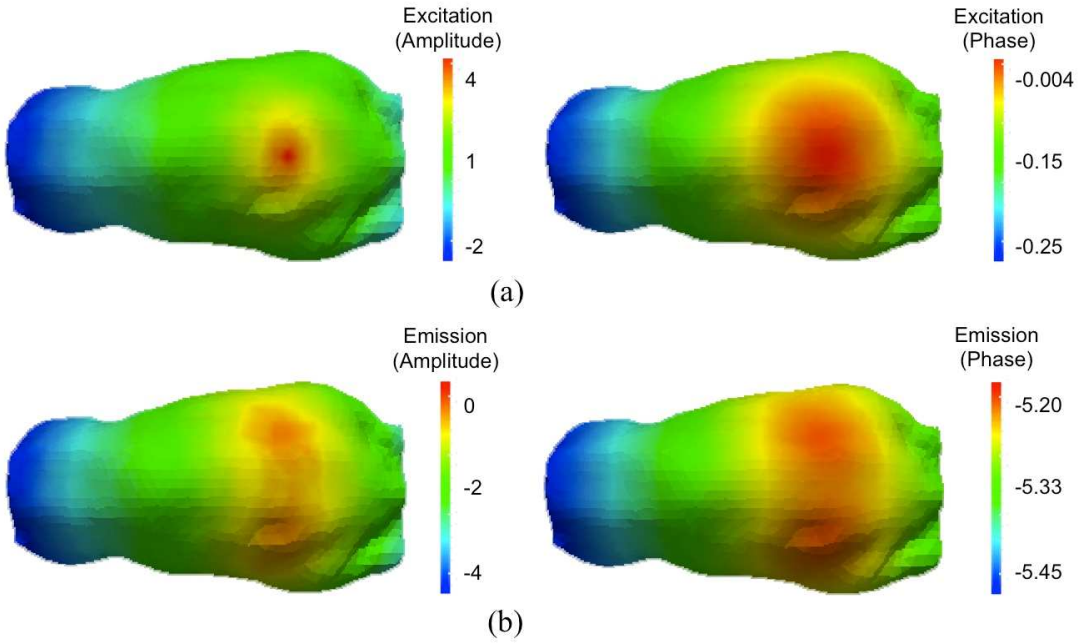

Figure 5-2. The synthetic radiance on the surface of the mouse phantom (a) excitation (left: amplitude, right: phase) and (b) emission (left: amplitude, right: phase)

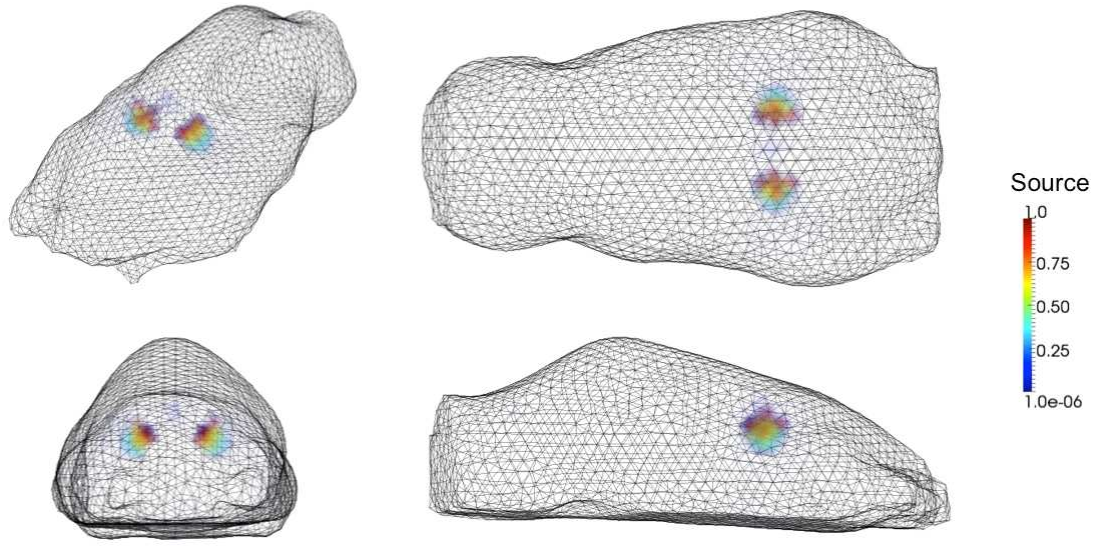

Figure 5-3. Reconstruction results using the angular-resolved data (in clockwise direction, perspective, top, side, and front views)

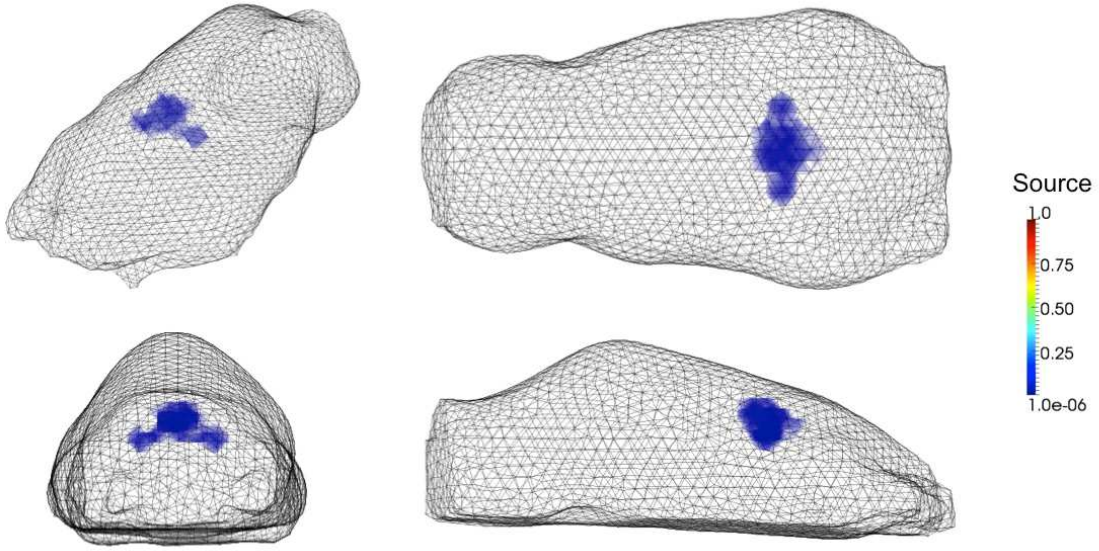

Figure 5-4. Reconstruction results using the angular-averaged data (in clockwise direction, perspective, top, side, and front views)

Figures 5-3 and 5-4 show the reconstruction results using angular-resolved data and angular-averaged data, respectively. As can be seen, the angular-resolved data leads to clear separation of the two fluorescent sources and more reliable quantification in the reconstruction result. However, when the angular-averaged data is used, the two sources cannot be separated.

5.2 Phantom Experiments

5.2.1 Optical Phantoms

For the characterization of the system's performance I employed a commercial optical phantom from Biomimic^{TM} from INO (Québec, Canada). This solid polyurethane phantom has a cylindrical shape and size (Ø 3.5 cm, 4.5 cm length) with a volume similar to that of an ordinary mouse. Black carbon was used as an absorber in the fabrication and provides a mostly flat absorption level over the visible and near infrared spectral range. The optical properties of phantoms were measured at 6 different wavelengths by using time-correlated single-photon counting (TCSPC) method. Table 5-1 summarizes the measured values of the optical properties at different wavelengths.

Table 5-1. Optical properties of the Biomimic^{TM} phantom at different wavelengths

Wavelength (nm)	475	515	575	661	757	828
μ_a (cm-1)	0.0768	0.0642	0.0693	0.0606	0.0512	0.0446
μ'_s (cm-1)	9.67	9.19	9.32	9.21	8.78	8.45

5.2.2 Single Fluorophore Experiment

A single hole was drilled into the cylindrical phantom (Ø 1.5 mm, 25 mm depth, and 5 mm away from the center of the phantom). This hole was filled with fluorescent solutions consisting of fluorescein (F2456-100G, Sigma-Aldrich Co.) diluted with distilled water to achieve by weight.

For the imaging processes, 475 nm excitation light illuminated three different points on the surface of the phantom and emission data was acquired using a combined filter set (515 nm long pass filter and 515/30 band pass filter). The optical properties at the excitation wavelength are μ_a = 0.0768 cm^{-1} and μ'_s = 9.67 cm^{-1} and those at the 515 nm emission wavelength are μ_a = 0.00642 cm^{-1} and μ'_s = 9.19 cm^{-1}.

The reconstruction was performed on the spatial and angular mesh of approximately 60,000 tetrahedron elements and 80 discrete ordinates. Figure 5-5 shows that the reconstructed position of the fluorescein-filled hole is well matched with the actual position in the optical phantom.

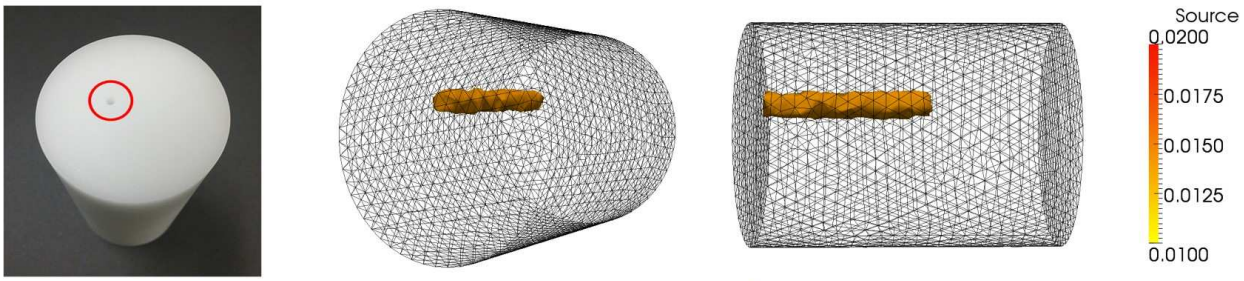

Figure 5-5. Phantom experiment (a) photograph of the phantom (red circle: insertion hole position) (b) image reconstruction results

5.3 Small Animal Imaging Studies

5.3.1 Case 1: Tumor Cells Positioned Subcutaneously

An initial animal experiment with a tumor-bearing mouse was conducted with the developed imaging system. Osteosarcoma cells (143B) transfected with GFP (pEGF-C1) were sorted multiple times by using flow cytometry to present 80~90% GFP positive expression. Considering the weak signals of GFP in the first attempt, the tumor cells (1×10^6 cells/ml in 100 μL PBS) were injected subcutaneously near the left kidney of a mouse. One week after the cell injection, the mouse was imaged to measure the tumor growth. For the FMT imaging, a 475 nm excitation wavelength was employed and the emission signals passing through a combined filter set (515 nm long pass filter and 515/30 band pass filter) were measured.

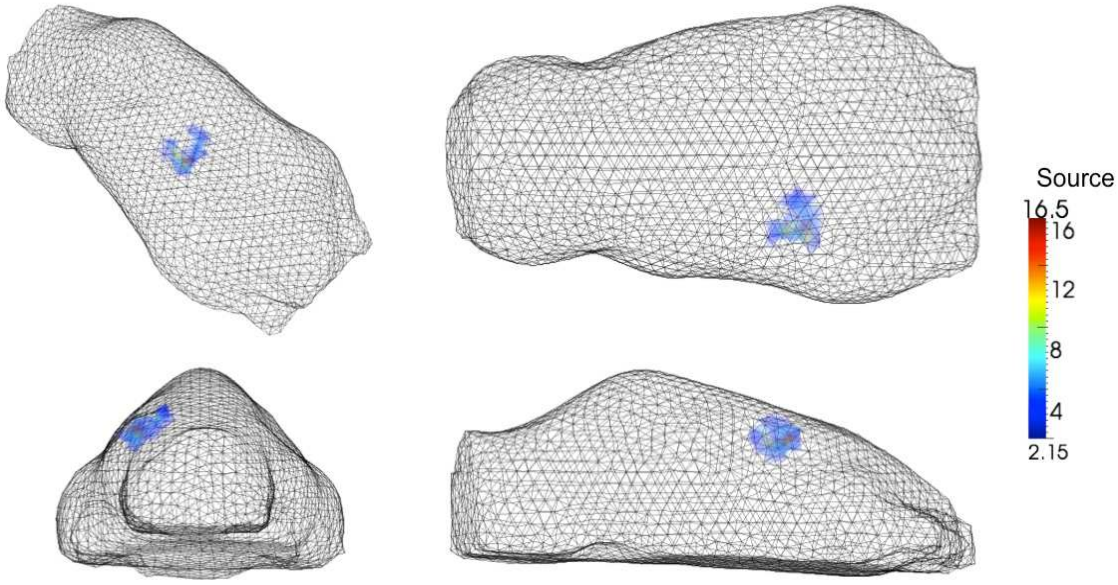

Figure 5-6. Reconstruction results of the tumor growth: one week after the subcutaneous tumor injection (in clockwise direction, perspective, top, side, and front views)

With one single illumination on the tumor area, total 37558 data points were obtained and used in the reconstruction. Figure 5-6 shows the reconstructed tumor location, which was confirmed by the planar imaging result using the Kodak In-Vivo Multispectral Imaging System FX (Carestream Health, Inc.).

5.3.2 Case 2: Tumor Cells Positioned near the Center of Abdomen

The GFP (pEGF-C1) tagged osteosarcoma cells (143B) of the previous animal experiment were used again in a longitudinal study of monitoring tumor growth. For this study, 1×10^7 cells/ml in 100 μL PBS were injected into the right iliac crest of a male athymic nude mouse with an X ray-guided intrapelvic injection as shown in Figure 5-7. Therefore the injection area of the tumor cells was near the center of the mouse abdomen. A week after the cell injection, the mouse was imaged with the new small animal imaging system once a week for three weeks. The same system setup employed for Case 1 was also used for the FMT imaging for this case. For the reconstruction a total of 20,334 data points from five illumination points were used together with a volume mesh having 125,000 tetrahedron elements.

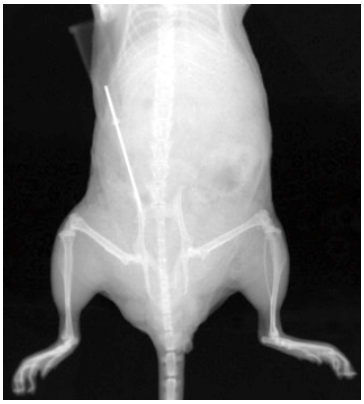

Figure 5-7. X-ray guided intrapelvic tumor cell injection

The reconstruction results in Figure 5-8, 5-9, and 5-10 clearly show the tumor growth over time from the first week to the third week. We present here a 3D volume contour of reconstructed GFP concentrations above the given threshold, which can provide a better way of possible quantitative assessment of the tumor growth over time. The calculated tumor volume increased up to about 7.43 times at the second week and 13.02 times at the third week in comparison with the first week.

At the third week imaging time point, the mouse was also imaged with the NanoSPECT/CT^{TM} imager of Bioscan Inc., USA. The CT results confirmed that the tumor area in the FMT reconstruction result corresponds well with the tumor boundaries obtained from the CT images (Figure 5-11) and with the shape of the explanted tumor (Figure 5-12b).

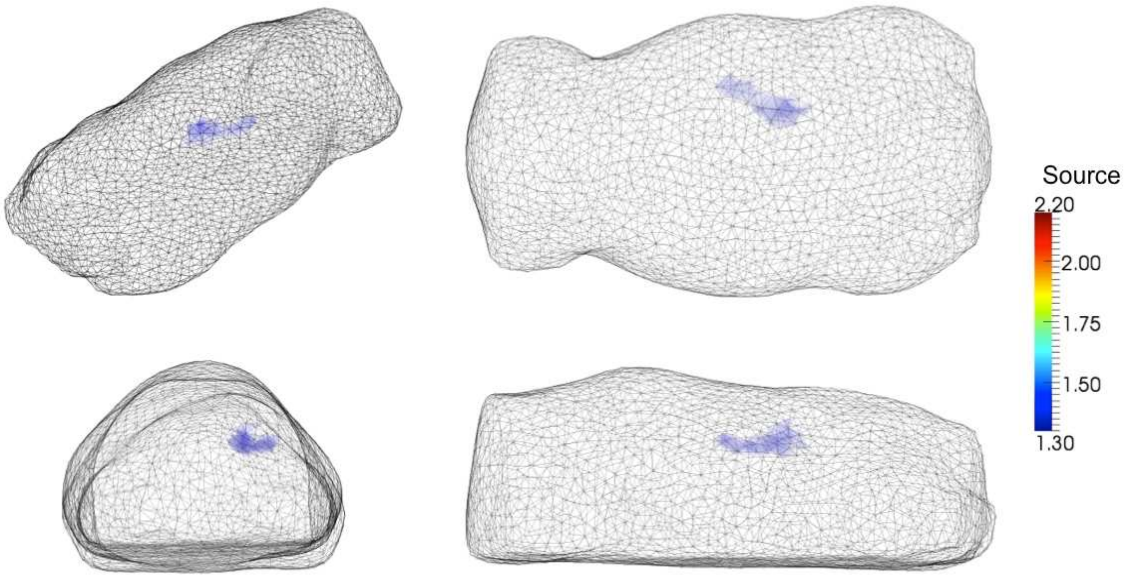

Figure 5-8. Reconstruction results of the tumor growth: the first week after the tumor injection (in clockwise direction, perspective, top, side, and front views)

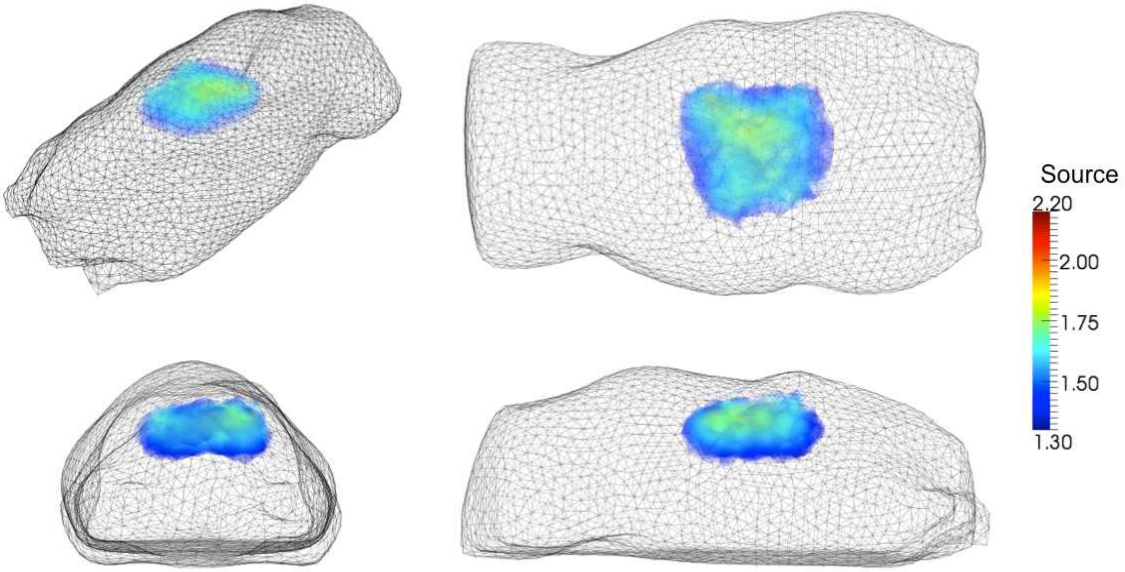

Figure 5-9. Reconstruction results of the tumor growth: the second week after the tumor injection (in clockwise direction, perspective, top, side, and front views)

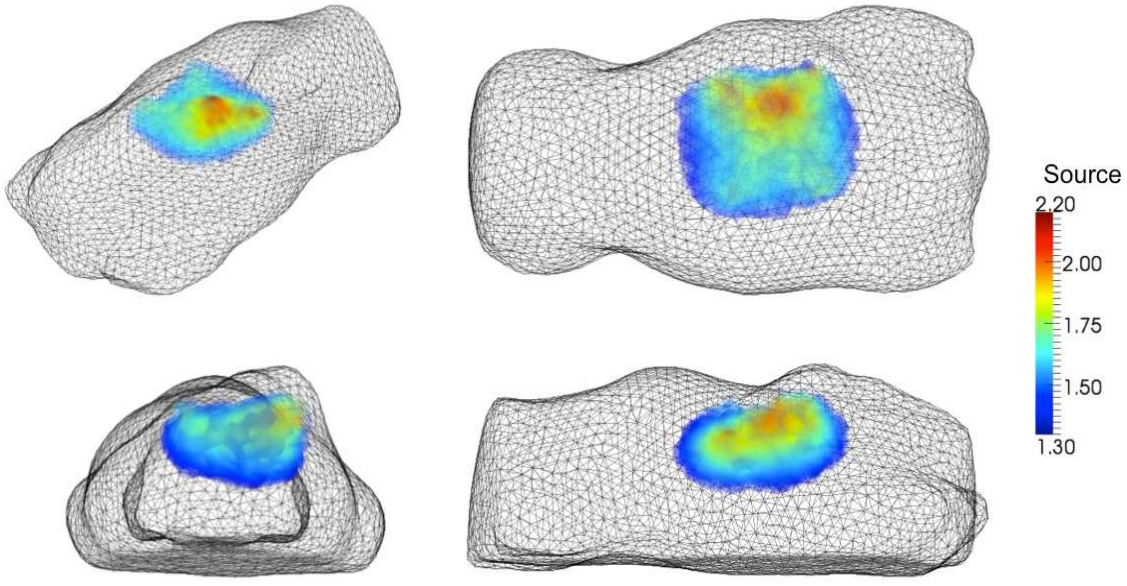

Figure 5-10. Reconstruction results of the tumor growth: the last third week after the tumor injection (in clockwise direction, perspective, top, side, and front views)

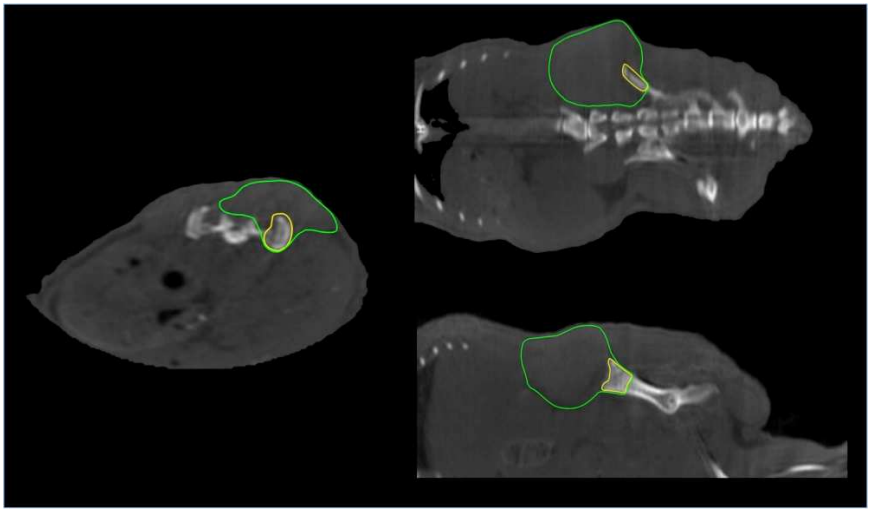

Figure 5-11. Results of CT imaging (axial, coronal and sagittal views in clockwise direction); In CT images, the areas enclosed by a green line and a yellow line present a soft tissue part and a bony part of the tumor respectively.

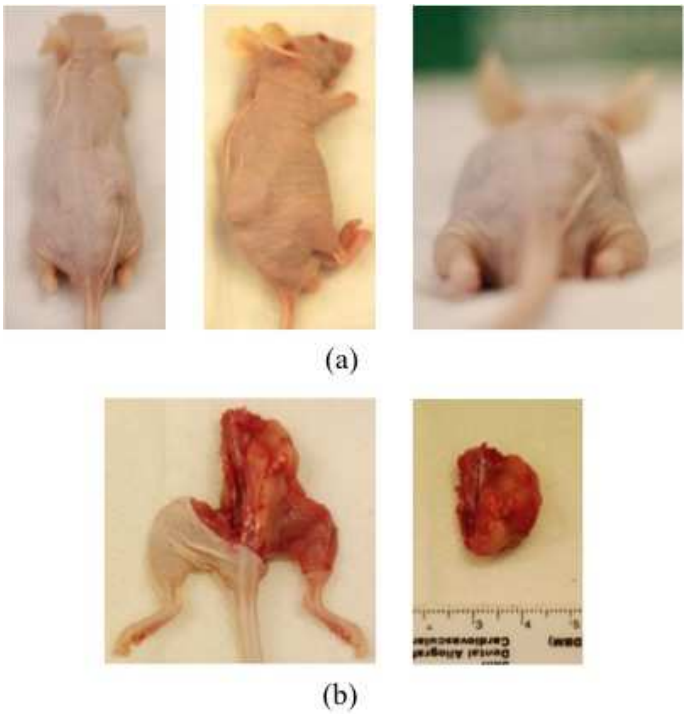

Figure 5-12. Photographs of (a) the mouse and (b) the explanted tumor at three weeks after the tumor cell injection 1

Chapter 6

SUMMARY AND FUTURE WORK

6.1 Summary

In vivo preclinical research has emerged as important tools for probing the nature of disease mechanisms and for bridging the gap between the traditional *in vitro* (or *ex-vivo*) studies and clinical findings. Optical imaging has become one of the most widely used standalone imaging modalities for preclinical small animal studies and is still growing in use. However, the inherent shallow penetration depth of optical imaging limits the precise localization and quantification of optical reporters. This unmet need can be addressed with the advancement of tomography techniques. This thesis focused on the improvement of existing optical tomography techniques by developing a new tomographic imaging system.

The newly developed imaging system allows for full non-contact whole-body small animal FMT imaging. To develop this system, an existing commercial imaging system, i.e., the Maestro 2 in vivo imaging system was analyzed through an initial exploratory study. Many prototype systems and most recently developed commercial systems were also reviewed. As a result, the double reflection mirror scheme was proposed to obtain multi-directional measurement with a single fixed position camera. Subsequently a frequency-domain small animal imaging system that makes use of the conical mirror imaging head was designed and implemented.

The frequency domain homodyne technique is utilized to separate the absorption and the scattering properties in tissues. For measuring the amplitude modulation and the phase shift, an intensity modulated laser beam (Ø 1-2 mm) is generated by using laser diodes, laser drivers, and

external signal generators. The generated laser beam is guided to the rotational gantry of the source illumination unit and is delivered to any surface area of the animal without obstructing the camera's FOV. The emitted light from the animal's body is consecutively reflected by the conical mirror imaging head and is projected onto an ICCD camera. Since the imaging head is positioned away from the animal, the unwanted back-reflections of light between the animal surface and the mirror surface is substantially reduced. Furthermore, the conical mirror shape of the imaging head provides the capability of angular-resolved data measurements.

To take full advantage of the obtained angular-resolved data in the image reconstruction, a novel ERT-based ray transfer operator and an ERT-based image reconstruction algorithm were developed. Using the surface geometry generated by the integrated surface scanner, the ERT-based ray transfer operator maps the spatial and angular distribution of emitted light on the animal's surface onto the pixels of the ICCD camera. With this angular-resolved data used as input, the ERT-based inverse algorithm reconstructs the position and concentration of fluorescent sources by using the PDE-constrained rSQP approach. It was shown that the use of angular-resolved data indeed leads to more accurate image reconstruction results. The reconstruction results of both phantom and animal experiments were well matched with the given information and the output of a CT imaging system. In addition, all results including numerical simulations were very promising as they were obtained with a fewer number of source illumination points (1-5 source points).

In conclusion, the developed small animal imaging system can perform non-contact whole body FMT imaging. Its strong advantages such as omni-directional and angular-resolved measurements remarkably improve the tomographic reconstruction results.

6.2 Future Work

Future work that is based on this completed thesis should focus on improving the efficiency of the system operation and extending the use of the FMT imaging system into the areas of BLT and DOT. In addition, the double-conical mirror scheme can be extended to various clinical applications such as non-contact breast cancer imaging or non-contact foot imaging for patients with peripheral artery disease. In both cases, a non-contact imaging modality would greatly enhance patient comfort. I will discuss these points in more detail in the following sections.

6.2.1 Small Animal Imaging System

Though the functions for the non-contact whole-body small animal FMT imaging have been completely implemented in this thesis, there is still room for potential improvements.

First, using the existing ICCD detection camera for the surface scanning, rather than additional webcams, would further simplify the imaging system. The surface scanner of the developed system uses two independent webcams on the movable platform. A commercial software is used for the mesh generation. Therefore the surface extraction requires moving the position of the scanner in accordance with the imaging process. Furthermore, cumbersome manual processes are needed to transform the domestic coordinates of the surface meshes into the global coordinate system of the imaging system. If the ICCD camera can be used to extract the surface mesh and its global coordinates directly, the components for the surface scanner will not be needed any more. This will reduce the costs and make the operation of the system more convenient and efficient.

Next, while the system was developed for small animal FMT imaging, it can be also utilized for small animal DOT and BLT imaging without modifications. Each technique will

provide different physiological or pathological information about the target animal. For example, DOT provides information about the blood oxygen saturation, BLT informs about the cell proliferation, and FMT provides information about the marker of a specific molecular mechanism. By integrating all these optical imaging modalities and results, one will be able to greatly extend information content in small animal studies.

Finally, a multimodality imaging system can be implemented. One of the strong advantages of the developed system is the unobstructed space around a target animal. This space can be used for combining the system with other gantry based imaging systems such as a micro-MRI and a micro-CT. A priori information from the anatomical imaging system can be used to improve optical tomographic reconstruction results and to provide better visualization of imaging results to the end users.

6.2.2 System Development for the Clinical Applications

To achieve simultaneous multi-directional detection with a single camera, I developed the double reflection mirror scheme in this thesis. Though the scheme was implemented here with conically shaped mirrors for imaging small animals, there is no particular limitation concerning the object shape or imaging applications.

Several clinical applications will be able to greatly benefit from this design as well. Figure 6-1 shows two examples, optical tomographic imaging of feet of diabetic patients with peripheral artery disease; and breast cancer imaging. Both applications of DOT are currently considered by several groups who rely on contact-based optical-fiber imaging heads [155-161]. As described in Chapter 3, the 2D cross sectional design for the mirror based imaging head can be extended to any shapes in three dimensions to maximize the detection area on the object body.

Since an outer boundary shape of the target object can vary from that of small animals to parts of the human body, the design flexibility is an important advantage for the system development. The maximized detection area and the multi-directional projection data will, in general, lead to improve image reconstruction results. In addition, if a curved shape mirror is employed, the angular-resolved data can be obtained to substantially increase the number of measurement data, which leads to improve reconstruction results. Furthermore, when the high prices of scientific cameras, the cost for developing mechanical components, and the throughput of the imaging process are considered, the mirror based imaging head can be a simple and cost effective solution for tomographic imaging instrumentations.

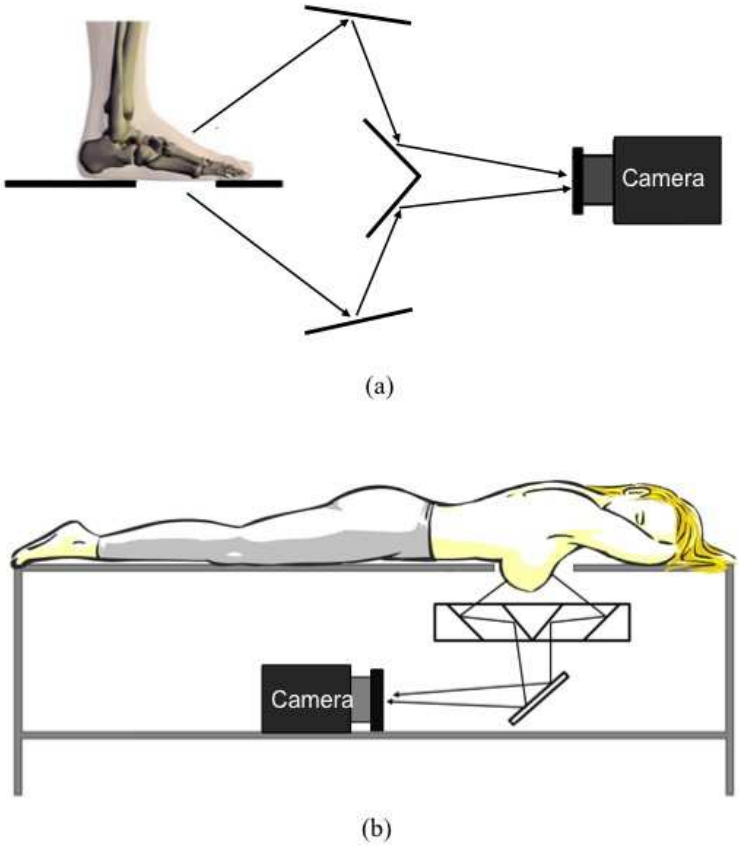

Figure 6-1 Application examples of the imaging head (a) foot imaging and (b) breast imaging (reproduced from the reference [157])

References

[1] B. Chance, R. R. Alfano, B. J. Tromberg, M. Tamura, E. M. Sevick-Muraca, Optical tomography and spectroscopy of tissue IV, Proceedings of SPIE **6434** (2007).

[2] A. P. Gibson, J. C. Hebden, S. R. Arridge, "Recent advances in diffuse optical imaging, Physics in Medicine and Biology," Physics in Medicine and Biology **50**(4), R1-R43 (2005).

[3] W. M. Star, "Diffusion theory of light transport," *in Optical-Thermal Response of Laser-Irradiated Tissue*. A. J. Welch and M. J. C. van Gemert ed. New York: Springer, (2011).

[4] D. A. Boas, D. H. Brooks, E. L. Miller, C. A. DiMarzio, M. Kilmer, R. J. Gaudtte, and Q. Zhang, "Imaging the Body with Diffuse Optical Tomography," IEEE Signal Processing Magazine, 57-75 (2001).

[5] S. R. Arridge, J. C. Schotland, "Optical tomography: forward and inverse problems," Inverse Problems, **25** (2009).

[6] D. A. Boas, B. H. Brooks, E. L. Miller, C. A. DiMarzio, M. Kilmer, R. J. Gaudette, and Q. Zhang, "Imaging the body with diffuse optical tomography," IEEE Signal Processing Magazine, 57-75 (2001).

[7] X. Zhou, L. Chen, C. Tse, T. B. Penney, and N. Chen, "Theoretical investigation of near-infrared light path in multi-layer brain models for three DOT systems," Photonics Global Conference, 1-5 (2012).

[8] C. Zhu and Q. Liu, "Review of Monte Carlo modeling of light transport in tissues," Journal of Biomedical Optics **18**(5), 050902 (2013).

[9] J. B. Domínguez and Y. Bérubé-Lauzière, "Diffuse optical tomographic imaging of biological media by time-dependent parabolic SPN equations: a two-dimensional study," Journal of Biomedical Optics **17**(8), 086012 (2012).

[10] K. Ren, G. Bal, A. H. Hielscher, "Frequency-domain optical tomography based on the equation of radiative transfer," SIAM Journal of Scientific Computing, **28**(4), 1463-1489 (2006).

[11] A. D. Klose, "The forward and inverse problem in tissue optics based on the radiative transfer equation: A brief review," Journal of Quantitative Spectroscopy & Radiative Transfer, **111**(11), 1852-1853 (2010).

[12] H.K. Kim, A.H. Hielscher, “A PDE-constrained SQP algorithm for optical tomography based on the frequency-domain equation of radiative transfer,” Inverse Problems **25**, 015010 (2009).

[13] H.K. Kim, J. Lee, A.H. Hielscher, “PDE-constrained fluorescence tomography with the frequency-domain equation of radiative transfer,” IEEE Journal of Selected Topics in Quantum Electronics **16**(4), 793-803 (2010).

[14] H. Gao and H. Zhao. "Multilevel bioluminescence tomography based on radiative transfer equation Part 2: total variation and l1 data fidelity." Optics Express **18**(3), 2894-2912 (2010).

[15] Y. Tan, M. Novo, L. Yao, L. Zhou, and H. Jiang, "In Vivo monitoring of stem cells in drosophila pupae using the radiative transfer equation-based fluorescence molecular tomography," Molecular Imaging and Biology **13**(50), 868-873 (2011).

[16] T. Tarvainen, V. Kolehmainen, O. Lehtikangas, J. P. Kaipio, and S. R. Arridge, "Utilising the coupled radiative transfer-diffusion model in diffuse optical tomography," Proceedings of OSA-SPIE **8799**, 879907 (2013).

[17] T. Tarvainen, V. Kolehmainen, S. R. Arridge, and J. P. Kaipio, "Image reconstruction in diffuse optical tomography using coupled radiative transport-diffusion model," Journal of Quantitative Spectroscopy and Radiative Transfer **112**(16), 2600-2608 (2011).

[18] A. D. Klose, "The forward and inverse problem in tissue optics based on the radiative transfer equation: a brief review," Journal of Quantitative Spectroscopy and Radiative Transfer **111**(11), 1852-1853 (2010).

[19] M. Marin, F. Asllanaj, and D. Maillet. "Sensitivity analysis to optical properties of biological tissues subjected to a short-pulsed laser using the time-dependent radiative transfer equation," Journal of Quantitative Spectroscopy and Radiative Transfer **133**, 117-127 (2014).

[20] Y. Lu and E. M. Sevick-Muraca. "Fluorescence-enhanced optical tomography with a radiative transfer-based model," Biomedical Imaging: From Nano to Macro, IEEE International Symposium, 484-487 (2011).

[21] Optical Properties Spectra, http://omlc.ogi.edu/spectra/index.html (2001).

[22] C. Depeursinge, “Optical Tomography,” in *Tomography*. P. Grangeat, ed. New Jersey: John Wiley & Sons, Inc., (2009).

[23] C. H. Schmitz, M. Locker, J. M. Lasker, A. H. Hielscher, and R. L. Barbour, "Instrumentation for fast functional optical tomography," Review of Scientific Instruments **73**, 429-39 (2002).

[24] F. E. Schmidt, M. E. Fry, E. M. C. Hillman, J. C. Hebden, and D. T. Delpy, “A 32-channel time resolved instrument for medical optical tomography,” Review of Scientific Instruments **73**, 256-265 (2000).

[25] B. W. Pogue, M. Testorf, T. McBride, U. Osterberg, and K. Paulsen, “Instrumentation and design of a frequency-domain diffuse optical tomography imager for breast cancer detection,” Optics Express, **1**(13), 391-403 (1997).

[26] S. Fantini, M. A. Franceschini, J. S. Maier, S. A. Walker, B. Barbieri, and E. Gratton, “Frequency-Domain Multichannel Optical Detector for non-Invasive Tissue Spectroscopy and Oximetry,” Optical Engineering **34**, 32-42 (1995).

[27] S. Keren, O. Gheysens, C. S. Levin, and S. S. Gambhir, "A comparison between a time domain and continuous wave small animal optical imaging system," IEEE Transactions on Medical Imaging **27**, 58-63 (2008).

[28] J. Fishkin, E. Gratton, M. J. V. Ven, and W. W. Mantullin, “Diffusion of intensity modulated near infrared light in turbid media,” in *Time–Resolved Spectroscopy and Imaging of Tissues* B. Chance, ed. Proceedings of the Society of Photo-Optical Instrumentation Engineers **1431**, 122-135 (1991).

[29] B. J. Tromberg, L. O. Svaasand, T. Tsay, and R. C. Haskell, “Properties of photon density waves in multiple-scattering media,” Applied Optics, **32**(4), 607-616 (1993).

[30] F. Leblond, S. C. Davis, P. A. Valdés, and B. W. Pogue, “Pre-clinical whole-body fluorescence imaging: Review of instruments, methods and applications,” Journal of Photochemistry and Photobiology B: Biology **98**, 77-94 (2010).

[31] B. Tromberg, "Optical Scanning and Breast Cancer," Academic Radiology, **12**, 923-924 (2005).

[32] X. Intes, "Time-Domain Optical Mammography SoftScan: Initial Results," Academic Radiology, **12**, 934-947 (2005).

[33] S. Srinivasan, B. W. Pogu, B. Brooksby, S. Jiang, H. Dehghani, C. Kogel, W. A. Wells, S. Sp. Poplack, and K. D. Paulsen, "Near-Infrared Characterization of Breast Tumors In Vivo using Spectrally-Constrained Reconstruction," Technology in Cancer Research & Treatment, **4**, 513-526 (2005).

[34] B. Tromberg, A. Cerussi, N. Shah, M. Compton, A. Durkin, D. Hsiang, J. Butler, R. Mehta, "Imaging in breast cancer: Diffuse optics in breast cancer: Diffuse optics in breast cancer: detecting tumors in pre-menopausal women and monitoring neoadjuvant chemotherapy," Breast Cancer Research, **7**, 279-285 (2005).

[35] A. Rice and C. M. Quinn, "Angiogenesis, thrombospodin, and ductal carcinoma in situ of the breast," Journal of Clinical Pathology **55**, 569-574 (2002).

[36] P. Vaupel, A. Mayer, and M. Höeckel, "Tumor Hypoxia and Malignant Progression," Methods in Enzymology **381**, 335-354 (2004).

[37] M. N. Kim, T. Durduran, S. Franos, E. M. Buckley, C. Zhou, G. Yu, B. L. Edlow, E. Mahoney-Wilensky, M. S. Grady, J. Levine, J. A. Detre, J. H. Greenberg, and A. G. Yodh, "Diffuse Optical Measurements of Cerebral Blood Flow and Oxygenation in Patients after Traumatic Brain Injury or Subarachnoid Hemorrhage," Biomedical Optics Optical Techniques in the Clinic, BSuD5 (2008).

[38] J. C. Hebden and T. Austin, "Optical tomography of the neonatal brain," European Radiology **17**, 2926-2933 (2007).

[39] D. G. Hirtz, "Report of the National Institute of Neurological Disorder and Stroke workshop on near infrared spectroscopy," Pediatrics **91**(2), 414–417 (1993).

[40] S. R. Hintz, W. F. Cheong, J. P. V. Houten, D. K. Stevenson, and D. A. Benaron, "Bedside imaging of intracranial hemorrhage in the neonate using light: comparison with ultrasound, computed tomography, and magnetic resonance imaging," Pediatrics **45**(1), 54–59 (1999).

[41] A. H. Hielscher, H. K. Kim, L. D. Montejo, S. Blaschke, U. J. Netz, P. A. Zwaka, G. Illing, G. A. Muller, and J. Beuthan, "Frequency-domain optical tomographic imaging of arthritic finger joints," IEEE Transactions on Medical Imaging **30**(10), 1725-1736 (2011).

[42] Y. Xu, N. Iftimia, H. Jiang, L. Key and M. Bolster, "Imaging of in vitro and in vivo bones and joints with continuous-wave diffuse optical tomography," Optics Express **8**(7), 447-451 (2001).

[43] D. J. DeGraff, V. L. Robinson, J. B. Shah, W. D. Brandt, G. Sonpavde, Y. Kang, M. Liebert, X. Wu, and J. A. Taylor. "Current preclinical models for the advancement of translational bladder cancer research," Molecular Cancer Therapeutics **12**(2), 121-130 (2013).

[44] C. V. Borlongan, "Recent preclinical evidence advancing cell therapy for Alzheimer's disease," Experimental Neurology **237** (1), 142-146 (2012).

[45] W. R. Sellers, "A blueprint for advancing genetics-based cancer therapy." Cell **147**(1), 26-31 (2011).

[46] A. Kumar, C. A. Haralampus, M. Hughes, D. Rouy, N. Cresswell, R. Braun, D. Turner, D. Amrani, D. Motlagh, and G. L. Schaer. "Assessment of safety, accuracy, and human CD34+ cell retention after intramyocardial injections with a helical needle catheter in a porcine model," Catheterization and Cardiovascular Interventions **81**(6), 970-977 (2013).

[47] N. P. Reddy, S. Miyamoto, K. Araki, T. Liu, M. Feldman, B. W. O'Malley, and D. Li. "A novel orthotopic mouse model of head and neck cancer with molecular imaging," The Laryngoscope **121**(6), 1202-1207 (2011).

[48] M. A. Mackanos, E. D. Jansen, and C. H. Contag, "Molecular Imaging Using Fluorescence and Bioluminescence to Reveal Tissue Response to Laser-Mediated Thermal Injury," *in Optical-Thermal Response of Laser-Irradiated Tissue*. A. J. Welch and M. J. C. van Gemert ed. New York: Springer, (2011).

[49] S. Dufort, L. Sancey, C. Wenk, V. Josserand, and J. L. Coll, "Optical small animal imaging in the drug discovery process," Biochimica et Biophysica Acta (BBA)-Biomembranes **1798**(12), 2266-2273 (2010).

[50] H. Tsai, B. Z. Bentz, V. Chelvam, V. Gaind, K. J. Webb, and P. S. Low, "In Vivo Optical Imaging of Kinetics in a Small Animal for Folate-Targeted Drug Development," Optical Trapping Applications, JW3B.5 (2013).

[51] A. E. Moran, K. L. Holzapfel, Y. Xing, N. R. Cunningham, J. S. Maltzman, J. Punt, and K. A. Hogquist, "T cell receptor signal strength in Treg and iNKT cell development demonstrated by a novel fluorescent reporter mouse," Journal of Experimental Medicine **208**(6), 1279-1289 (2011).

[52] S. I. Kojima and G. G. Borisy, "An image-based, dual fluorescence reporter assay to evaluate the efficacy of shRNA for gene silencing at the single-cell level," F1000Research 3:60 (2014).

[53] K. S. Kim, S. Park, S. Lee, S. B. Kang, J. Lee, S. Lee, and C. Ryu, "A novel fluorescent reporter system for monitoring and identifying RNase III activity and its target RNAs," RNA biology, **9**(9) (2012).

[54] Y. Lu, H. B. Machado, Q. Bao, D. Stout, H. Herschman, and A. F. Chatziioannou. "In vivo mouse bioluminescence tomography with radionuclide-based imaging validation," Molecular Imaging and Biology **13**(1), 53-58 (2011).

[55] M. A. Lewis, E. Richer, N. V. Slavine, V. D. Kodibagkar, T. C. Soesbe, P. P. Antich, and R. P. Mason, "A Multi-Camera System for Bioluminescence Tomography in Preclinical Oncology Research," Diagnostics **3**(3), 325-343 (2013).

[56] C. Qin, J. Feng, S. Zhu, X. Ma, J. Zhong, P. Wu, Z. Jin, and J. Tian, "Recent advances in bioluminescence tomography: methodology and system as well as application," Laser& Photonics Reviews **8**(10), 94-114 (2014).

[57] X. Michalet, F. F. Pinaud, L. A. Bentolila, J. M. Tsay, S. Doose, J. J. Li, G. Sundaresan, A. M. Wu, S. S. Gambhir, and S. Weiss, "Quantum dots for live cells, in vivo imaging, and diagnostics," Science **307**(5709), 538–544 (2005).

[58] A. Corlu, “Multi-spectral and fluorescence diffuse optical tomography of breast cancer,” PhD dissertation, University of Pennsylvania (2007).

[59] A. D. Klose, “Radiative transfer of luminescence light in biological tissue,” *in Light Scattering Reviews 4*. A. Kokhanovsky, ed. New York: Springer, (2009).

[60] S. R. Arridge, “Optical tomography in medical imaging,” Inverse Problem **15**, R41-R93 (1999).

[61] J. Feng, K. Jia, S. Zhu, X. Yang, and J. Tian, "Bioluminescence Tomography Imaging In Vivo: Recent Advances," IEEE Journal of Selected Topics in Quantum Electronics **8**(4), 1394-1402 (2012).

[62] A. D. Klose, V. Ntziachristos, and A. H. Hielscher, “The inverse source problem based on the radiative transfer equation in optical molecular imaging,” Journal of Computational Physics **202**, 323-345 (2005).

[63] R. T. Sadikot and T. S. Blackwell, “Bioluminescence imaging,” Proceedings of the American Thoracic Society **2**(6), 537-540 (2005).

[64] T. Troy, D. Jekic-McMullen, L. Sambucetti, and B. Rice, "Quantitative Comparison of the Sensitivity of Detection of Fluorescent and Bioluminescent Reporters in Animal Models," Molecular Imaging, **3**(1), 9-23 (2004).

[65] D. Y. Paithankar, A. U. Chen, B. W. Pogue, M. S. Patterson, and E. M. Sevick-Muraca, "Imaging of fluorescent yield and lifetime from multiply scattered light reemitted from random media," Applied Optics, **36**(10), 2260-2272 (1997).

[66] E. Shives, Y. Xu, and H. Jiang, "Fluorescence lifetime tomography of turbid media based on an oxygen-sensitive dye," Optics Express, **10**(26), 1557-1562 (2002).

[67] R. Roy, A. Godavarty, and E. M. Sevick-Muraca, "Fluorescence-enhanced three-dimensional lifetime imaging: A phantom study, " Physics in Medicine and Biology, **52**(14), 4155-4170 (2007).

[68] A. T. N. Kumar, S. B. Raymond, G. Boverman, D. A. Boas, and B. J. Bacskai, "Time resolved fluorescence tomography of turbid media based on lifetime constant," Optics Express **14**(25), 12255-12270 (2006).

[69] G. Wang, Y. Li, and M. Jiang, "Uniqueness theorems in bioluminescence tomography," Medical Physics, **31**(8), 2289-2299 (2004).

[70] X. Gu, Q. Zhang, L. Larcom, and H. Jiang, "Three-dimensional bioluminescence tomography with model-based reconstruction," Optics Express **12**(17), 3996-4000 (2004).

[71] J. Feng, K. Jia, S. Zhu, X. Yang, and J. Tian, "Bioluminescence Tomography Imaging In Vivo: Recent Advances," IEEE Journal of Selected Topics in Quantum Electronics **18**(4), 1394-1402 (2012).

[72] J. Bai, "Fluorescence molecular tomography," *in Molecular Imaging- Fundamentals and Applications*. J. Tian, ed. New York: Springer, (2012).

[73] R. Sharma and A. Sharma, "21.1 Tesla Magnetic Resonance Imaging Apparatus and Image Interpretation: First Report of a Scientific Advancement," Recent Patents on Medical Imaging **1**, 89-105 (2011).

[74] J. Comley, "In vivo preclinical imaging – an essential tool in translational research," Drug Discovery World Summer, 58-71 (2011).

[75] P. Zanzonico, "Noninvasive Imaging for Supporting Basic Research," *in Small Animal Imaging-Basic and Practical Guide.* F. Kiessling, and B. J. Pichler, ed. New York: Springer, (2010).

[76] W. Koba, K. Kim, M. L. Lipton, L. Jelicks, B. Das, L. Herbst, and E. Fine, "Imaging devices for Use in Small Animals," Seminars in Nuclear Medicine **41**, 151-165 (2011).

[77] M. A. Pysz, S. S. Gambhir, and J. K. Willmann, "Molecular imaging: current status and emerging strategies," Clinical Radiology **65**, 500-516 (2010).

[78] B. W. Pogue, M. Testorf, T. McBride, U. Osterberg, and K. Paulsen, "Instrumentation and design of a frequency-domain diffuse optical tomography imager for breast cancer detection," Optics Express **1**(13), 391-403 (1997).

[79] M. L. Flexman, M. A. Khalil, R. A. Abdi, H. K. Kim, C. J. Fong, E. Desperito, D. L. Hershman, R. L. Barbour, and A. H. Hielscher, "Digital optical tomography system for dynamic breast imaging," Journal of Biomedical Optics **16**(7), 076014 (2011).

[80] E. E. Graves, J. Ripoll, R. Weissleder, and V. Ntziachristos, "A submillimeter resolution fluorescence molecular imaging system for small animal imaging," Medical Physics **30** (5), 901-911 (2003).

[81] R. Choe, A. Corlu, K. Lee, T. Durduran, S. D. Konecky, M. Grosicka-Koptyra, S. R. Arridge, B. J. Czerniecki, D. L. Fraker, A. DeMichele, B. Chance, M. A. Rosen, and A. G. Yodh, "Diffuse optical tomography of breast cancer during neoadjuvant chemotherapy: A case study with comparison to MRI," Medical Physics **32**(4), 1128-1139 (2005).

[82] R. W. Holt, F. Leblond, and B. W. Pogue, "Toward ideal imaging geometry for recovery independence fluorescence molecular tomography," Proceedings of SPIE **8574**, 857403 (2013).

[83] N. Delionlanis, T. Lasser, D. Hyde, A. Sourbret, J. Ripoll, and V. Ntziachristos, "Free-space fluorescence molecular tomography utilizing 360° geometry projections," Optics Letters **32**(4), 382-384 (2007).

[84] G. Wang, H. Shen, K. Duraiaj, X. Qian, and W. X. Cong, "The first bioluminescence tomography system for simultaneous acquisition of multiview and multispectral Data," International Journal of Biomedical Imaging **2006**, 1-8 (2006).

[85] C. Gardner, J. Dutta, G. S. Mitchell, S. Ahn, C. Li, P. Harvey, R. Gershman, S. Sheedy, J. R. Mansfield, S. R. Cherry, R. M. Leahy, and R. M. Levenson, "Improved in vivo fluorescence tomography and quantitation in small animals using a novel multiview, multispectral imaging system," Biomedical Optics OSA Biological and Drug Discovery Imaging, BTuF1 (2010).

[86] J. A. Guggenheim, H. R. A. Basevi, J. Frampton, I. B. Styles, and H. Dehghani, "Multi-modal molecular diffuse optical tomography system for small animal imaging," Measurement Science and Technology **24**, 105405 (2013).

[87] C. Li, G. S. Mitchell, J. Dutta, S. Ahn, R. M. Leahy, and S. R. Cherry, " A three-dimensional multispectral fluorescence optical tomography imaging system for small animals based on a conical mirror design," Optics Express, **17**(9), 7571-7585 (2009).

[88] A. H. Hielscher, H. K. Kim, L. D. Montejo, S. Blaschke, U. J. Netz, P. A. Zwaka, G. Illing, G. A. Müller, and J. Beuthan, "Frequency-domain optical tomography imaging of arthritic Finger Joints," IEEE Transactions on Medical Imaging **30**(10), 1725-1736 (2011).

[89] S. V. Patwardhan, S. R. Bloch, S. Achilefu, and J. P. Culver, "Time-dependent whole-body fluorescence tomography of probe bio-distribution in mice," Optics Express **13**(7), 2564-2577 (2005).

[90] H. Meyer, A. Garofalakis, G. Zacharakis, S. Psycharakis, C. Mamalaki, D. Kloussis, E. N. Economou, V. Ntziachristos, and J. Ripoll, "Noncontact optical imaging in mice with full angular coverage and automatic surface extraction," Applied Optics **46**(17), 3617-3627 (2007).

[91] G. Hu, J. Yao, J. Bai, "Full-angle optical imaging of near-infrared fluorescent probes implanted in small animals," Progress in Natural Science **18**(6), 707-711 (2008).

[92] E. Lapointe, J. Pichette, and Y. Bérubé-Lauziéré, "A multi-view time-domain non-contact diffuse optical tomography scanner with dual wavelength detection for intrinsic and fluorescence small animal imaging," Review of Scientific Instruments **83**(6), 063703, (2012).

[93] T. Pöschinger, E. Janunts, and A. Langenbucher, "Development of an Optical Fluorescence Tomography System for Small Animal Imaging," World Congress on

Medical Physics and Biomedical Engineering 2009, IFMBE Proceedings, **25**, 123-126 (2009).

[94] C. Li, G. S. Mitchell, J. Dutta, S. Ahn, R. M. Leahy, and S. R. Cherry, " A three-dimensional multispectral fluorescence optical tomography imaging system for small animals based on a conical mirror design," Optics Express, **17**(9), 7571-7585 (2009).

[95] A. Kienle, F. K. Foster, and R. Hibst, "Anisotropy of light propagation in biological tissue," Optics Letters, **29**(22), 2617-2619 (2004).

[96] H. Gao, and H. Zhao, "Multilevel bioluminescence tomography based on radiative transfer equation Part1: l1 regularization," Optics Express, **18**(3), 1854-1871 (2010).

[97] J. Folkman, M. Bach, J. W. Rowe, F. Davidoff, P. Lambert, C. Hirsch, A. Goldberg, H. H. Hiatt, J. Glass, and E. Henshaw, "Tumor angiogenesis: therapeutic implications," New England Journal of Medicine **285**(21), 1182-1186 (1971).

[98] V. R. Muthukkaruppan, L. Kubai, and R. Auerbach, "Tumor-induced neovascularization in the mouse eye," Journal of the National Cancer Institute **69**(3), 699-708 (1982).

[99] L. Holmgren, M. S. O'Reilly, and J. Folkman, "Dormancy of micrometastases: Balanced proliferation and apoptosis in the presence of angiogenesis suppression," Nature Medicine **1**(2), 149-153 (1995).

[100] C. Sessa, A. Guibal, G. D. Conte, and C. Rüegg, "Biomarkers of angiogenesis for the development of antiangiogenic therapies in oncology: tools or decorations?," Nature Reviews Clinical Oncology **5**(7), 378-391 (2008).

[101] Y. R. Kim, A. Yudina, J. Figueiredo, W. Reichardt, D. Hu-Lowe, A. Petrovsky, H.W. Kang, D. Torres, U. Mahmood, R. Wissleder, and A. A. Bogdanov, Jr. "Detection of Early Antiangiogenic Effects in Human Colon Adenocarcinoma Xenografts: In vivo Changes of Tumor Blood Volume in Response to Experimental VEGFR Tyrosine Kinase Inhibitor, " Cancer Research **65**(20), 9253-9260 (2005).

[102] F. Kabbinavar, H.I. Hurwitz, L. Fehrenbacher, N. Meropol, W.F. Novotny, G. Lieberman, S. Griffing, and E. Bergsland, "Phase II, randomized trial comparing bevacizumab plus fluorouracil (FU)/leucovorin (LV) with FU/LV alone in patients with metastatic colorectal cancer," Journal of Clinical Oncology **21**, 60–65 (2003).

[103] H. Hurwitz, L. Fehrenbacher, W. Novotny, T. Cartwright, J. Hainsworth, W. Heim, J. Berlin, A. Baron, S. Griffing, E. Holmgren, N. Ferrara, G. Fyfe, B. Rogers, R. Ross, and F. Kabbinavar, "Bevacizumab plus irinotecan, fluorouracil, and leucovorin for metastatic colorectal cancer," New England Journal of Medicine **350**, 2335–2342 (2004).

[104] J. G. Bender, E. M. Cooney, J. J. Kandel, and D. J. Yamashiro, "Vascular remodeling and clinical resistance to antiangiogenic cancer therapy," Drug Resistance Updates **7**(4-5), 289-300 (2004).

[105] R. Pazdur, *FDA approval for Bevacizumab* (2009).

[106] G. Bergers and D. Hanahan, "Modes of resistance to anti-angiogenesis therapy," Nature Reviews Cancer **8**(8), 592-603 (2008).

[107] K. J. Kim, B. Li, J. Winder, M. Armanini, N. Gillett, H. S. Philips, and N. Ferrara, "Inhibition of vascular endothelial growth factor-induced angiogenesis suppresses tumor growth in vivo," Nature, **362**(6423), 841-844 (1993).

[108] B. Turkbey, H, Kobayashi, M. Ogawa, M. Bernardo, and P.L. Choyke, "Imaging of Tumor Angiogenesis: Functional or Targeted?" American Journal of Roentgenology **193** (2009).

[109] N.R. Smith, N.H. James, I. Oakley, A. Wainwright, C. Copley, J. Kendrew, L. M. Womersley, J. M. Jürqensmeier, S. R. Wedge, and S. T. Barry, "Acute pharmacodynamic and antivascular effects of the vascular endothelial growth factor signaling inhibitor AZD2171 in Calu-6 human lung tumor xenografts," Molecular Cancer Therapeutics **6**, 2198-2208 (2007).

[110] D.W. Miller, S. Vosseler, N. Mirancea, D.J. Hicklin, P. Bohlen, H.E. Volcker, F.G. Holz and N.E. Fusenig, "Rapid Vessel Regression, Protease Inhibition, and Stromal Normalization upon Short-Term Vascular Endothelial Growth Factor Receptor 2 Inhibition in Skin Carcinoma Heterotransplants," American Journal of Pathology **167**(5), 1389-1403 (2005).

[111] R. K. Jain, "Normalization of tumor vasculature: an emerging concept in antiangiogenic therapy," Science **307**(5706), 58-62 (2005).

[112] D. J. Cuccia, F. Bevilacqua, A. J. Durkin, S. Merritt, B. J. Tromberg, G. Gulsen, H. Yu, J. Wang, and O. Nalcioglu, "In vivo Quantification of Optical Contrast Agent Dynamics in Rat Tumors by Use of Diffuse Optical Spectroscopy with Magnetic Resonance Imaging Coregistration," Applied Optics **42**(16), 2940-2950 (2003).

[113] R. T. Tong, Y. Boucher, S. V. Kozin, F. Winkler, D. J. Hicklin, and R. K. Jain, "Vascular Normalization by Vascular Endothelial Growth Factor Receptor 2 Blockade Induces a Pressure Gradient Across the Vasculature and Improves Drug Penetration in Tumors," Cancer Research **64**, 3731-3736 (2004).

[114] E. M. C. Hillman and A. Moore, "All-optical anatomical co-registration for molecular imaging of small animals using dynamic contrast," Nature photonics **1**, 526-530 (2007).

[115] D. H. Rowe, J. Z. Huang, M. L. Kayton, R. Thompson, A. Troxel, K. M. O'Toole, D. Yamashiro, C. J. H. Stolar, and J. J. Kandel, "Anti-VEGF antibody suppresses primary tumor growth and metastasis in an experimental model of Wilm's tumor," Journal of Pediatric Surgery **35** (1), 30-32 (2000).

[116] J. P. Houston, “Near infrared fluorescent optical lymphography for cancer diagnostics,” PhD dissertation, Texas A&M University (2005).

[117] E. M. C. Hillman, C. B. Amoozegar, T. Wang, A. F. H. McCaslin, M. B. Bouchard, J. Mansfield, and R. M. Levenson, “In vivo optical imaging and dynamic contrast methods for biomedical research,” Philosophical Transactions of the Royal Society **369**, 4620-4643 (2011).

[118] M. L. Flexman, F. Vlachos, H. K. Kim, S. R. Sirsi, J. Huang, S. L. Hernandez, T. B. Johung, J. W. Gander, A. R. Reichstein, B. S. Lampl, A. Wang, M. A. Borden, D. J. Yamashiro, J. J. Kandel, and A. H. Hielscher, “Monitoring early tumor response to drug therapy with diffuse optical tomography,” Journal of Biomedical Optics **17**(1), 016014 (20012).

[119] C. Li, G. S. Mitchell, J. Dutta, S. Ahn, R. M. Leahy, and S. R. Cherry, “ A three-dimensional multispectral fluorescence optical tomography imaging system for small animals based on a conical mirror design,” Optics Express **17**(9), 7571-7585 (2009).

[120] J. S. Reynolds, T. L. Troy, and E. M. Sevick-Muraca, "Multipixel Techniques for Frequency-Domain Photon Migration Imaging," Biotechnology Progress **13**, 669-680 (1997).

[121] A. B. Thompson, E. M. Sevick-Muraca, "Near-infrared fluorescence contrast-enhanced imaging with intensified charge-coupled device homodyne detection: measurement precision and accuracy, " Journal of Biomedical Optics **8**, 111-120 (2003).

[122] D. Kang and M. A. Kupinski, “Noise characteristics of heterodyne/homodyne frequency-domain measurements,” Journal of Biomedical Optics **17**(1), 015002 (2012).

[123] F. P. Bolin, L. E. Preuss, R. C. Taylor, and R. J. Ference, “Refractive index of some mammalian tissues using a fiber optic cladding method,” Applied Optics **28**(12), 2297-2303 (1989).

[124] A. Kinele, L. Lilge, M. S. Patterson, R. Hibst, R. Steiner, and B. C. Wilson, “Spatially resolved absolute diffuse reflectance measurements for noninvasive determination of the optical scattering and absorption coefficients of biological tissue,” Applied Optics **35**(13), 2304-2314 (1996).

[125] A. K. Popp, M. T. Valentine, P. D. Kaplan, and D. A. Weitz, “Microscopic origin of light scattering in tissue,” Applied Optics **42**(16), 2871-2880 (2003).

[126] Y. L. Kim, Y. Liu, R. K. Wali, H. K. Roy, M. J. Goldberg, A. K. Kromin, K. Chen, and V. Backman, “Simultaneous measurement of angular and spectral properties of light scattering for characterization of tissue microarchitecture and its alteration in early precancer,” IEEE Journal of Selected Topics in Quantum Electronics **9**(2), 243-256 (2003).

[127] A. Kienle, F. K. Foster, and R. Hibst, "Anisotropy of light propagation in biological tissue," Optics Letters **29**(22), 2617-2619 (2004).

[128] H. Gao, and H. Zhao, "Multilevel bioluminescence tomography based on radiative transfer equation Part1: l1 regularization," Optics Express, **18**(3), 1854-1871 (2010).

[129] S. Minkowycz, E. Sparrow, and J. Murthy, *Handbook of Numerical Heat Transfer*. Hoboken, New Jersey: Wiley (2006).

[130] K. Ren, G. Bal, and A. H. Hielscher, "Frequency domain optical tomography with the equation of radiative transfer," SIAM Journal on Scientific Computing **28**, 1463–1489, (2006).

[131] H. K. Kim and A. Charette, "A sensitivity function-based conjugate gradient method for optical tomography with the frequency-domain equation of radiative transfer," Journal of Quantitative Spectroscopy and Radiative Transfer **104**, 24–39 (2007).

[132] G. S. Abddoulaev, K. Ren, and A. H. Hielscher, "Optical tomography as a PDE-constrained optimization problem," Inverse Problem **21,** 1507– 1530 (2005).

[133] Y. Saad, "Iterative Methods for Sparse Linear Systems," Philadelphia, PA: SIAM, (2003).

[134] Y. Saad and M. H. Schultz, "GMRES: A generalized minimal residual algorithm for solving non symmetric linear systems," SIAM Journal on Scientific and Statistical Computing **3**, 856–869 (1986).

[135] J. Chang, H. L. Graber, and R. L. Barbour, "Imaging of fluorescence in highly scattering media," IEEE Transactions on Biomedical Engineering **44(**9), 810–822 (1997).

[136] R. Roy and E. M. Sevick-Muraca, "A numerical study of gradient-based nonlinear optimization methods for contrast enhanced optical tomography," Optics Express **9,** 49–65 (2001).

[137] A. D. Klose and A. H. Hielscher, "Fluorescence tomography with simulated data based on the equation of radiative transfer," Optics Letters **28**, 1019–1021 (2003).

[138] A. D. Klose, V. Ntziachristos, and A. H. Hielscher, "The inverse source problem based on the equation of radiative transfer," Journal of Computational Physics **202**, 323–345 (2005).

[139] D. Y. Paithankar, A. U. Chen, B. W. Pogue, M. S. Patterson, and E. M. Sevick-Muraca, "Imaging of fluorescent yield and lifetime from multiply scattered light reemitted from random media," Applied Optics **36**, 2260–2272 (1997).

[140] H. Jiang, "Frequency-domain fluorescent diffusion tomography: A finite-element-based algorithm and simulations," Applied Optics **37,** 5337– 5343 (1998).

[141] M. A. O'Leary, D. A. Boas, X. D. Li, B. Chance, and A. G. Yodh, "Fluorescence lifetime imaging in turbid media," Optics Letters **21**, 158–160 (1996).

[142] Ntziachristos and R. Weissleder, "Experimental three-dimensional fluorescence reconstruction of diffuse media by use of a normalized Born approximation," Optics Letters **26,** 893–895 (2001).

[143] J. Lee and E. M. Sevick-Muraca, "Three-dimensional fluorescence enhanced optical tomography using referenced frequency-domain photon migration measurements at emission and excitation wavelengths," Journal of the Optical Society of America A **19**, 759–771 (2002).

[144] M. J. Eppstein, D. J. Hawrysz, A. Godavarty, and E. M. SevickMuraca, "Three-dimensional, Bayesian image reconstruction from sparse and noisy data sets: Near-infrared fluorescence tomography," Proceedings of the National Academy of Sciences **99**, 9619–9624 (2002).

[145] A. B. Milstein, S. Oh, K. J. Webb, C. A. Bouman, Q. Zhang, D. A. Boas, and R. P. Millane, "Fluorescence optical diffusion tomography," Applied Optics **42**, 3081–3094, 2003.

[146] J. Nocedal and S. J. Wright, *Numerical Optimization*. New York: Springer-Verlag, (2006).

[147] G. S. Abddoulaev, K. Ren, and A. H. Hielscher, "Optical tomography as a PDE-constrained optimization problem," Inverse Problems **21**, 1507–1530 (2005).

[148] H. K. Kim and A. H. Hielscher, "A PDE-constrained reduced Hessian SQP method for optical tomography based on the frequency-domain equation of radiative transfer," Inverse Problems **25**, 015010 (2009).

[149] L. Biegler, O. Ghattas, M. Heinkenschloss, and B. Bloemen, *Large-Scale PDE-Constrained Optimization*. New York: Springer-Verlag, (2003).

[150] L. Biegler, C. Schmid, and D. Ternet, *A Multiplier-Free, Reduced Hessian Method For Process Optimization, Large-Scale Optimization with Applications, Part II: Optimal Design and Control*. New York: Springer-Verlag, (1997).

[151] J. L. Hu, Z. Wu, H. McCann, L. E. Davis, and C. G. Xie, "Sequential quadratic programming method for solution of electromagnetic inverse problems," IEEE Transactions on Antennas and Propagation **53(**8), 2680–2687 (2005).

[152] D. Feng and T. Pulliam, *All-at-once reduced Hessian SQP scheme for aerodynamics design optimization (RIACS technical report)*, NASA Ames Research Center, Mountain View, (1995).

[153] L. Biegler, J. Nocedal, C. Schmid, and D. Ternet, “Numerical experience with a reduced Hessian method for large scale constrained optimization,” Computational Optimization and Applications **15**, 45–67 (2000).

[154] M. Modest, *Radiative heat transfer*. New York: MacGraw-Hill Inc., (2003).

[155] M. A. Khalil, H. K. Kim, I-K. Kim, M. Flexman, R. Dayal, G. Shrikhande, and A.H. Hielscher, “Dynamic Diffuse Optical Tomography Imaging of Peripheral Arterial Disease,” Biomedical Optics Express **3**(9), 2288 (2012).

[156] M. L. Flexman, M. A. Khalil, R. Al Abdi, H. K. Kim, C. J. Fong, E. Desperito, D. L. Hershman, R. R. Barbour, and A. H. Hielscher, “Digital optical tomography system for dynamic breast cancer imaging,” Journal of Biomedical Optics **16**(7), 076014 (2011).

[157] A. Corlu, R. Choe, T. Durduran, M. A. Rosen, M. Schweiger, S. R. Arridge, M. D. Schnall, and A. G. Yodh, "Three-dimensional in vivo fluorescence diffuse optical tomography of breast cancer in humans." Optics Express **15**(11), 6696-6716 (2007).

[158] B. J. Tromberg, B. W. Pogue, K. D. Paulsen, A. G. Yodh, D. A. Boas, and A. E. Cerussi, “Assessing the future of diffuse optical imaging technologies for breast cancer management,” Medical Physics **35**, 2443 (2008).

[159] S. V. D. Ven, A. Wiethoff, T. Nielsen, B. Brendel, M. V. D. Voort, R. Nachabe, M. V. D. Mark, M. V. Beek, L. Bakker, L. Fels, S. Lias, P. Juijten, and W. Mail, "A novel fluorescent imaging agent for diffuse optical tomography of the breast: first clinical experience in patients.” Molecular Imaging and Biology **12**(3), 343-348 (2010).

[160] M. Fradkin, M. C. Hofmann, J. Rouet, R. H. Moore, D. B. Kopans, K. Tipton, S. Suryanarayanan, D. A. Boas, and Q. Fang, "Diagnosing breast cancer using independent diffuse optical tomography and x-ray mammography scans," Proceedings of SPIE **8574**, 85740G (2013).

[161] S. A. Carp, A. Y. Sajjadi, C. M. Wanyo, Q. Fang, M. C. Specht, L. Schapira, B. Moy, A. Bardia, D. A. Boas, and S. J. Isakoff, "Hemodynamic signature of breast cancer under fractional mammographic compression using a dynamic diffuse optical tomography system," Biomedical Optics Express **4**(12), 2911-2924 (2013).